BTO 2015.025 | May 2015

BTO report

Addressing Quality Issues During Potable Water ASR

Optimizing Aquifer Storage Recovery through hydrogeochemical analysis of a pilot project, column tests and modeling

KWR Watercycle Research Institute

BTO

Addressing Quality Issues During Potable Water ASR

Optimizing aquifer storage recovery through hydrogeochemical analysis of a pilot project, column tests and modeling

BTO 2015.025 | May 2015

Project number
B111664

Project manager
Ir. Jan Willem Kooiman

Client
BTO – Subsurface storage of water and energy

Quality Assurance
Prof. Dr. Pieter J. Stuyfzand

Author(s)
Andreas E. Antoniou MSc

Sent to
This report is distributed to BTO-participants and is public.

Year of publishing
2015

More information
Ir. Jan Willem Kooiman
T 030 6069683
E jan.willem.kooiman@kwrwater.nl

Keywords
ASR, grondwater kwaliteit, kolom experimenten, mangaanverwijdering

PO Box 1072
3430 BB Nieuwegein
The Netherlands

T +31 (0)30 60 69 511
F +31 (0)30 60 61 165
E info@kwrwater.nl
I www.kwrwater.nl

KWR Watercycle Research Institute

BTO *Managementsamenvatting*

Kwaliteitsaspecten in kaart gebracht bij ondergrondse drinkwateropslag middels ASR

Auteur Dr. Andreas Antoniou

Aquifer Storage & Recovery (ASR) is een watermanagementtechniek waarbij men water in de ondergrond opslaat voor gebruik in tijden van watertekort. Toepassingen liggen veelal in seizoensberging en hebben als extra voordeel een efficiënte en kosteneffectieve inzet van bedrijfsmiddelen. Vanwege deels achterhaalde redenen is ASR in Nederland nog niet breed ingezet. Deze studie heeft als doel om één van die redenen nader in kaart te brengen, namelijk eventuele nadelige kwaliteitsveranderingen in de ondergrond. Hierbij ligt de focus op infiltratie van zuurstofhoudend water in een zuurstofloze ondergrond gevuld met zoet grondwater. De resultaten wijzen erop dat adequate behandeling van het infiltratiewater en preparatie van de bodem, vooraf of tijdens de bedrijfsvoering, nadelige waterkwaliteitsveranderingen bij ASR-systemen kunnen voorkomen of verkleinen. Dit onderzoek presenteert een speciaal ontwikkeld rekenmodel, gebaseerd op een reactief transportmodel en uitgebreid met een Python-script, dat geschikt is om voor verschillende waterkwaliteiten en bodems de toepasbaarheid van ASR vooraf te bepalen.

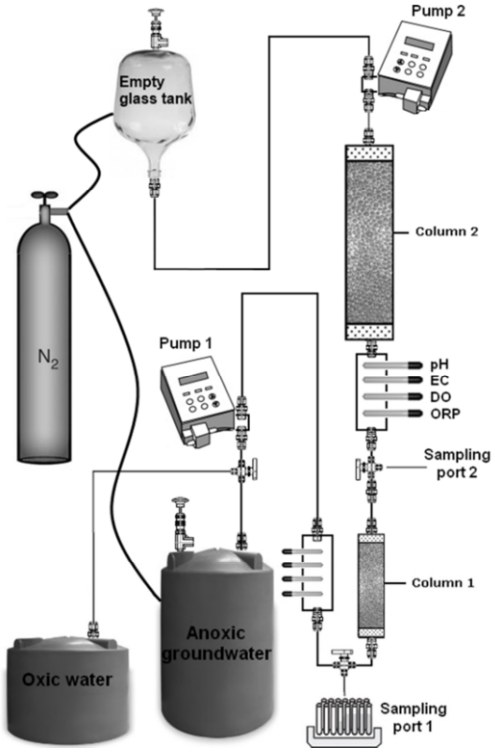

Schematische weergave van de ASR kolom, speciaal ontwikkeld door Andreas Antoniou en KWR en beschikbaar voor toekomstig onderzoek.

Belang: terughoudendheid voor ASR wegnemen door beter inzicht in kwaliteitsaspecten

De noodzaak voor ondergrondse wateropslag neemt steeds meer toe. Redenen hiervoor zijn een toegenomen frequentie van perioden met wateroverlast en droogte, de verwachte uitbreiding van waterproblemen als gevolg van klimaatverandering en een toenemende druk op zowel de bovengrondse ruimte als economische doelen. Ondanks wereldwijde toepassing van ASR is men in Nederland nog terughoudend. Hier zijn vier redenen voor: (i) vrees voor putverstopping, (ii) angst voor nadelige kwaliteitsveranderingen in de ondergrond, (iii) gebrek aan vertrouwen in een voldoende hoog terugwinpercentage, en (iv) onvoldoende motivatie vanwege continue beschikking over voldoende water. Voor de eerste drie redenen bestaan technische oplossingen. De angst voor nadelige kwaliteitsveranderingen in de ondergrond (reden ii), blijkt in Nederland op veel plaatsen gegrond. Daarom wil deze studie meer grip krijgen op wat die veranderingen daadwerkelijk zijn en wat hiertegen valt te doen. Problemen en oplossingen komen aan bod bij het tijdens piekbehoeften terugwinnen van drinkwater dat tevoren in een zuurstofloze watervoerende laag werd geïnfiltreerd.

Aanpak: veelzijdig gebruik van bestaande meetresultaten, aangevuld met proeven

Als basis voor het onderzoek zijn de waterkwaliteitsveranderingen tijdens een tien jaar durende, representatieve drinkwater ASR proef in Herten (Limburg, Nederland) geïdentificeerd en gekwantificeerd. Vervolgens is op grond van de meetresultaten een reactieve transportsimulatie opgesteld. Ook werd het model gebruikt om de effectiviteit van verschillende voorbehandelingstechnieken te testen, met als doel de agressiviteit van het infiltratiewater ten aanzien van de doelaquifer in Herten te verlagen.

Na inbouw van een Python-script, is bovengenoemd model verder toegepast om de kwaliteitsverandering te testen van drie infiltratiewatersoorten tijdens ASR toepassing: ontzilt zeewater, regenwaterafvoer in stedelijk gebied en drinkwater. Uitgangspunt bij de simulaties was een maximaal terugwinpercentage bij latere ASR cycli, zonder overschrijding van drinkwaternormen.

Tot slot zijn in deze studie de mogelijkheden onderzocht om de terugwinefficiëntie te verhogen door de mangaanmobilisatie middels voorbehandeling van de watervoerende laag te onderdrukken met een kaliumpermanganaat-dosering.

Resultaten: verhoging terugwinpercentage en terugwinrendement van ASR zijn mogelijk

De injectie van zuurstofverzadigd drinkwater veroorzaakt oxidatiereacties. De meest reactieve bestanddelen zitten in de watervoerende laag. Vooral de oplossing van mangaan vormde een probleem, met een lichte overschrijding van de drinkwaternorm in het teruggewonnen drinkwater (0,05 mg/L).

Zuurstofverrijking van het infiltratiewater, gecombineerd met pH-buffering reduceert de mangaanconcentratie, met bijkomend voordeel van een verhoogd terugwinpercentage. Dankzij de voorspellende waarde van het met Python-script uitgebreide model kan de geschiktheid van verschillende ASR systemen vooraf worden getest op basis van de aquifer en de kwaliteit van het infiltratiewater in een bepaalde setting.

Een zelfontworpen kolomopstelling toonde een succesvolle onderdrukking van de gevreesde mangaanmobilisatie aan door voorbehandeling van zuurstofloos, pyriet- en sideriethoudend zand met een kaliumpermanganaatoplossing. Het terugwinrendement nam hierin toe.

Implementatie: onderzoek vertaalbaar naar andere ASR(-achtige) toepassingen

Het hier gepresenteerde onderzoek brengt kwaliteitsaspecten in kaart bij het gebruik van ASR voor infiltratie van zuurstofhoudend water in een zuurstofloze ondergrond gevuld met zoet grondwater. De toegepaste onderzoeksmethoden, processen en modellen zijn ook inzetbaar in andere ASR(-achtige) toepassingen met andere soorten infiltratiewater voor andere doeleinden. Hierbij kan worden gedacht aan de opslag van regen- of oppervlaktewater voor de landbouw en bij warmte-koude-opslag.

Rapport

Dit onderzoek is beschreven in rapport *Addressing Quality Issues During Potable Water ASR* (BTO 2015.025) en proefschrift op 29 april 2015 met succes verdedigd aan de Vrije Universiteit Amsterdam (promotor prof. dr. P.J. Stuyfzand).

Jaar van publicatie
2015

Meer informatie
Prof. dr. Pieter Stuyfzand
T 030 60 69 552
E pieter.stuyfzand@kwrwater.nl

Keywords
ASR, grondwater kwaliteit, kolom experimenten, mangaanverwijdering

PO Box 1072
3430 BB Nieuwegein
The Netherlands

T +31 (0)30 60 69 511
F +31 (0)30 60 61 165
E info@kwrwater.nl
I www.kwrwater.nl

KWR Watercycle Research Institute

BTO 2015.025 | May 2015 © KWR

BTO *Samenvatting*

Addressing Quality Issues During Potable Water ASR

Aquifer Storage & Recovery (ASR) is een watermanagementtechniek waarbij men water in de ondergrond opslaat voor gebruik in tijden van watertekort. Kenmerkend daarbij is dat het infiltreren of injecteren en het terugwinnen met dezelfde put geschiedt, en dat ASR doorgaans 3 fasen kent: een infiltratie-, bergings- en terugwinfase. ASR kan met allerlei soorten water bedreven worden: voorgezuiverd afvalwater, rivierwater, oeverfiltraat, regenwater of drinkwater. De bodem vervult de rol van een ondergronds reservoir, beschermd tegen o.a. radioactieve fall-out, algenbloei en verdampingsverliezen, maar met risico op ongewenste kwaliteitsveranderingen door bodemreacties, putverstopping, waterverliezen door het af- of opdrijven van het geïnfiltreerde watervolume, en menging met oorspronkelijk grondwater van (soms) slechte kwaliteit.
ASR wordt veelal toegepast voor seizoensberging, met opslag gedurende natte periodes en verbruik in droge periodes, maar ASR kan ook watertekorten op langere termijn helpen overbruggen. Een extra voordeel van ASR bestaat uit het efficiënt en kosteneffectief inzetten van bedrijfsmiddelen. Door toepassing van ASR kan een zuiveringsinstallatie gelijkmatiger over het jaar gaan produceren, omdat men piekbehoeften kan dekken vanuit ondergronds geborgen water dat tijdens daluren of dalmaanden (voor)gezuiverd is. Zodoende wordt met een kleinere, dus goedkopere installatie een constanter volume aan water per tijdseenheid bereid.
ASR wordt al enkele decennia wereldwijd toegepast, in zeer uiteenlopende omstandigheden. In Nederland heeft ASR echter nog geen brede ingang gevonden, om vier deels achterhaalde redenen: (i) vrees voor putverstopping, (ii) angst voor nadelige kwaliteitsveranderingen in de ondergrond die in Nederland op veel plaatsen nogal reactief blijkt, (iii) gebrek aan vertrouwen in een voldoende hoog terugwinpercentage, en (iv) onvoldoende motivatie vanwege continue beschikking over voldoende water.
Inmiddels weten wij dat redenen i t/m iii onvoldoende zwaar wegen om ASR uit te sluiten. Er zijn immers vele technische oplossingen voor deze problemen. Daarnaast is de noodzaak tot ondergrondse berging van water met goede kwaliteit enorm toegenomen ten gevolge van de toegenomen frequentie van perioden met wateroverlast en droogte, de verwachte verergering van waterproblemen door klimaatverandering en een toenemende druk op zowel de bovengrondse ruimte als economische doelen.

In dit proefschrift komen vooral de waterkwaliteitsproblemen (en hun oplossingen) aan de orde, die ontstaan bij het infiltreren van zuurstofhoudend water in een zuurstofloze ondergrond gevuld met zoet grondwater. De focus is daarbij vooral gericht op problemen met de opslag van ver voorgezuiverd water zoals drinkwater. De beschouwde methoden van onderzoek, processen en modellen zijn evenwel inzetbaar ook in andere ASR en ASR-achtige toepassingen met andere soorten infiltratiewater voor andere doeleinden, zoals bij de opslag van regenwater voor de landbouw en bij Koude-Warmte opslag.

In hoofdstuk 2 zijn de waterkwaliteistveranderingen tijdens een 10 jaar durende drinkwater ASR proef in Herten (Limburg, Nederland) geïdentificeerd en gekwantificeerd. Het betreft een wereldwijd veelvoorkomende, dus representatieve situatie, waarin zuurstofverzadigd drinkwater in een zuurstofloze watervoerende laag wordt gebracht en tijdens piekbehoefte wordt teruggewonnen.
De injectie van dit water veroorzaakte oxidatiereacties met de meest reactieve aquifer bestanddelen, namelijk pyriet, organisch materiaal en geadsorbeerd ijzer en mangaan. Het hierbij vrijkomende zuur

werd gebufferd door omzetting van in het drinkwater overvloedig aanwezige bicarbonaat in koolzuur en door langzame oplossing van carbonaatmineralen, voornamelijk bestaande uit kalk en mangaanhoudende sideriet. Dit leidde tot de mobilisatie van vooral sulfaat, anorganische koolstof, ijzer en mangaan in het teruggewonnen drinkwater. Ook losten er sporenelementen (Al, Co en Ni) op door pyrietoxidatie, maar deze werden tijdens de bergings- en terugwinfase weer in de bodem vastgelegd in vers gevormde ijzerhydroxiden. Vooral de oplossing van mangaan vormde een probleem, omdat dit de drinkwaternorm van het teruggewonnen drinkwater (0,05 mg/L) iets deed overschrijden. Dit in combinatie met een afgenomen drinkwaterbehoefte leidde ertoe dat Waterleiding Maatschappij Limburg (WML) destijds (!) afzag van ASR toepassing.

In hoofdstuk 3 is een reactieve transportsimulatie beschreven van de in hoofdstuk 2 gepresenteerde meetresultaten met betrekking tot de Herten pilot. De simulatie geschiedde met ééndimensionale stroombanen vanuit de ASR put de aquifer in en weer terug, met PHREEQC-2 als reactief transport model en met PEST als kalibratiegereedschap. De aquifer werd geschematiseerd door middel van 2 geochemisch homogene bodemlagen. Het gekalibreerde en gevalideerde model werd vervolgens gebruikt om de effectiviteit te testen van verschillende voorbehandelingstechnieken om het infiltratiewater minder aggressief te maken ten aanzien van de doelaquifer in Herten. De gesimuleerde resultaten maken duidelijk dat zuurstofverrijking van het infiltratiewater, alleen in combinatie met pH-buffering door bijvoorbeeld NaOH, de mobilisatie van ijzer en mangaan voldoende kan reduceren. Deze werkwijze voorkomt de geconstateerde mangaanproblemen en verhoogt het terugwinpercentage.

Het model is in hoofdstuk 4, na inbouw van een Python script, verder toegepast om te testen hoe de kwaliteit verandert van 3 infiltratiewatersoorten (ontzilt zeewater, regenwaterafvoer in stedelijk gebied en drinkwater) tijdens ASR toepassing in een zuurstofloze aquifer, met of zonder beldrift (zijdelingse verplaatsing van het geïnfiltreerde volume door de ‘natuurlijke’ grondwaterstroming). De geteste watersoorten beslaan een breed spectrum aan infiltratiewateren die ook in andere delen van de wereld worden gebruikt voor ASR toepassing. Uitgangspunt bij de simulaties was dat er met het infiltratiewater eerst een bufferzone rond het opgeslagen water wordt opgebouwd, om tijdens navolgende ASR cycli te zorgen voor maximalisatie van het terugwinpercentage zonder overschrijding van drinkwaternormen. Het Python script zorgt ervoor dat de terugwinning automatisch wordt stopgezet en de volgende injectiefase begint, zodra de concentratie van kritische bestanddelen tijdens terugwinning een bepaalde drempelwaarde overschrijdt.
Het model maakt het mogelijk om vooraf de prestatie te voorspellen van verschillende ASR systemen ten aanzien van de kwaliteit en kwantiteit van het terug te winnen water. Dit houdt in dat de geschiktheid getest kan worden van zowel de aquifer als de kwaliteit van het infiltratiewater voor ASR-toepassing in een bepaalde setting.

In hoofdstuk 5 zijn de mogelijkheden onderzocht om door voorbehandeling van de watervoerende laag met een kaliumpermanganaatoplossing de geconstateerde mangaanmobilisatie te onderdrukken, ter verhoging van de terugwinefficiëntie. Hiertoe zijn kolomproeven uitgevoerd met een zelfontworpen kolomopstelling, die haar bijzonderheid ontleent aan de complexe simulatie van ASR cycli in een zuurstofloze omgeving. Met deze kolomopstelling werd aangetoond dat voorbehandeling van zuurstofloos, pyriet- en sideriethoudend zand met een kaliumpermanganaatoplossing succesvol is in het onderdrukken van de gevreesde mangaanmobilisatie, en dat dit tot een verbeterd terugwinrendement leidt.

Addressing quality issues during potable water ASR

Optimizing Aquifer Storage Recovery through hydrogeochemical analysis of a pilot project, column tests and modeling

Andreas Eleftherios Antoniou | 2015

ISBN:
Cover by: Harris Hatzimpaloglou
Lay-out by: Ilse Stronks, persoonlijkproefschrift.nl
Printed by: Ipskamp Drukkers BV, Enschede, The Netherlands

This work was performed within the cooperation framework of Wetsus, Center of excellence for sustainable water technology (www.wetsus.nl). Wetsus is co-funded by the Dutch Ministry of Economic Affairs and the Ministry of Infrastructure and Environment, the European Union Regional Development Fund, the Province of Fryslân, and the Northern Netherlands Provinces.

The research was also financially supported by the joint research program of the dutch water sector (BTO), ‘‘Source Risk Management’’ theme.

The work was carried out both at KWR Watercycle Research Institute, Nieuwegein and the Critical Zone Hydrology Group, Department of Earth Sciences, Faculty of Earth and Life Sciences, Vrije University Amsterdam.

VRIJE UNIVERSITEIT

Addressing quality issues during potable water ASR

Optimizing Aquifer Storage Recovery through hydrogeochemical analysis of a pilot project, column tests and modeling

ACADEMISCH PROEFSCHRIFT

ter verkrijging van de graad Doctor aan
de Vrije Universiteit Amsterdam,
op gezag van de rector magnificus
prof.dr. F.A. van der Duyn Schouten,
in het openbaar te verdedigen
ten overstaan van de promotiecommissie
van de Faculteit der Aard- en Levenswetenschappen
op woensdag 29 april 2015 om 11.45 uur
in de aula van de universiteit,
De Boelelaan 1105

door
Andreas Eleftherios Antoniou
geboren te Panorama (Thessaloniki), Griekenland

promotor: prof.dr. P.J. Stuijfzand
copromotor: dr. B.M. van Breukelen

Examination committee
dr. H.P. Broers (Vrije Universiteit Amsterdam / TNO)
dr. Doris van Halem (Technische Universiteit Delft)
prof.dr. J. Griffioen (Universiteit Utrecht / TNO)
prof.dr. G. Massmann (Universität Oldenburg)
prof.dr. T.N. Olsthoorn (Technische Universiteit Delft / Waternet)

TABLE OF CONTENTS

ABSTRACT

This thesis is built upon water quality issues identified during a drinking ASR pilot project in the Netherlands. The aquifer is considered of a representative nature for ASR standards. Therefore, studying the issues faced and proposing solutions is considered internationally relevant for many ASR candidate applications. The hydrogeochemical processes responsible for the deterioration of water quality are identified and quantified in Chapter 2. The injection of oxic source water for ASR purposes triggers oxidation reactions with the most reactive aquifer constituents, namely pyrite, sedimentary organic material, and exchangeable Fe(II), NH_4^+, and Mn(II). The induced acidity is buffered by conversion of abundant HCO_3 into CO_2 and by slow dissolution of carbonate minerals such as calcite, siderite, and ankerite. As a consequence, heavy metals such as Fe(II) and Mn(II) are released in the groundwater. During recovery, due to inadequately high pH conditions, adsorptive removal to neoformed ferrihydrite is not efficient and the released heavy metals reach the ASR well. Trace elements (As, Co, Ni) released during pyrite oxidation are also observed in the groundwater at various distances from the ASR well. The water-sediment reactions and the leaching rate of reactive solid phases are quantified following a mass balance approach. The poor, from a drinking perspective, quality of the abstracted water, in combination with expected post-treatment costs, convinced the water supply company WML (Limburg, The Netherlands) to abandon the idea of ASR application in this type of aquifer.

Chapter 3 describes the reactive transport simulation of one-dimensional flow lines that extend from the ASR well. The Herten aquifer is discretized into 4 geochemically homogeneous sublayers and the spatio-temporal evolution of water quality along the flow lines is successfully simulated by the model. The calibrated and validated model is further used to test pre-treatment techniques of the source water prior to injection. Based on the simulated results, oxygen enrichment of the source water combined with pH-buffering agents (e.g. NaOH) can control the mobilization of heavy metals and increase the recovery efficiency of the ASR plant.

In chapter 4, the reactive transport model is further used to test representative source water types (desalinated seawater, urban storm water) that have been used for ASR purposes in other parts of the world. These scenarios are tested in conjunction with the ASR cycles required to build a buffer zone that allows complete recovery of the stored water body without exceedances of drinking water standards. In order to achieve this, the model is coupled to a Python script that automatically stops recovery and starts the next injection phase when certain specified concentration thresholds are exceeded. The implementation of the buffer zone can be accelerated by enriching the source water with O_2 and/or NaOH in order to suppress the Fe(II), Mn(II) and As problems related to the tested source water types.

Finally, chapter 5 describes the implementation of an experimental column setup, designed to closely simulate ASR cycles in an anoxic environment. The installation is used to test

aquifer pretreatment prior to ASR application in order to neutralize the various reductants responsible for the deterioration of the abstracted water quality. Pre-treating the aquifer with a potassium permanganate solution suppresses significantly the pyrite reactivity and generates abundant Mn-oxide precipitates with high sorption capacity. The treatment helps controlling the Mn(II) mobilization and allows for an overwhelmingly improved recovery efficiency.

CHAPTER 1
Introduction

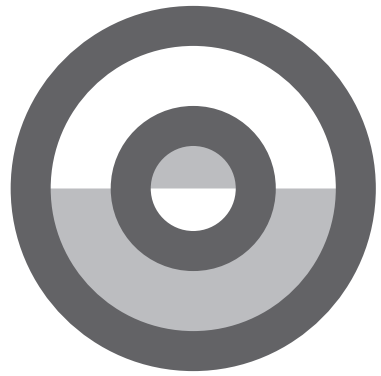

1.1 AN INTRODUCTION TO ASR

Aquifer storage and recovery (ASR) is a water resource management method to balance water supply with demand. During periods of excess water, water is injected and stored in an aquifer for subsequent recovery and use in times of water demand (Pyne 2005, Maliva and Missimer 2010). Wet months and strong rain events constitute the most plausible examples of excess water periods. According to Pyne (2005), we should consider operating reservoirs at lower levels to capture peak flows and transfer them to ASR storage, recovering the water when needed. Periods of water demand usually appear during dry seasons or due to higher total demand such as during tourism season. Storage may, therefore, have a broad duration range depending on whether it aims at covering emergency, seasonal, or long-term demand.

The stored water typically extends a few tens to 600 m away from the ASR well. A buffer zone separates the recoverable stored water from the surrounding native water, and consists of a kind of mixture between the two water types. Towards the ASR well, this mixing does not consist of true mixing but it reflects the hydrogeochemical similarity between the injected water that underwent strong reactions with the aquifer, and the native groundwater that underwent several of the same reactions. Towards the interface, this mixing is true physical mixing. The volume of the buffer zone therefore depends mainly upon the extent of geochemical reactions and natural dispersion in the aquifer. Sources of water suitable for injection and use within previous ASR applications include treated drinking water (Stuyfzand 1998a, Izbicki et al. 2010), treated or untreated groundwater (Pyne 2005), rainwater (Dillon and Barry 2005, Barry et al. 2007), high quality reclaimed wastewater (Vanderzalm et al. 2006, Maliva et al. 2007), and desalinated seawater (Mukhopadhyay et al. 1998, Rashid and Almulla 2005).

The water is typically stored in deep, confined aquifers but there are cases where unconfined aquifers are used (Gerges et al. 1998). The latter are generally not preferred since they are more vulnerable to surface contamination and to complications resulting from the mound of water during injection which creates a temporary radial hydraulic gradient (Herrmann 2005). About one third of ASR schemes store water in brackish or even saline aquifers with total dissolved solids (TDS) concentrations up to 20,000 mg/L. The abstracted water may require treatment for one or more constituents in order to achieve compliance with drinking water quality standards, due to water-rock interactions or mixing with ambient groundwater (Pyne 2005). Ideally, however, this is not needed. Observation wells are usually installed at increasing distance from the ASR well to monitor the movement of the stored water and the buffer zone during the various stages of ASR (injection, storage, and recovery) as well as the changes in water quality that may occur.

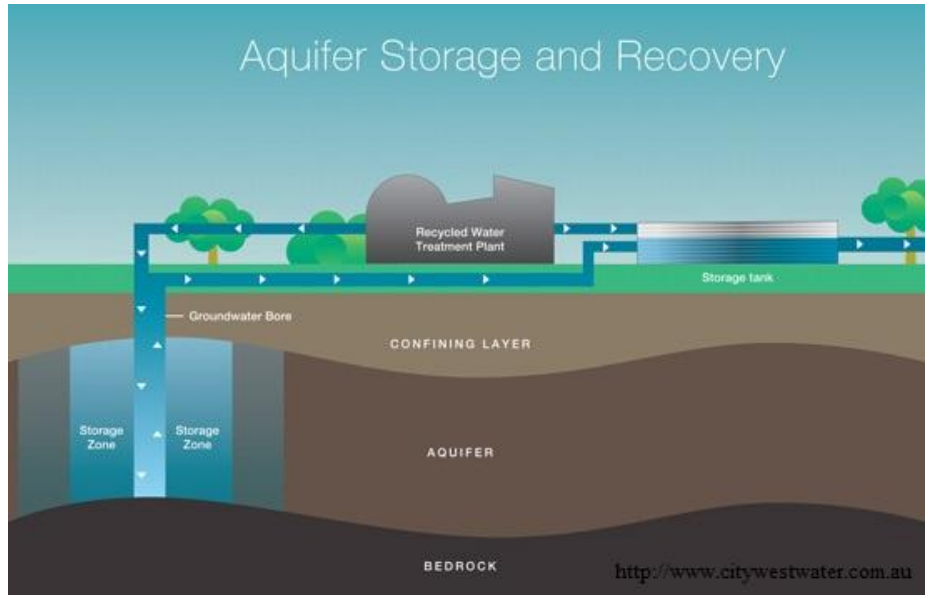

Figure 1.1 ASR scheme in cross section, depicting the injection of recycled water in a confined aquifer after being treated at a local treatment plant.

Advantages of ASR

ASR normally offers financial benefits and water quality improvements. The main financial advantages compared to surface water storage consist of (1) an increased security of water supply and reduced well maintenance, (2) little land occupation, (3) reductions in costs of water storage and evaporation losses, and (4) during water purification, storing the treated water in the subsurface can decrease the peak factor allowing the facility to have a smaller capacity (Pyne 2005).

As opposed to single purpose groundwater abstraction wells, ASR wells offer a decreased well clogging risk due to flow reversals which prevent or delay the accumulation of clogging material along the borehole wall. With respect to water quality improvements, processes such as filtration, sorption, and biodegradation are responsible for the water “recycling” during its passage through the aquifer. The intentional use of the natural attenuation processes to improve water quality has been referred to as natural aquifer treatment (Maliva and Missimer 2010). NAT is a beneficial side-effect of ASR systems; however it could be used as an integral component of the treatment processes for reclaimed water or surface water. NAT has already been used for over 100 years in riverbank filtration and subsurface iron removal systems. With respect to surface water storage, therefore, water quality improvements during ASR may consist of denitrification, biodegradation of organic micropollutants like chlorination byproducts (Pavelic et al. 2005) and pharmaceuticals (Overacre et al. 2006), and removal of pathogens (Page et al. 2010). Moreover, ASR

closely resembles the technique of subsurface iron removal (SIR) where a limited amount of oxygenated water is injected into the aquifer to reduce originally high concentrations of ferrous iron, manganese and ammonium in the zone close to the injection point (Van Beek 1983, Rott and Friedle 1985, Braester and Martinell 1988, Appelo et al. 1999, Mettler 2002, Van Halem 2011). A similar process takes place in ASR systems during the recovery phase, when iron and manganese (mobilized in the outer zones of the ASR bubble) show a retarded breakthrough due to adsorption in the oxidized zone around the ASR well (Stuyfzand et al. 2005b). Adsorption is taking place in SIR systems on the newly formed iron-hydroxides and on the original cation-exchangers, mainly composed of sedimentary organic material and clay minerals (Appelo et al. 1999).

Disadvantages of ASR

On the other hand, disadvantageous aspects of ASR include water losses due to migration of the stored water through the aquifer and adverse water quality changes that need additional treatment. Interaction between injected water and native groundwater and sediments can result in quality deterioration of the injected source water. Upon injection of the source water, mixing with the native groundwater, mineral dissolution and precipitation processes, cation exchange, and redox reactions may all contribute to the alteration of the injected water quality.

Additional complications arise during ASR applications in brackish/saline aquifers due to buoyancy effects between the source water and the heavier native groundwater. These effects result in an earlier chloride breakthrough deteriorating the recovered water quality and reducing the theoretically recoverable fraction due to mixing only.

Hydrogeochemical reactions

Upon injection of oxic water, oxygen is mainly consumed during the oxidation of aquifer constituents such as iron-sulfides, exchangeable iron, manganese and ammonium, and sedimentary organic material. Pyrite oxidation may result in elevated concentrations of released ferrous iron, arsenic, and other trace elements such as nickel and cobalt (Stuyfzand 1998a, Pyne 2003). Arsenic release has been reported during ASR operations in different parts of the world and is attributed to oxidation of arsenic-bearing pyrite, a trace component (~0.1%) of the aquifer matrix. In Florida, United States, for example, recovered arsenic concentrations reached 1.5 µmol/L despite concentrations of <0.13 µmol/L in the native groundwater and the source water (Mirecki 2004, Pyne et al. 2004, Price and Pichler 2006, Arthur et al. 2007, Jones and Pichler 2007, Stuyfzand and Pyne 2010). Arsenic mobilization was also noted during ASR applications in Australia (Vanderzalm et al. 2007) and the Netherlands (Stuyfzand 2001).

Various studies indicate that pyrite oxidation rates strongly depend on: (1) the amount and reactivity of organic material competing for reaction with oxidants (Stuyfzand 1998a, Hartog et al. 2002); (2) the size of pyrite grains, with framboidal pyrite having a greater surface area (smaller grain size) and thus oxidizing faster as compared to euhedral pyrite (McKibben and Barnes 1986); (3) coating by iron-hydroxide precipitates which inhibit the rate as the reaction continues (Goldhaber 1983, Nicholson et al. 1990); and (4) temperature, with oxidation rates increasing with temperature (Prommer and Stuyfzand 2005) and becoming very slow below 10°C (Stuyfzand 1998b).

Dissolution processes mainly refer to carbonate minerals and metal oxides. Silicate minerals do not really affect the water quality during ASR due to their low solubilities and slow dissolution rates (Appelo and Postma 2005). Carbonate dissolution is promoted when the source water is undersaturated with respect to these minerals when present in the storage zone. The degree of dissolution depends on the solubility of the mineral at the given pH, temperature, and partial pressure conditions and may result in elevated concentrations of dissolved iron and manganese (Ibison et al. 1995, Pyne 2005, Stuyfzand et al. 2005b). Mineral dissolution may also be triggered by oxidation reactions as a buffering response to the generated acidity, especially when the bicarbonate content is low. Carbon dioxide released by microbial activities (Herczeg et al. 2004) and oxidation of sedimentary organic matter can contribute to the dissolution of carbonate minerals. Iron- and manganese-oxide dissolution can also occur by proton-promoted and reductive pathways (Scot 2005) and may cause similar deteriorating effects.

Cation exchange is always present during ASR causing typically sorption/desorption reactions between Ca, Mg, K, Na, NH_4, Fe, and Mn. The effects of such reactions are usually too small to affect the intended use of the recovered water (Maliva and Missimer 2010). These effects will have a greater magnitude when ASR is performed in a brackish/saline aquifer with the freshening process resulting in stronger sorption of Ca to the sediment and subsequent desorption of Na (and frequently also K, Mg and several trace elements) to the injection water.

Water quality may deteriorate further during an extended storage or recovery phase due to migration of the stored water or due to reducing conditions triggered by anaerobic degradation of organic material in the proximal zone of the ASR well (Vanderzalm et al. 2002, Stuyfzand et al. 2005b). The latter usually involves necrosis of microbial communities that develop during the injection phase and subsequently die-off due to lack of nutrients and oxygen during the storage phase. In such cases, elevated concentrations of iron, manganese, ammonium and arsenic may cause less water to be recoverable as compared to the previously injected volume. The ratio between recovered water and injected water volume define the recovery efficiency of each ASR cycle (Pyne 2005).

Reactive transport modeling is an important tool that can aid on the acquisition of a better understanding of the hydrogeochemical processes taking place in the aquifer, as well as on their quantification based on kinetic rate expressions. Calibrated models can be used to predict the recovered water quality from an ASR well after a number of cycles as well as to study the temporal and spatial leaching of minerals around the ASR well.

1.2 KNOWLEDGE GAPS

The hydrogeochemistry behind processes affecting the recovered water quality during ASR has been extensively studied in the literature; some of these studies were mentioned already in Section 1.1. Some studies describe the evolution of these hydrogeochemical processes in time and with consecutive ASR cycles. Descourvieres et al. (2010), for example, was able to successfully quantify reaction rates of competing redox and buffering reactions during the injection of oxidized aqueous solutions into anoxic groundwater systems. Certain processes seem to fade out in time due to an overall leaching of the reactive phases and due to side-processes dampening the reactivity of the aquifer.

Enhancing the processes that are responsible for water quality improvements, while at the same time inhibiting the processes causing quality deterioration, seems possible, but very few attempts have been made to put certain methods into practice. The ASR concept and the cumulative effects to water quality due to the various hydrogeochemical processes have never been studied in the lab under controlled conditions.

ASR pilots have been simulated using reactive transport models able to simulate the recovered water quality over time (Gaus et al. 2002, Petkewich et al. 2004, Greskowiak et al. 2005, Brown and Misut 2010, Wallis et al. 2011). These models, once calibrated, can however also be used as predictive tools for many aspects related to the ASR plant operation. It is possible to predict the time frame under which the various water quality deteriorating processes related to the oxidation or dissolution of reactive phases will fade away. Running scenario simulations can help assessing the effects on recovered water quality of various source water types and to test methods (such as source water treatment or aquifer treatment) that may improve the ASR operation with respect to recovered water quality.

1.3 RESEARCH OBJECTIVES

Based on the knowledge gaps described above, three key objectives were defined for this research study:

1. Acquiring an improved insight in hydrogeochemical patterns and processes and water quality improvements through long term monitoring of a drinking water ASR pilot and through lab experiments with an innovative column setup (combined with modeling).
2. Improving ASR operation with optional treatments (O_2, NaOH, permanganate) as investigated in the field, with column experiments, and with reactive transport modeling.
3. Assessing and optimizing ASR performance through reactive transport modeling alone, by evaluation of variations in operational aspects (different source water compositions, implementation of a buffer zone, and bubble migration during a prolonged storage phase).

1.4 THESIS OUTLINE

The thesis is organized as follows:

Chapter 2 gives an improved mechanistic insight in hydrogeochemical patterns and processes and water quality improvements during a long term ASR application in a pyritiferous and Mn-carbonate containing sandy aquifer (Herten, The Netherlands). The ASR pilot study in Herten was run by drinking water supply company WML (Water Maatschappij Limburg) in order to test the feasibility and efficiency in terms of recovered water quality and quantity. A mass balance approach was followed to quantify the water-sediment reactions and the leaching rate of reactive solid phases.

Chapter 3 presents the development and calibration of a reactive transport model that simulates and predicts the water quality developments of the previous case study. For this purpose, we followed a novel approach where the model, calibrated with data from the first ASR cycle, was allowed to run a series of 14 later cycles and its longer term performance was validated by comparing the model predictions to the actual observations of these later ASR cycles.

Chapter 4 uses the calibrated reactive transport model to test the behavior of the Herten aquifer upon injection of 3 different source water types (pre-treated drinking water, desalinated and urban storm water). We investigate on how to optimize the cycling scheme by means of enriching the source water with O_2 and/or NaOH and by implementing a buffer zone that would allow a subsequent ideal recovery efficiency of 100% with respect to Fe(II), Mn(II) and As. We finally studied the deteriorating effects of a possible bubble migration following the injection of the different source water types in combination with the source water enrichment.

In chapter 5 we describe the implementation of a realistic, bi-directional column-based ASR simulation, which allowed the injection of oxic tap water in a brackish and anoxic “aquifer” setting. Undisturbed core samples, collected from an ASR candidate aquifer, were used to evaluate the aquifer behavior during potential ASR applications. The persisting Mn(II) mobilization, deriving from carbonate dissolution and triggered by oxidation reactions, compromised during each recovery the abstracted water quality after having recovered 15-30% of the injected water. We assessed the impact of aquifer treatment with an aqueous permanganate solution on water quality, and compared it with the injection of conventional air-saturated water. We specifically evaluated, using a column setup, how permanganate treatment of the aquifer sediments improves the recovery efficiency with respect to manganese and arsenic.

In Chapter 6, finally, we integrate all results, discuss the links between the various chapters and give recommendation for practice and further research.

CHAPTER 2

Hydrogeochemical patterns, processes and mass transfers during ASR in an anoxic sandy aquifer

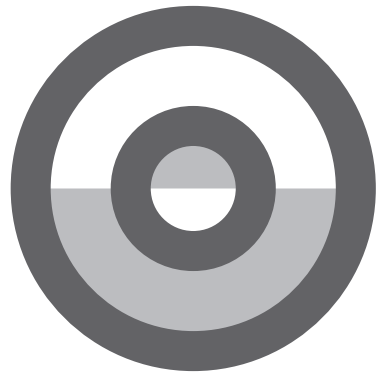

Published as:

Antoniou, E. A. Van Breukelen, B. M., Putters, B. and Stuyfzand, P. J. (2012). Hydrogeochemical patterns, processes and mass transfers during aquifer storage and recovery (ASR) in an anoxic sandy aquifer. Applied Geochemistry 27(12): 2435-2452.

ABSTRACT

The hydrogeochemical processes that took place during an aquifer storage and recovery (ASR) trial in a confined anoxic sandy aquifer (Herten, the Netherlands) were identified and quantified, using observation wells at 0.1, 8 and 25 m distance from the ASR well. Oxic drinking water was injected in 14 ASR cycles in the period 2000-2009. The main reactions consisted of the oxidation of pyrite, sedimentary organic matter, and (adsorbed) Fe(II) and Mn(II) in all aquifer layers (A-D), whereas the dissolution of carbonates (Mg-calcite and Mn-siderite) occurred mainly in aquifer layer D. Extinction of the mobilization of SO_4, Fe(II), Mn(II), As, Co, Ni, Ca, and total inorganic carbon pointed at pyrite and calcite leaching in layer A, whereas reactions with Mn-siderite in layer D did not show a significant extinction over time. Fe(II) and Mn(II) removal during recovery was demonstrated by particle tracking and pointed at sorption to neoformed ferrihydrite. Part of the oxidants was removed by neoformed organic material in the ASR proximal zone (0 - ca. 5 m) where micro-organisms grow during injection and die away when storage exceeds about 1 month. Anoxic conditions during storage led to increased concentrations for a.o. Fe(II), Mn(II) and NH_4 as noted for the first 50-200 m^3 of abstracted water during the recovery phase. With a mass balance approach the water-sediment reactions and leaching rate of the reactive solid phases were quantified. Leaching of pyrite and calcite reached completion up to 8 m distance in layer A, but not in layer D. The mass balance approach moreover showed that Mn-siderite in layer D was probably responsible for the Mn(II) exceedances of the drinking water standard (0.9 µmol/L) in the recovered water. Leaching of the Mn-siderite up to 8 m from the ASR well would take 1600 more pore volumes of drinking water injection (on top of the realized 460).

Keywords: ASR, aquifer recharge, redox, pyrite, siderite, manganese, arsenic, nickel

2.1 INTRODUCTION

Aquifer storage and recovery (ASR) is a method to balance water supply with demand. It consists of injecting water in an aquifer during a period of excess, in order to keep it stored until there appears necessity (Pyne 2005, Maliva and Missimer 2010). The stored water is then recovered from the same well and distributed as drinking, industrial or irrigation water (Maliva et al. 2007).

Water Supply Company Limburg (WML) ran an ASR pilot in the period 2000-2009 in Herten (Limburg, the Netherlands; Figure 2.1), injecting pre-treated drinking water and testing the feasibility and efficiency in terms of recovered water quality and quantity as well as pre-treatment. Water supply in the province of Limburg currently relies on groundwater, bank filtered River Meuse water, and surface water imported from Germany, but WML needs alternatives to cope with expected increases in fluctuations of both demand and water availability.

The first goal of this study was to identify the spatial and temporal patterns in water quality changes during ASR application in a pyritiferous, confined sandy aquifer, which is internationally relevant for many ASR candidate applications. To this end, the Herten ASR pilot was monitored by high frequency sampling of dedicated observation wells with short well screens (1 m) at relatively short distances away from the ASR well (0.1, 8 and 25 m) and the target aquifer received a detailed geochemical inspection. The monitoring system was furthermore set-up to gain insight in near well processes by placing observation wells in the gravel pack of the ASR well, especially during recovery, long storage phases and a 5 years standstill period when these processes mainly occurred. The second goal was to identify and quantify the major hydrogeochemical processes, especially those that might compromise the quality of the recovered water. The third and final goal was to determine the leaching rate of the reactive solid phases, in order to predict when the most cumbersome reactions will fade away and thus when ASR will start to yield water uncompromised by solutes mobilized from the aquifer. To this end, we applied a mass balance approach (REACTIONS+ (Stuyfzand 2010)) that was extended in this paper with a coupled leaching routine. Contrary to existing inverse models like BALANCE (Parkhurst et al. 1982), PHREEQC-2 (Parkhurst and Appelo 1999) or NETPATH (Plummer et al. 1991), all data handling and calculations were performed in an Excel® spreadsheet with macros to run the geochemical routines.

2.2 MATERIAL AND METHODS

2.2.1 Description ASR site and monitoring wells

The Herten ASR trial site is located in the province of Limburg, the Netherlands (Figure 2.1). The site consists of one ASR well and two monitoring wells, M8 and M25 situated at 8 and 25 m distance, respectively (Figure 2.1 and 2.2). The aquifer consists of 4 layers, each with

different hydraulic and geochemical properties (see section 2.3.1). The ASR well, screened between 159.4 and 169 m depth below surface, is equipped with three piezometers inside the gravel pack, at 0.1 m distance (Figure 2.2). Each monitoring well contains three piezometers with a 1 m long screen. The upper piezometers (ASR-1, M8-1 and M25-1) and lower piezometers (ASR-3, M8-3 and M25-3) were monitored throughout the whole study period. The middle piezometers (ASR-2, M8-2 and M25-2) were only monitored during the first 20 months of operation. The piezometers made of PVC have an inner diameter of 25 mm below and 52 mm above 40 m below ground level (BGL), the ASR well has an inner diameter of 226 mm. Clay seals were installed in between each piezometer and where fine grained deposits were pierced through the drilling.

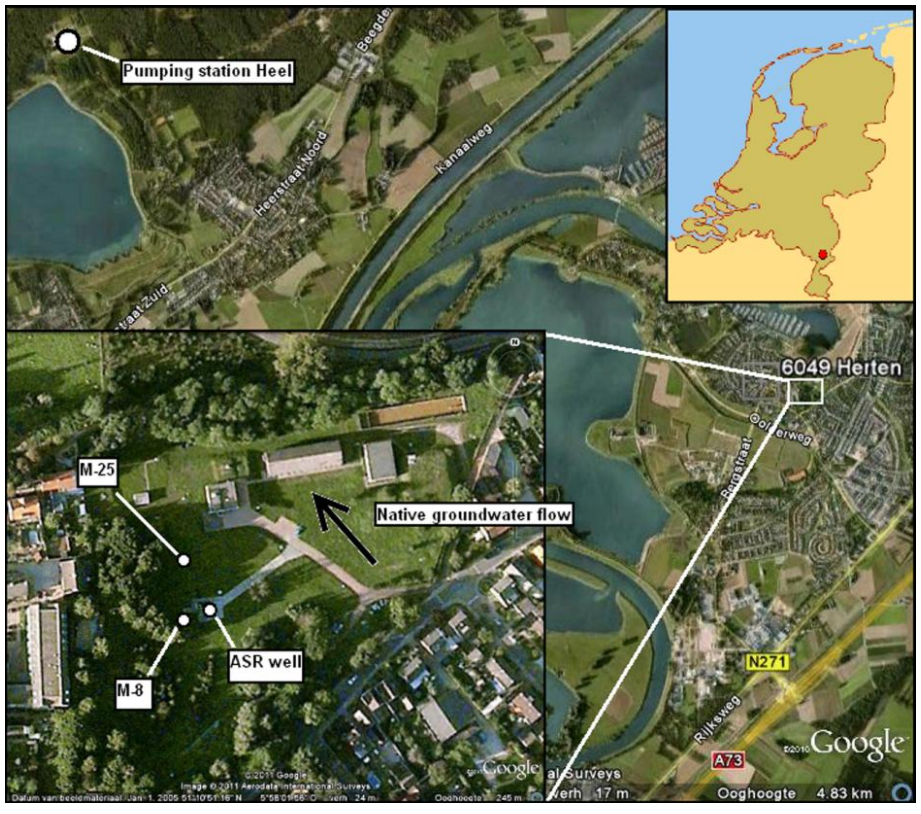

Figure 2.1 Site map showing the location of well fields Herten and Heel, the ASR pilot, and regional groundwater flow direction.

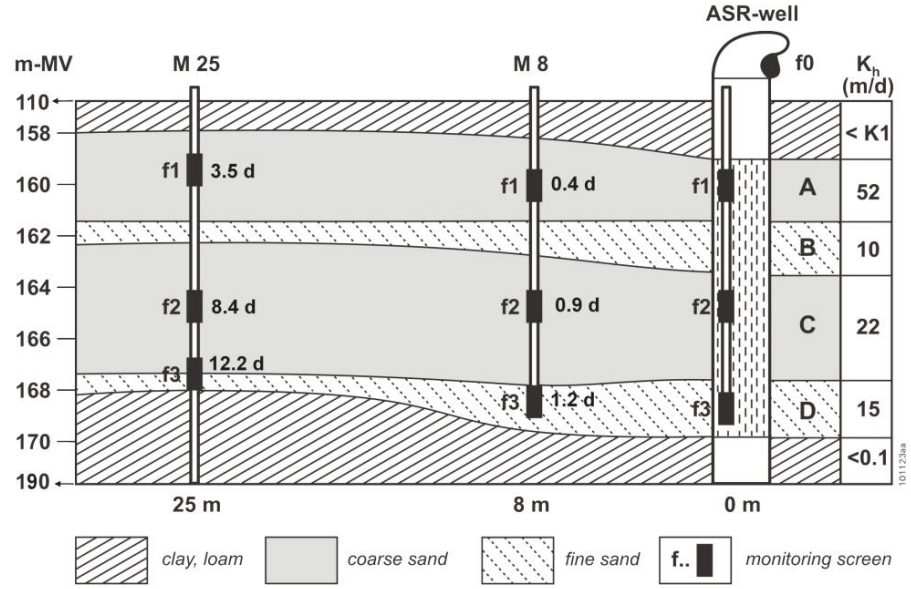

Figure 2.2 Cross section of the aquifer depicting the ASR well and monitor wells M8 and M25. Kh = horizontal hydraulic conductivity. Calculated travel times of injection water to monitor wells in days.

2.2.2 Set-up of the ASR pilots

The experiment lasted for almost 9 years and consisted of two pilots. Drinking water from the Herten pumping station was selected as the source water for the first pilot. This water was a mixture of water pumped from aquifers shallower (50-110 m BGL) and deeper (190-220 m BGL) than the ASR target aquifer. For the second pilot, drinking water from pumping station Heel at 6 km distance (Figure 2.1) was used as this became available via a transport main and was expected to become the source water for ASR application in the area. Table 2.1 presents the mean composition for both source waters. Note the two source water types used during the first pilot showed some distinctive differences in chloride and sulfate concentrations. Injected water quality was rather constant during each pilot, with chloride and sulfate fluctuations of ca. 15%. The injection and pumping rates were, on average, 45 m^3/h.

During the first pilot, five ASR cycles were performed (Figure 2.3a; Table 2.2). Cycles 1, 2 and 5 were undertaken without a storage phase, while during cycle 3 no recovery was performed, and cycle 4 consisted of an injection phase only. In order to study the effects of enhancing the oxidation processes, the source water was enriched with oxygen (from 0.28 to 0.78 mmol/L) during cycle 3, and with nitrate (0.22 mmol $NaNO_3$/L) during cycle 5. The second pilot started after a 5 years stand-still phase with the previously stored bubble still in place, and nine more cycles were performed. The first four cycles were undertaken without a storage phase, whereas the last five cycles consisted of longer injection phases with shorter recoveries.

Table 2.1 Native groundwater quality before initiation of pilot 1, mean groundwater quality in aquifer layers A and D prior to start of pilot 2, mean injection water quality during each pilot, and recovered water quality during cycle 2 (17 days pumping after 1.5 day storage), 13 (28 days pumping after 21 day storage) and 14 (28 days pumping after 91 day storage). C#X = ASR cycle number X.

	temp	EC	pH	O_2	Cl	SO_4	TIC	NO_3	Na	K	Ca	Mg	NH_4	SiO_2	TOC	Fe	Mn	As	Ni	SI-C	SI-S
	(°C)	(mS/m)	lab	(mmol/L)												(µmol/L)				calc.	sid.
NATIVE GROUNDWATER																					
ASR well	13	39.0	7.00	<0.02	0.17	<0.03	6.82	<0.01	0.37	0.04	2.08	0.48	0.005	0.34	0.06	100	4	0.16	0.03	-0.19	0.75
Layer A	12.9	34.5	6.78	<0.02	0.19	<0.03	7.99	<0.01	0.41	0.04	2.14	0.48	0.005	0.35	0.04	112	5	0.18	0.03	-0.39	0.59
Layer D	13.2	35.0	6.78	<0.02	0.17	<0.03	8.09	<0.01	0.35	0.04	2.10	0.51	0.003	0.35	0.03	127	8	0.13	0.03	-0.39	0.66
RESIDUAL ASR BUBBLE 4.2-4.5 years after 1st pilot																					
Layer A[a]	12.4	43.3	7.08	<0.02	0.65	0.47	4.28	<0.01	0.57	0.04	1.80	0.30	0.006	0.24	0.09	30	2	0.31	0.10	-0.37	0.14
Layer D[b]	12.9	52.0	6.87	<0.02	0.59	0.48	6.43	<0.01	0.57	0.04	2.37	0.37	0.012	0.26	0.14	86	12	0.19	0.11	-0.34	0.50
INJECTED WATER (mean for all cycles)																					
1st pilot (Herten water)	11.4	38.8	7.48	0.29	0.61	0.25	3.07	0.02	0.63	0.03	1.83	0.26	<0.05	0.25	0.06	<0.1	<0.1	0.01	0.01	0.04	-2.07
2nd pilot (Heel water)	12.6	45.2	7.45	0.28	1.11	0.64	2.99	0.02	1.05	0.06	1.71	0.27	<0.05	0.14	0.09	<0.1	<0.1	<0.01	0.05	-0.14	-2.20
RECOVERED WATER (ASR well)																					
Herten water. C#2. 17 d	11.8	35.0	7.15	<0.02	0.56	0.31	3.96	<0.01	0.32	0.03	1.84	0.27	0.001			0.18	0.09			-0.31	-2.00
Heel water. C#13. 28 d	13.4	45.0	7.02	<0.02	1.04	0.70	3.20	<0.01	1.00	0.06	1.65	0.27	0.001	0.14	0.10	0.09	3.46	0.01	0.13	-0.59	-2.50
Heel water. C#14. 28 d	12.8	44.4	7.06	<0.02	1.10	0.71	3.10	<0.01	1.04	0.06	1.62	0.28	0.001	0.13	0.07	0.18	6.37	0.01	0.09	-0.58	-2.17

[a] M25-1, average of samples 31 Aug 2006 + 12 Jan 2007
[b] ASR-3, sample taken at 31 Aug 2006

Table 2.2 Numerical description of ASR cycles

1st PILOT	Date interval	Number of days			Volume injected			Volume pumped			Infiltration water
Cycle		Inj	Sto	Rec	m^3/h	m^3 tot	m^3 remaining in aquifer	m^3/h	m^3 tot	m^3 remaining in aquifer	(source & characteristics)
1	16/10/00 - 02/02/01	82	2	26	44.8	88127	88127	43.3	27013	61114	Herten
2	05/02/01 - 21/05/01	54	2	50	44.8	58035	119149	47.6	57168	61981	Herten
3	28/05/01 - 30/09/01	47	79	0	44.0	49587	111568		0	111568	Herten / O_2 enrichment
4	01/10/01 - 17/02/02	140	0	0	38.8	130435	242003		0	242003	Herten
5	18/02/02 - 31/05/02	16	5	82	59.3	22760	264763	62.7	123413	141349	Herten / NO_3 enrichment
2nd PILOT											
6	11/09/07 - 22/10/07	21		21	50.0	25200	166549	50.0	25200	141349	Heel
7	23/10/07 - 10/12/07	21		28	50.0	25200	166549	50.0	33600	132949	Heel
8	08/01/08 - 18/02/08	21		21	50.0	25200	158149	50.0	25200	132949	Heel
9	19/02/08 - 31/03/08	21		21	50.0	25200	158149	50.0	25200	132949	Heel
10	01/04/08 - 26/05/08	27	8	21	50.0	32400	165349	50.0	25200	140149	Heel
11	27/05/08 - 14/07/08	28	14	7	40.0	26880	167029	50.0	8400	158629	Heel
12	15/07/08 - 15/09/08	28	21	14	40.0	26880	185509	50.0	16800	168709	Heel
13	16/09/08 - 22/12/08	49	21	28	40.0	47040	215749	50.0	33600	182149	Heel
14	23/12/08 - 31/05/09	35	91	34	40.0	33600	215749	50.0	40800	174949	Heel

A residual clogging of the ASR well was not observed during the first pilot (Stuyfzand et al. 2005b), and neither during the second. Minor hydraulic resistances on the well screen and the borehole wall during injection disappeared spontaneously during recovery.

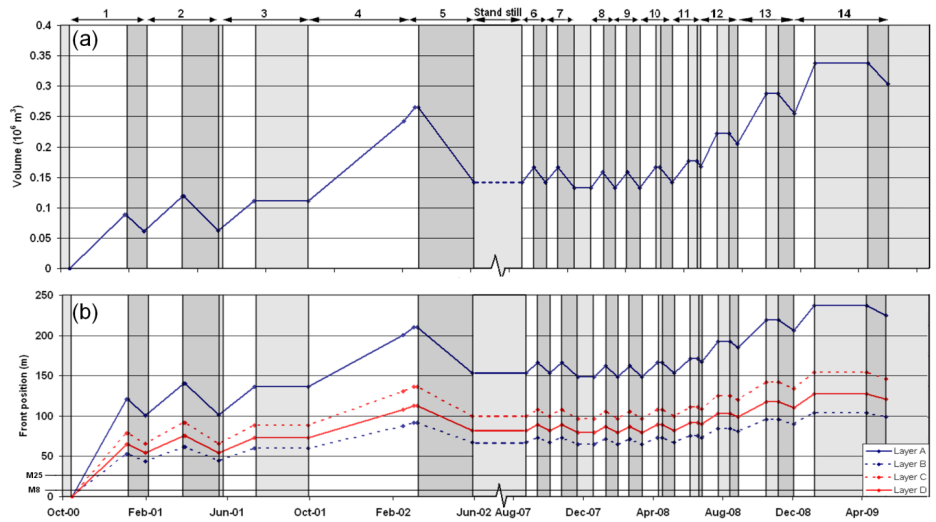

Figure 2.3 (a) Cumulative volume during ASR cycles, (b) Calculated front position of injected water bubble in layers A-D (m distance from ASR well) during both pilots. Effects of bubble drift are not included. Position of monitor wells M8 and M25 indicated (white = injection, light grey = storage, dark grey = recovery).

2.2.3 Geochemical sampling and characterization

Ten PVC cores, each 1 m long (0.10 m diameter) were obtained from the entire depth section of the target aquifer, 159-170 m BGL, when the ASR well was drilled (percussion drilling method). The cores were taken ahead of the drilling bit via a core catcher, and immediately stored in an anoxic stainless steel case under nitrogen atmosphere at 4 °C. They were processed inside a glove-box under nitrogen atmosphere at the TNO-NITG laboratory. Buijs & van der Grift (2001) analyzed 15 subsamples on: (1) total elemental composition (26 elements) using X-ray fluorescence (XRF); (2) total carbon and sulfur (LEKO Induction Furnace Instruments); (3) organic matter and total carbonates by thermogravimetry (TGA at 480, 550, 800 °C); (4) composition of the cation exchange complex by $BaCl_2$ extraction; (5) Cation Exchange Capacity (CEC) by $BaCl_2$ extraction followed by $MgSO_4$ saturation; (6) Mn-oxides, amorphous and crystalline Fe-(hydr)oxides and Al-(hydr)oxides extracted by ammonium oxalate in ascorbic acid; and (7) pyrite deduced from dissolved Fe(II) in the extract after successive hydroxylamine extractions with HCl, HF and HNO_3 (Lord III 1982).

Redox reactivity was determined by incubation experiments (Buijs and Van der Grift 2001) in which the sediment (30 g) was mixed with 50 mL of synthetic ASR source water in 100-mL Duran bottles under a N_2-atmosphere, leaving a constant headspace. These bottles were connected for 30 days at 12°C and subsequently for another 18 days at 26°C to an indirect closed circuit respirometer (Micro-Oxymax). During this period the O_2 consumed and CO_2 produced were measured consecutively in each bottle, resulting in measurements every 6

h for each incubation. The sediment-water slurry was magnet-stirred at 100 rpm to ensure a homogeneous chemical system and enhance oxygen diffusion from the head space to the aqueous phase. In addition, an oxygen-exposure incubation experiment was carried out, where 30 grams of sediment were shaken with 300 mL of simulated ASR source water by continuous bubbling with oxygen for 15 days.

2.2.4 Water sampling and analysis

Throughout the two pilots, all available screens were sampled on a weekly to fortnightly basis for inorganic and microbiological analysis. Three additional sampling sessions were performed during the intermediary stand-still period. During sampling, temperature, pH, electrical conductance (EC) and dissolved oxygen concentration were measured in the field using a multiprobe sensor device (Type WTW Oxi 340, WTW LF 340 and WTW pH 340). The injected and recovered water were sampled through a faucet on the ASR well at ground level. The observation wells were sampled by submersible centrifugal pumps (Eijkelkamp, Agrisearch Equipment). These pumps were permanently fixed in each riser pipe to shorten the refreshing period. Samples were taken after pumping a volume equal to three times the volume of the suction and discharge pipes of the pump (the bottom of the suction pipe was located at screen depth and its internal diameter was 10 mm). The purging lasted considerably shorter than if the whole PVC-riser had to be purged (0.5 instead of 2-3 hours), and allowed simultaneous work (9 piezometers in 2-3 hours).

The samples for analysis of total dissolved concentrations of cations, PO_4, As, and heavy metals were filtered in the field (using 0.45 µm membrane filters) and stored in 50 ml PE bottles. They were acidified with 0.35 ml of 65% suprapur HNO_3 upon arrival in the laboratory in the evening of the sampling day. Samples for O_2 and CH_4 analysis were kept in glass bottles with an airtight cap. All water samples were analyzed by the certified laboratory WLZ in Breda, the Netherlands, using conventional analytical methods.

2.2.5 Hydrological calculations: travel time, pore flushes, bubble front position, and bubble drift velocity

The mean travel time from the ASR well to a monitoring screen in layer N of the target aquifer was calculated for each ASR cycle C as follows, assuming a cylindrical extension in each layer and no lateral flow:

$$t_{N,C} = \frac{n_N \pi r^2 T}{Q_{IN,C} K_{h,N}} \qquad (2.1)$$

where: $t_{N,C}$ = moment of 50% break-through in layer N during ASR cycle C [d]; n_N = porosity of layer N [-]; r = distance from the ASR well [m]; T = transmissivity of the target aquifer, preferably determined by a pumping test [m^2/d]; $Q_{IN,C}$ = mean injection rate as applied during ASR cycle C [m^3/d]; $K_{h,N}$ = horizontal hydraulic conductivity of layer N [m/d].

The number of pore flushes in layer N of the target aquifer at a specific point during any ASR cycle ($PV_{N,C}$) is defined as the number of times the monitoring section between ASR well and that point has been flushed with the source water during cycle C:

$$PV_{N,C} = t_{IN,C} / t_{N,C} \qquad (2.2A)$$

where: $t_{IN,C}$ = duration of injection in ASR cycle C [d]. An important condition for Eq.2.2A is that cycles with $t_{IN,C} < t_{N,C}$ do not count. Likewise the total number of pore flushes since the start of ASR ($PV_{T,N}$) is defined as:

$$PV_{T,N} = \sum_{C=1}^{C=C} \left(\frac{t_{IN,C}}{t_{N,C}} \right) \qquad (2.2B)$$

The front position of the ASR bubble in layer N during ASR cycle C ($R_{N,C}$) was calculated for the same conditions and neglecting diffusion and dispersion, by:

$$R_{N,C} = \sqrt{\frac{\left[\sum_{C=1}^{C=C} (Q_{IN,C} t_{IN,C}) - \sum_{C=1}^{C=C} (Q_{OUT,C} t_{OUT,C}) \right] K_{h,N}}{n_N \pi T}} \qquad (2.3)$$

where: $Q_{OUT,C}$ = mean recovery pumping rate as applied during ASR cycle C [m^3/d]; $t_{OUT,C}$ = duration of recovery pumping in ASR cycle C [d]. An important condition here is that negative $R_{N,C}$ values are to be replaced by zero at any point during the summation.

Bubble drift velocity in layer N ($V_{B,N}$) was calculated for long storage phases, by taking:

$$V_{B,N} = \frac{K_{h,N} \Delta H}{n_N \Delta X} \qquad (2.4)$$

where: $\Delta H/\Delta X$ = regional hydraulic gradient in the target aquifer [m/m].

2.2.6 Quantification of hydrogeochemical reactions

We used the code REACTIONS+ (Stuyfzand 2010), programmed in Excel ® spreadsheet, to quantify and identify through mass balances the main hydrogeochemical processes during the two pilots. The 2010 version was modified by including the calculation of leach factors for reactive mineral phases (section 2.7).

The mass transfer in the water phase always referred to the sum of reactions needed to change the measured average source water composition (input) into the evolved water composition (output) as measured somewhere in the target aquifer with an observation well or, during recovery, with the ASR well. Table 2.3 lists the most important hydrogeochemical reactions. This selection is based on extensive geochemical and hydrochemical monitoring of many injection experiments in Dutch aquifer systems (Stuyfzand 1998a). Several reactions were excluded as they were considered negligible in ASR systems, like the dissolution of

(aluminum) silicate minerals (except for opal) and the dissolution of minerals by strong acids (only CO_2 being active while abundant HCO_3 is acting as a significant acid buffer). Reactions with oxidants that are added to drinking water, like O_3, Cl_2, ClO_2 and NH_2Cl, were not addressed as they are not applied/present in Dutch drinking water.

A fixed oxidation reaction sequence was maintained (in order to simplify the calculations), if parallel oxidation had to be excluded for instance due to lack of sufficient oxidants. The sequence was in descending order: (1) dissolved organic carbon (DOC) + NH_4 in the source water, (2) pyrite (if present), (3) Fe(II) + NH_4^+ + Mn(II) deriving from the exchange complex (during injection phases only and depending on the position of the exchange front), (4) siderite (if present), and (5) sedimentary organic material (SOM). The oxidation of DOC and NH_4 in the input was completely ignored in the ASR Herten case because of negligible NH_4 inputs and observed conservative behavior of very low DOC inputs.

Table 2.3 The most relevant hydrogeochemical reactions for infiltrating (sub)oxic, high alkalinity surface water in an anoxic aquifer (modified after Stuyfzand 2010). Reactions irrelevant to ASR systems in the Netherlands incl. the Herten site show numbers within brackets.

	Process	Reaction equation	No.
Initial	Unsat zone + convection [a]	+ O_2 + CO_2 - CH_4 ; (Cl-out - Cl-in)	(1)
	Nitrification	$2O_2 + NH_4 + 2HCO_3 \rightarrow NO_3 + 2\,CO_2 + 3H_2O$	2
	DOC oxidation [b]	$0.5O_2 + 0.4NO_3 + CH_2O\text{-DOC} \rightarrow 0.6CO_2 + 0.4HCO_3 + 0.2N_2 + 0.8H_2O$	(3)
Redox 1	O_2 oxidizing pyrite	$3.75O_2 + FeS_2 + 4HCO_3 \rightarrow Fe(OH)_3 + 2SO_4 + 4CO_2 + 0.5H_2O$	4
	NO_3 oxidizing pyrite	$2.8NO_3 + FeS_2 + 0.8CO_2 + 0.4H_2O \rightarrow Fe + 2SO_4 + 1.4N_2 + 0.8HCO_3$	5
	O_2 oxidizing Mn-siderite	$(1\text{-}x)O_2 + 4Fe_{(1-x)}Mn_xCO_3 + (6\text{-}2x)H_2O \rightarrow (4\text{-}4x)Fe(OH)_3 + 4xMn^{2+} + (4\text{-}8x)CO_2 + 8xHCO_3$	6
	O_2-reduction	$O_2 + CH_2O \rightarrow CO_2 + H_2O$	7
	NO_3-reduction	$4NO_3 + 5CH_2O \rightarrow 2N_2 + CO_2 + 4HCO_3 + 3H_2O$	8
	MnO_2-reduction	$MnO_2 + 0.5CH_2O + 1.5CO_2 + 0.5H_2O \rightarrow Mn + 2HCO_3$	9
	$Fe(OH)_3$ reduction	$Fe(OH)_3 + 0.25CH_2O + 1.75CO_2 \rightarrow Fe + 2HCO_3 + 0.75H_2O$	10
	SO_4-reduction (FeS_2)	$2SO_4 + 3.5CH_2O + Fe \rightarrow FeS_2 + 2HCO_3 + 1.5CO_2 + 2.5H_2O$	(11)
	CH_4-formation	$CO_2 + 2CH_2O \rightarrow CH_4 + 2CO_2$	(12)
Dissolution	Calcite	$CaCO_3 + CO_2 + H_2O \leftrightarrow Ca + 2HCO_3$	13
	Mg-calcite	$Ca_{(1-x)}Mg_xCO_3 + CO_2 + H_2O \leftrightarrow (1\text{-}x)Ca + xMg + 2HCO_3$	14
	Mn-siderite	$Fe_{(1-x)}Mn_xCO_3 + CO_2 + H_2O \leftrightarrow (1\text{-}x)Fe + xMn + 2HCO_3$	15
	Gypsum	$CaSO_4{\cdot}2H_2O \leftrightarrow Ca + SO_4$	(16)
	Halite	$NaCl \leftrightarrow Na + Cl$	(17)
	Quartz / opal	$SiO_2 + 2H_2O \leftrightarrow H_4SiO_4$	18
Exchange	Fe sorption to $Fe(OH)_3$ [c]	$S\text{-}OH^o + Fe^{2+} \rightarrow S\text{-}OFe(II)^+ + H^+$	19
	SiO_2-sorption [d]	$Fe(OH)_3 + xH_4SiO_4 + H_2O \leftrightarrow Si_xFe(OH)_{(3+4x)}{\cdot}H_2O$	20
	Cation exchange	$aCa + [bFe,cMn,dNH_4]\text{-EXCH} \leftrightarrow bFe + cMn + dNH_4 + [aCa]\text{-EXCH}$	21
	Anion Exchange	$F + [H_2PO_4]\text{-EXCH} \leftrightarrow H_2PO_4 + [F]\text{-EXCH}$	(22)
Redox 2	Oxidation sorbed Fe^{2+} [c]	$S\text{-}OFe(II)^+ + 0.25\,O_2 + 1.5\,H_2O \rightarrow S\text{-}OFe(III)(OH)_2{}^o + H^+$	23
	Oxidation after mixing or	$O_2 + 4Fe^{2+} + 8HCO_3 + 2H_2O \rightarrow 4Fe(OH)_3 + 8CO_2$	24
	desorption cation	$0.5\,O_2 + Mn^{2+} + 2HCO_3 \rightarrow MnO_2 + 2CO_2 + H_2O$	25
	MnO_2 reduction by Fe^{2+}	$MnO_2 + 2Fe^{2+} + 2HCO_3 + 2H_2O \rightarrow 2Fe(OH)_3 + Mn^{2+} + 2CO_2$	26

[a] additional gaseous in/outputs + correction for TDS fluctuations in input
[b] assuming 50% oxidation by O_2 and 50% by NO_3
[c] S-O representing solid iron (hydr)oxide surface
[d] sorption also to other solid phases;

2.2.7 Quantification of the leaching of reactive phases

Since geochemical analyses were only performed prior to initiation of the ASR trial, hydrochemical data were used to approximate the number of pore flushes in layer N needed to practically deplete a specific reactive aquifer constituent within the section of monitoring ($PV_{L,N}$). In this approach (part of REACTIONS+) we assume that: (1) the leaching is a steady process at a constant rate yielding a sharp leaching front; (2) the reactive phase is homogeneously distributed in the aquifer layer; (3) there is no neoformation of the reactive phase within the ASR bubble; and (4) the reaction rate is dictated by one dissolved component which is quantified for that reaction by the hydrochemical mass balance. The calculation of $PV_{L,N}$ is as follows (Stuyfzand 1998b):

$$PV_{L,N} = \left[1 + \frac{f_N (solid)_N}{(prod)_N r_P}\right] \tag{2.5}$$

where:

f_N = conversion factor for mmol/kg into mmol/L in layer N [kg/L];

$$f_N = \left[\frac{\rho_S (1 - n_N)}{n_N}\right] \tag{2.6}$$

and where $(solid)_N$ = content of reactive phase in aquifer layer N [mmol/kg d.w.]; ρ_S = density of aquifer matrix, assumed equal in each layer [2.65 kg/L]; n_N = porosity of layer N [-]; $(prod)_N$ = concentration of reaction product in layer N [mmol/L]; r_P = reaction coefficient defined as the proportion of the stoichiometric coefficients of the solid and product, see Table 2.3 [-].

For example, in case of pyrite leaching, FeS_2 is the solid, $(SO_4)_{OUT}$ - $(SO_4)_{IN}$ is the product, and r_P is 0.5 (conform reactions 4 and 5 in Table 2.3). As most reactions slow down during ASR this approach yields an underestimation of $PV_{L,N}$, if the concentration of the dissolved component is taken at the beginning (after 5-20 PVs when redox reactions normally are at maximum; (Stuyfzand 1998a)).

When data are available for each cycle, the leaching progress is better approached by discretization as follows:

$$f_N (solid)_{N,t} = f_N (solid)_{N,0} - \sum_{C=1}^{C=C} \left[(prod)_{N,C} r_P PV_{N,C}\right] \tag{2.7}$$

where: *N,t* = in layer N at time t = t; *N,0* = in layer N at time t = 0 ($PV_{T,N}$ = 0); *C* = ASR cycle number.

Under all conditions pertaining to Eqs.2.1, 2.2 and 2.7, the relative position of the leaching front in layer N at any moment between the injection and an observation well ($R_{L,N}$ in %) becomes:

$$R_{L,N} = 100 \sqrt{\frac{PV_{T,N}}{PV_{L,N}}} \tag{2.8}$$

2.2.8 Quantification of oxidant consumption

Oxidants, in this case O_2 and NO_3 (not SO_4), are consumed during ASR operations, mainly during the injection and storage phases. Experimental data indicate that the consumption rate declines over time in both cases and follows first-order decay. Therefore the concentration of oxidant C at time t since the start of either injection ($C_{t,INJ}$) or storage ($C_{t,STO}$) is approximated for an observation well as follows, ignoring dispersion (Figure 2.4):

$$C_{t,INJ} = (C_{IN} - \Delta C) - (C_{IN} - \Delta C - C_0)\, e^{-\ln 2\,(t - t50)\,/\,T½INJ} \quad (2.9)$$

$$C_{t,STO} = (C_{IN} - \Delta C - C_0)\, e^{-\ln 2\, t\,/\,T½STO} + C_0 \quad (2.10)$$

where: C_{IN}, C_0 = concentration of oxidant C in respectively the source water and in the water before injection or after prolonged storage [mmol/L]; ΔC = steady concentration decrease during injection after reaching equilibrium [mmol/L]; $T½_{INJ}$, $T½_{STO}$ = half life of oxidant C during respectively injection and storage [d]; t = time since start of injection or storage [d]; t_{50} = travel time to observation well [d].

In the present anoxic aquifer C_0 was always zero. The terms $T½_{INJ}$ and $T½_{STO}$ refer to different oxidant consuming processes: normally $T½_{INJ}$ includes microbiological processes near the borehole wall and oxidation of sorbed Fe(II), Mn(II) and NH_4 in addition to oxidation of SOM, pyrite or siderite, whereas $T½_{STO}$ only includes the oxidation of SOM, pyrite or siderite.

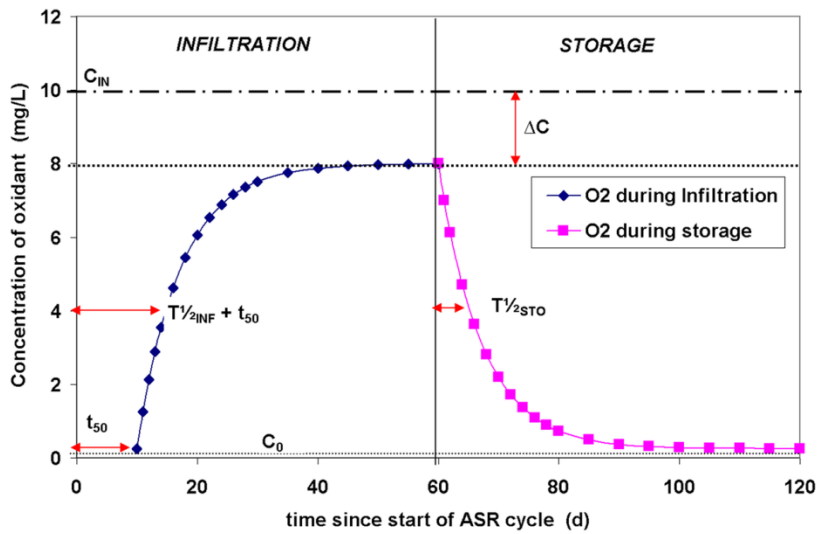

Figure 2.4. Example of oxidant breakthrough during an ASR source cycle and subsequent oxidant consumption during storage, with visualization of selected parameters to calculate the oxidant concentration over time. In this example $T½_{INF} = T½_{STO} = 5$ days. Dispersion ignored.

2.3 RESULTS: THE AQUIFER PRIOR TO ASR APPLICATION

2.3.1 Geochemical characterization

The deeply anoxic target aquifer is composed of uncemented fluvial sands of Pliocene age and is further subdivided into four layers (A-D, Table 2.4, Figure 2.2). SOM (<0.25-8% d.w) and pyrite (0.05-0.25% d.w) concentrations were measured in all aquifer layers. Carbonate minerals are practically lacking in layers A and C, while low contents are present in layers B and D (0.4-0.6% d.w.). These carbonates, apparently a Mg-calcite ($Ca_{0.88}Mg_{0.12}CO_3$) and Mn-siderite ($Fe_{0.9}Mn_{0.1}CO_3$), are mainly concentrated in clay and gyttja lenses in layers B and D. The chemical composition of these carbonate solid solutions was indirectly concluded from the CO_2 production against the O_2 consumption in the micro-oxymax experiments, XRF- and TGA-analyses, analyses of the final solution remaining after the micro-oxymax experiment, and the results of the ASR pilots.

Table 2.4 Target aquifer characterization. Average values for 1-6 core samples.

Layer	Unit	A	B	C	D
Depth	m BGL	158.6 - 162.2	162.2 - 163.3	163.3 - 168	168 - 170
No. Samples	n	4	1	4	6
K_h	m/d	52	10	22	15
Clay size fraction[a]	% d.w	1.1	1.6	0.8	1.4
CEC	meq/kg	6.7	124.8	23.8	32.6
SOM	% d.w	0.08	8.03	1.31	1.76
Pyrite[b]	% d.w	0.05	0.25	0.07	0.09
Calcite[c]	% d.w	<0.02	0.13	<0.01	0.15
Siderite[d]	% d.w	<0.06	0.45	<0.07	0.25
Fe speciation					
Total	% d.w	0.04	0.56	0.05	3.13
Hydroxide (by oxalate)	% d.w	-	0.30	-	0.62
Exchangeable	% d.w	<0.001	0.011	0.002	0.002
Pyrite	% d.w	0.02	0.12	0.03	0.04
Siderite	% d.w	<0.01	0.22	<0.03	0.12
Mn speciation					
Total	ppm	3	77	7	621
Hydroxide (by oxalate)	ppm	-	33	-	103
Exchangeable	ppm	0.2	4.8	0.7	1.0
Siderite	ppm	<3	40	<6	133
Incubation experiment (Oxymax)					
dO_2 12°C	mmol/L/d	0.03	0.14	0.08	0.08
dCO_2 12°C	mmol/L/d	0.03	0.12	0.06	0.22
dCO_2/dO_2 12°C	mmol/L/d	0.86	0.86	0.73	2.88
dO_2 26°C	mmol/L/d	0.09	0.34	0.18	0.17
dCO_2 26°C	mmol/L/d	0.06	0.18	0.09	0.44
dCO_2/dO_2 26°C	mmol/L/d	0.61	0.53	0.48	2.63

[a] grain size fraction < 2µm
[b] containing As, Co, Ni and Zn
[c] containing Mg
[d] containing Mn

The average aquifer porosity was estimated at 0.3, and the average trace element composition of FeS_2 is approximated with $Fe_{0.94}Co_{0.007}Ni_{0.02}Zn_{0.04}S_2As_{0.0087}$. This composition was derived from the slope of strong linear correlations between the FeS_2 content on the one hand and the total As, Co, Ni and Zn contents on the other hand. Similar values were observed by Savage et al. (2000), Cremer et al. (2003), and Price & Pichler (2006).

The selective extractions of Fe- and Mn-phases showed that layers B and D also contain Fe- and Mn-(hydr)oxides. This could be realistic but also an artifact due to potential oxygenation of the samples notwithstanding measures to keep the samples anoxic, and due to dissolution of siderite in the extractant (ammonium oxalate in ascorbic acid).

Redox reactivity results by respirometry (Table 2.4) indicated that aquifer layers A-C are dominated by O_2 reaction with pyrite and SOM, and that aquifer layer D is dominated by reaction with pyrite, SOM and siderite. This was deduced from the average dCO_2/dO_2 ratio (where dCO_2 is the CO_2 production and dO_2 the O_2 consumption). A value around 1 indicates SOM oxidation (Eq.7 in Table 2.3), 1.1 indicates pyrite oxidation with HCO_3 as the acid buffer (Eq. 4 in Table 2.3), and 4 indicates siderite oxidation (Eq. 6 in Table 2.3). Obviously the siderite in layer B did not manifest itself as in layer D, probably due to its much higher SOM and pyrite content.

2.3.2 The native groundwater

The native groundwater, before initiation of pilot 1 in 2000, is characterized as pH-neutral, calcareous, deeply anoxic, oligohaline, unpolluted water of the $Ca(HCO_3)_2$-type (Table 2.1). Ferrous iron concentration was rather high (0.1 mmol/L) and methane low (<2 µmol/L). Hydrochemical stratification in the aquifer was minimal, showing slightly higher Fe(II), Mn(II), Mg and HCO_3 concentrations in the deeper parts, notably in layer D (Table 2.1). The water was generally slightly undersaturated with respect to calcite (Saturation Index = -0.35) and oversaturated with respect to siderite (Saturation Index = +1.0).

2.4 RESULTS: PATTERNS AND PROCESSES DURING ASR

2.4.1 Hydrological behavior of the ASR bubble

Average travel times (Figure 2.2) to each monitoring screen were calculated using Eq.2.1 taking an average injection rate of 45 m^3/h (which remained fairly constant during both pilots). These results were compared to the observed chloride breakthrough patterns (from 0.2 to 0.6 mmol/L; Table 2.1), albeit sampling was performed every 7 days. One day after initiation of injection, 100% and 70% breakthrough was observed in wells M8-1 and M8-3, respectively, while 8 days later, 100% and 60% breakthrough was observed in wells M25-1 and M25-3, respectively. These observed chloride breakthrough values within layers A and D at 8 and 25 m from the ASR well agreed with the calculated estimates of travel time.

Bubble drift must have been significant during the 5.3 years long storage phase in between cycles 5 and 6. Calculations with Eq. 2.3 and a SE-NW regional hydraulic gradient in the aquifer of 0.00043 indicate that the bubble has drifted in a NW direction by about 140 m in layer A (0.07 m/d), and about 40 m in layer D (0.02 m/d). These distances are smaller than the front position of the ASR bubble after cycle 5 (153 and 82 m in layers A and D, respectively) as calculated with Eq. 2.2 (Figure 2.3b). The position of well M25 in the regional groundwater flow domain also gives it an extra advantage of 25 m compared to M8 and the ASR well (Figure 2.1). 8 months before pilot 2 (cycle 6) started, Cl concentrations were identical to those in the water injected during the first pilot, indicating that Herten ASR water was still present around all wells.

We deduce from Figure 2.3b that, after the breakthrough of Herten water in cycle 1, groundwater sampled from all wells (M8, M25 and ASR) during pilot 1 consisted exclusively of Herten source water. This also held (M25 more than for M8) during the early phases of injection cycles 7-10 and the late phases of recovery cycles 6-10 during pilot 2 when Heel water was used as source water. As of cycle 11, groundwater sampled from all wells was exclusively Heel source water. This was confirmed by Cl data showing a clear difference between Herten and Heel source water (0.6 versus 1.1 mmol/L; Table 2.1).

2.4.2 Overview of water quality changes

Tables 2.5 and 2.6 present an overview of the quality of source water as sampled from the monitoring wells after 62-63 days of storage, and during injection and recovery (after only 1.5 days of storage), respectively. Conservative behavior was observed for Na, K, Cl, NO_2 (< 4 µmol/L), CH_4 (< 2 µmol/L) and dissolved organic carbon (DOC). The main quality changes relate to redox reactions of the oxic source water with anoxic aquifer constituents, notably pyrite, SOM, exchangeable Fe(II), NH_4^+, and Mn(II) in all layers, and Mn-siderite only for layer D (and B). As a consequence of these reactions, concentrations of the oxidants O_2 and NO_3 steadily declined during aquifer passage and, if still present, during storage, while concentrations increased of SO_4 (up to 0.34 mmol/L increase from pyrite), Fe(II) (up to 71 µmol/L increase mainly from desorbing Fe and Mn-siderite), Mn(II) (up to 20 µmol/L increase mainly from desorbing Mn and Mn-siderite), As, Co and Ni (up to 0.04, 0.52 and 0.26 µmol/L, respectively, all from pyrite).

The most important redox reactions (4, 6 and 7 in Table 2.3) produced acidity, which was partly buffered by conversion of abundant HCO_3 into CO_2 and by slow dissolution of carbonate minerals. As a result, the pH and calcite saturation index (SI_C) decreased by 0.1-0.7 units as compared to the injected water, resulting in subsaturation with respect to calcite (SI_C = -0.14 to -0.8) in all aquifer layers. The concentration of Ba was augmented (up to 0.46 µmol/L increase) probably by desorption, whereas the concentration of silica slightly decreased (up to 0.08 mmol/L), possibly by sorption to neoformed iron(hydr)oxides (reaction 20 in Table 2.3).

Table 2.5 Overview of water quality changes of source water in aquifer layers A, C and D after 62-63 days of storage, during ASR cycles 3 (Herten drinking water with 0.5 mmol/L extra O_2) and 14 (Heel drinking water without extra O_2). PVs = pore volumes flushed with source water. Water temperature 13-14°C during both cycles. PVs C# = PVs during Cycle 3 or 14; PVs EXCH = PVs needed to complete cation exchange.

Observation	Aquifer	Dist[a]	t_{50} [a]	PVs			pH	SI	O_2	NO_3	Cl	SO_4	TIC	DOC	Na	K	Ca	Mg	SiO_2	As	Ba	Co	Fe	Mn	NH_4	Ni	Zn
point	Layer	m	d	Total	C#	EXCH		Calcite	mmol/L											µmol/L							
Cycle #3 after 62 days storage																											
Input C#3	A-D	0.0	0.0				7.58	0.15	0.78	0.02	0.63	0.27	3.86	0.06	0.36	0.03	1.82	0.26	0.25	0.04	0.36	0.02	0.09	0.09	1.39	0.03	0.07
ASR-1	A	4.7	0.1	1491	509	10	7.10	-0.25	0.00	0.00	0.59	0.42	4.52	0.10	0.35	0.03	2.05	0.30	0.26	0.05	0.44	0.02	2.69	0.91	7.21	0.03	0.04
M8-1	A	9.3	0.5	378	129	10	7.15	-0.22	0.00	0.00	0.54	0.47	4.34	0.10	0.37	0.03	2.10	0.29	0.24	0.03	0.37	0.03	0.09	0.82	1.39	0.14	0.20
M25-1	A	20.3	2.3	77	13	10	6.75	-0.69	0.00	0.00	0.56	0.61	4.49	0.10	0.37	0.03	2.03	0.28	0.22	0.03	0.52	0.15	0.36	1.64	1.39	0.12	0.12
ASR-2	C	2.0	0.1	3612	919	32	7.10	-0.25	0.00	0.01	0.59	0.48	4.52	0.08	0.37	0.04	2.10	0.32					0.72	0.73	1.39		
M8-2	C	8.2	1.0	206	53	32	7.00	-0.34	0.00	0.00	0.56	0.48	4.71	0.12	0.37	0.03	2.16	0.30	0.25	0.04	0.38	0.53	0.18	2.37	1.39	0.29	0.35
M25-2	C	23.0	7.1	26	5	32	6.75	-0.67	0.00	0.00	0.59	0.48	4.85	0.07	0.37	0.04	1.95	0.29	0.17	0.01	0.80	0.14	9.49	4.19	1.39	0.07	0.12
ASR-3	D	1.4	0.0	5127	1223	44	6.90	-0.63	0.00	0.00	0.59	0.47	5.38	0.06	0.40	0.04	2.30	0.35	0.27	0.03	0.63	0.02	0.72	1.09	3.33	0.03	0.04
M8-3	D	8.1	1.2	146	35	44	6.70	-0.38	0.00	0.00	0.54	0.54	6.49	0.11	0.37	0.04	2.47	0.34	0.22	0.01	0.55	0.19	7.46	7.22	1.39	0.19	0.29
M25-3	C+D	23.7	10.9	17	4	44	6.80	-0.54	0.00	0.00	0.62	0.45	4.80	0.07	0.35	0.04	1.84	0.36	0.19	0.03	0.73	0.02	71.62	4.19	4.43	0.03	0.08
Cycle #14 after 63 days storage																											
Input C#14	A-D	0.0	0.0				7.50	-0.04	0.28	0.02	1.11	0.64	2.93	0.09	0.60	0.06	1.71	0.27	0.14	0.01	0.23	0.01	0.10	0.09	1.39	0.05	0.10
ASR-1	A	4.7	0.1	4636	205	10	7.32	-0.19	0.00	0.00	1.07	0.69	3.44		0.60	0.06	1.80	0.29	0.15	0.03	0.31	0.03	15.22	20.02	19.40	0.01	0.15
M8-1	A	9.3	0.5	1184	52	10	7.03	-0.50	0.03	0.01	1.13	0.72	3.45		0.60	0.06	1.77	0.28	0.15	0.01	0.25	0.07	0.09	0.36	1.39	0.10	0.18
M25-1	A	20.3	2.3	249	5	10	7.03	-0.57	0.00	0.00	1.10	0.74	3.05		0.60	0.06	1.60	0.27	0.13	0.01	0.47	0.11	1.43	2.18	1.39	0.09	0.43
ASR-3	D	1.4	0.0	14433	494	44	7.11	-0.80	0.00	0.00	1.10	0.67	4.02		0.62	0.06	1.90	0.31	0.16	0.03	0.33	0.03	5.91	17.29	19.40	0.02	0.17
M8-3	D	8.1	1.2	442	15	44	6.86	-0.34	0.00	0.00	1.10	0.66	4.33		0.62	0.06	1.87	0.31	0.12	0.01	0.36	0.04	8.59	11.83	1.39	0.08	0.43
M25-3	C+D	23.7	11.0	52	2	44	6.85	-0.52	0.00	0.00	1.13	0.67	3.44		0.60	0.05	1.50	0.28	0.13	0.01	0.69	0.02	51.93	3.82	3.88	0.05	0.43

[a] distance traveled or travel time in aquifer, taking bubble drift into account
NO_2 < 4 µmol/L
CH_4 < 2 µmol/L

Table 2.6 Overview of water quality changes of source water in aquifer layers A, C and D, during respectively injection and recovery of ASR cycle #2. Situation reflects particle tracking in each layer since day 38 of cycle 2, with 1.5 days of storage during days 55-56. Water temperature 9-12°C.

Observation	Aquifer	Dist[a]	t_{50} [a]	day[b]	PVs		pH	O_2	NO_3	Cl	SO_4	TIC	DOC	Na	K	Ca	Mg	SiO_2	As	Ba	Co	Fe	Mn	NH_4	Ni	Zn
point	**Layer**	**m**	**d**	**No.**	**Total**	**C#**							**mmol/L**										**µmol/L**				
During injection. cycle #2																											
Input C#2	A-D	0	0	38			7.40	0.29	0.02	0.63	0.27	3.98	0.06	0.36	0.03	1.82	0.26	0.25	0.01	0.38	0.01	0.1	0.1	1.4	0.01	0.06
M8-1	A	8	0.36	38	349	123	7.35	0.22	0.01	0.51	0.34	3.95	0.05	0.32	0.03	1.88	0.28	0.25	0.03	0.33	0.10	0.1	0.1	1.4	0.12	0.21
M25-1	A	25	3.5	41	36	13	7.15	0.01	0.00	0.45	0.48	4.00	0.05	0.32	0.03	1.91	0.26	0.24	0.05	0.50	0.01	15.0	0.4	1.4	0.01	0.04
M8-2	C	8	0.85	39	148	53	7.25	0.18	0.01	0.45	0.38	4.05	0.05	0.32	0.03	1.93	0.28	0.24	0.04	0.32	0.25	0.1	0.1	1.4	0.17	0.17
M25-2	C	25	8.3	46	15	5	7.00	0.03	0.00	0.48	0.40	4.31	0.05	0.32	0.03	1.80	0.27	0.21	0.02	0.56	0.01	46.6	1.7	2.4	0.01	0.04
M8-3	D	8	1.24	39	101	35	7.15	0.11	0.01	0.45	0.41	4.21	0.05	0.32	0.03	1.91	0.27	0.22	0.03	0.39	0.01	11.6	0.7	1.4	0.03	0.11
M25-3	C+D	25	12.1	50	11	4	6.80	0.01	0.00	0.54	0.34	4.75	0.06	0.32	0.03	1.67	0.30	0.20	0.03	0.57	0.01	60.9	2.4	2.8	0.01	0.04
During extraction. cycle #2																											
ASR-0	A-D	0	0	74	0	5-14	7.15	0.01	0.00	0.56	0.35	4.04		0.32	0.03	1.84	0.27					0.2	0.1	1.4		
ASR-1	A	0.1	0.0001	74	2235200	14	7.10	0.01	0.00	0.51	0.46	3.95	0.05	0.32	0.03	1.86	0.28					0.5	0.1	1.4		
M8-1	A	8	0.36	74	349	14	7.10	0.01	0.00	0.48	0.42	4.03	0.06	0.32	0.03	1.90	0.28					0.4	0.5	1.4		
M25-1	A	25	3.5	71	36	14	7.15	0.00	0.00	0.56	0.35	3.98										16.3	0.9	1.4		
ASR-2	C	0.1	0.0001	74	946673	6	7.10	0.03	0.00	0.51	0.39	4.14	0.08	0.32	0.03	1.86	0.27					0.2	0.1	1.4		
M8-2	C	8	0.9	73	148	6	7.15	0.02	0.00	0.51	0.35	4.09	0.06	0.32	0.03	1.83	0.27					0.1	0.5	1.4		
M25-2	C	25	8.3	66	15	6	7.15	0.01	0.00	0.59	0.28	4.17										50.1	2.0	1.4		
ASR-3	D	0.1	0.0002	74	644769	5	7.05	0.02	0.00	0.62	0.30	4.24	0.03	0.32	0.03	1.66	0.27					0.1	0.4	1.4		
M8-3	D	8	1.24	73	101	5	7.05	0.01	0.03	0.51	0.35	4.24	0.04	0.32	0.03	1.78	0.27					17.9	2.0	1.4		
M25-3	C+D	25	12.1	62	11	5	7.05	0.00	0.00	0.54	0.33	4.14										68.0	3.1	3.9		

[a] distance traveled or travel time in aquifer
[b] since start of cycle 2
NO_2 < 4 µmol/L
CH_4 < 2 µmol/L

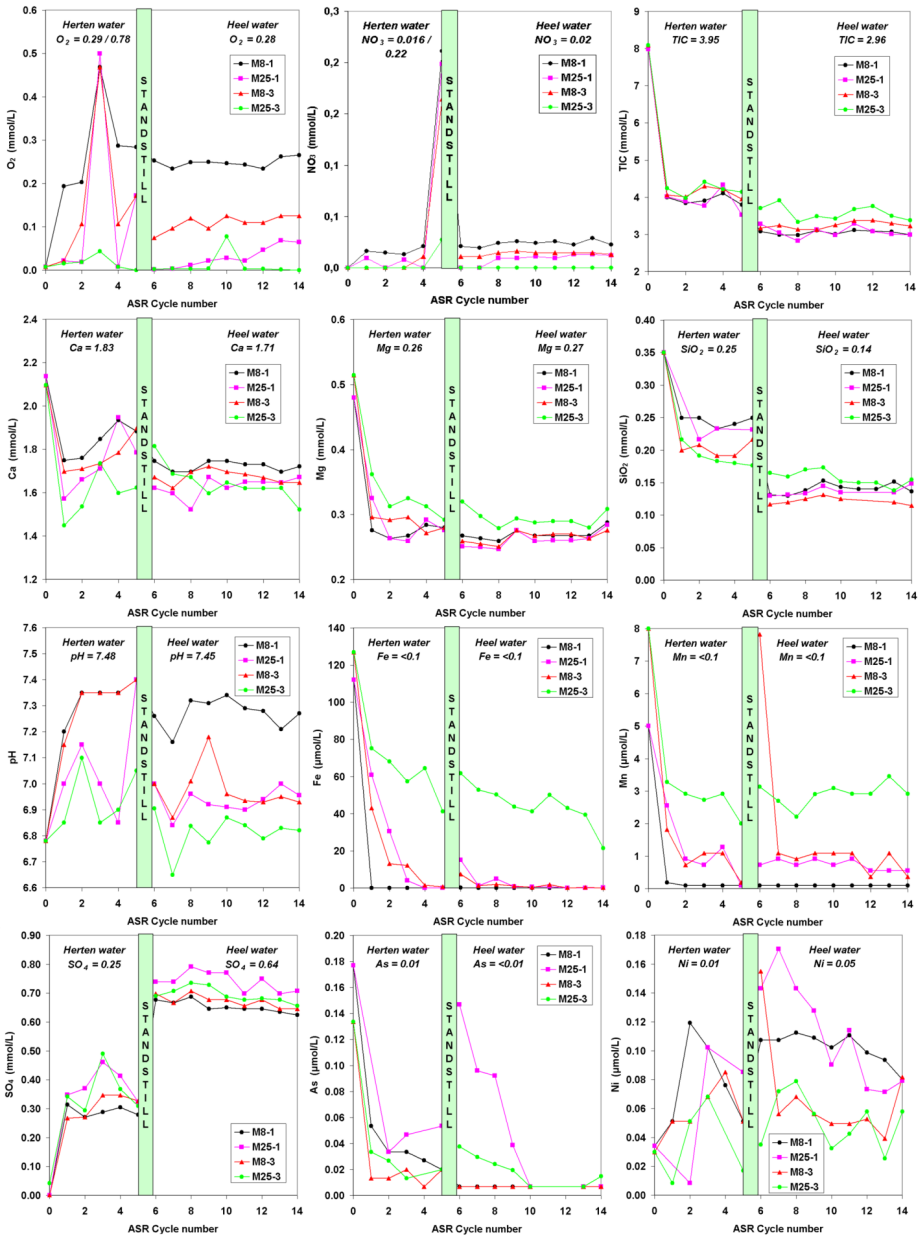

Figure 2.5 Quality changes of source water in layer A (M8-1 and M25-1) and D (M8-3 and M25-3) during ASR cycles 1-14, each after 14-21 days of injection. Mean composition of source water (Herten and Heel) indicated. Cycle 0 = native groundwater, Cycle 3 with O_2 added, cycle 5 with $NaNO_3$. Standstill period from June 1, 2002 till September 10, 2007.

2.4.3 Spatial hydrogeochemical patterns

Differences between layers A, C, and D

The hydrogeochemical behavior of aquifer layers A, C and D is compared in Table 2.5 for two ASR cycles executed after a relatively long storage phase during which (nearly) all oxidants were consumed. Due to about 2 months of bubble drift, the observation wells in the ASR well displayed the quality of water that reached a distance of ca. 4.7 (ASR-1), 2.0 (ASR-2) and 1.3 m (ASR-3) from the ASR well during injection. Differences between layers A and D are also derived from Figure 2.5, which shows the quality changes during the injection phase of successive ASR cycles.

The general picture is that pyrite oxidation was most pronounced in layers A and C, as evidenced by the strongest increase for SO_4, As and Ni, and that the magnitude of Mg-calcite and Mn-siderite dissolution was highest in layer D as demonstrated by the strongest increase for TIC, Mg, Ca and Mn(II). Layer A showed hardly any dissolution of carbonate minerals. Layer C showed an intermediate position between layers A and D, regarding pyrite oxidation and Mg-calcite dissolution. These differences in reactivity agree with their geochemical composition (Table 2.4) indicating a relation between mineral content and oxidation/dissolution reactions.

Layer D always displayed the largest SiO_2 sink and lowest pH (Figure 2.5), probably due to the highest production rate of reactive ferrihydrite. Layer D also showed contrasting behavior of Ca, which increased in concentration during storage (Table 2.5) due to Mg-calcite dissolution, and decreased during the first weeks of injection (Figure 2.5) due to cation-exchange for Fe(II), Mn(II) and NH_4.

Effects of travel distance during injection

During injection, a longer travel time and distance in the aquifer (from ASR via M8 to M25) result in a clear increase of SO_4, Fe(II), Mn(II) and Ba concentrations and a clear decrease of O_2, NO_3 and SiO_2 concentrations in the source water (Table 2.6, Figure 2.5). This behavior is also demonstrated by Fe(II) and Mn(II) in Figure 2.6. We explain this behavior by (1) relatively slow reaction kinetics with respect to travel time and (2) less flushing with source water with longer travel time. O_2 and NO_3 were consumed in between 8 and 25 m away from the ASR well for most cycles of pilot 1. Cation-exchange reactions (Fe(II), Mn(II) and Ba exchanging for Ca) were still ongoing even during ASR cycle 14 at M25-3 experiencing the lowest number of pore flushes. The reason is not only that more pore flushes would be needed to equilibrate the original exchange complex with source water (compare PVs in Table 2.5), but also that the exchange complex gets reloaded during each recovery, especially with Fe(II) and Mn(II) deriving from pyrite and Mn-siderite dissolution.

Effects of travel distance during recovery

During recovery only few water quality parameters continued to change in the aquifer as a function of travel distance (from M25 via M8 to the ASR well). Concentrations of Fe(II)

and Mn(II) strongly declined, whereas pH slightly decreased (Table 2.6). These changes are best interpreted with “particle tracking” during the first two cycles in layers A and C. Figure 2.6 shows the Fe(II) and Mn(II) concentration against the time the water resided in the aquifer. The Fe(II) and Mn(II) concentrations clearly decreased when the groundwater moved backwards from M25 via M8 to the ASR well. We explain this decrease with sorption of Fe(II) and Mn(II) to neoformed ferrihydrite (reaction 19 in Table 2.3), a well known process acting during subsurface iron removal. We also conclude from Figure 2.6 that the Fe(II) and Mn(II) mobilization diminished between consecutive cycles 1 and 2.

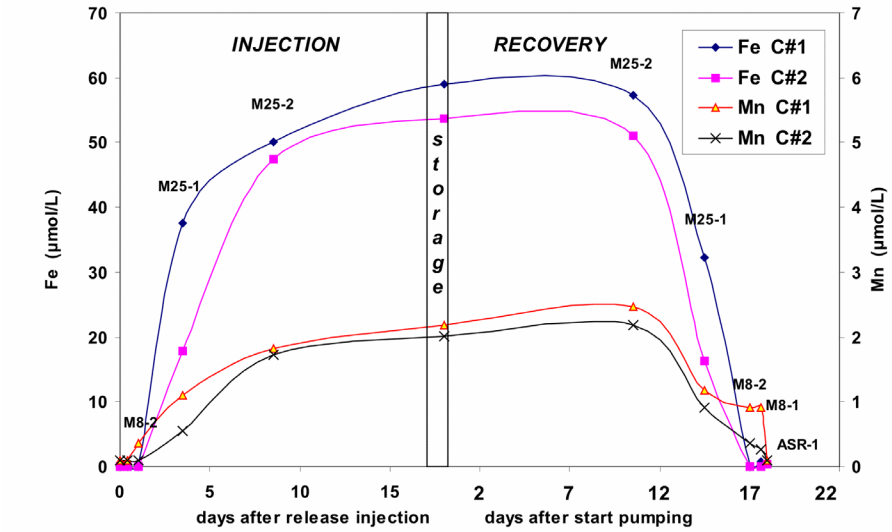

Figure 2.6 Particle tracking in layers A and C, with only 1 day of storage (data based on Table 2.6). During injection Fe and Mn concentrations increase along the flow path away from the ASR well, while they decrease on their return during pumping. The decrease is due to sorption processes similar to those acting during SIR. C#2 = ASR cycle No. 2.

Anomalies in the ASR proximal zone

Remarkable anomalies were observed in observation wells ASR-1 and ASR-3, situated in the gravel pack of the ASR well at 0.1 m distance (Table 2.5, Figure 2.7). Concentration changes in the source water were small during injection as the travel time through inert gravel was extremely short (10 sec). During recovery, the changes as observed between M25 and M8 continued between M8 and ASR-1/3 as expected (see previous subsection ‘Effects of travel distance during recovery’). During storage, however, anomalously high concentrations of Fe(II), Mn(II), As, NH_4 and TIC gradually showed up in ASR-1/3, being best displayed in the data of long storage phases like for cycle 14 (Table 2.5; Figure 2.7) and in the standstill period (Figure 2.5 and 2.7).

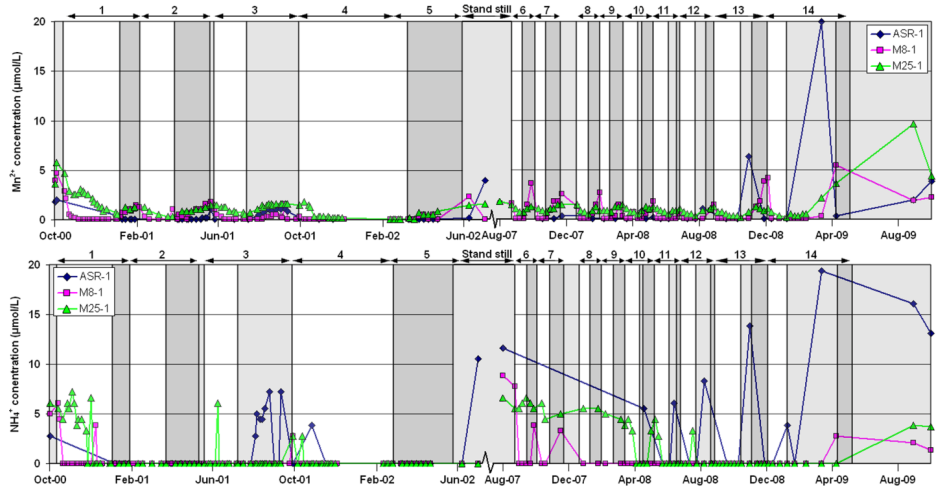

Figure 2.7 Plot of Mn and NH_4 concentrations in layer A over time, showing an anomalous Mn and NH_4 mobilization only in monitor well ASR-1 within the ASR proximal zone. 1-14 = cycle numbers; colored bands: white = injection, light grey = storage, dark grey = recovery.

We explain this anomalous increase with the removal of oxidants by neoformed organic material in the ASR proximal zone, where micro-organisms grow during injection and die away during storage (Stuyfzand et al. 2002, Vanderzalm et al. 2002, Stuyfzand et al. 2005a). During storage, anoxic conditions arise close to the ASR well (<8 m distance) due to biomass mineralization as evidenced by TIC increases and by NH_4 concentration peaks which were not detected elsewhere in the aquifer (Figure 2.7). Concomitantly Fe and Mn (hydr)oxides are reductively dissolved, after their deposition in the proximal zone either after oxidation of pyrite, siderite and desorbing Fe(II) or by introduction of colloidal $Fe(OH)_3$ flocks that formed during drinking water treatment. As a result standards are exceeded for a.o. Fe(II), Mn(II) and NH_4 during the first 50-200 m^3 (6-22 well volumes) of abstracted water the during recovery phase (Stuyfzand et al. 2005a).

2.4.4 Temporal hydrogeochemical patterns

Effects of subsequent ASR cycles and increasing pore volumes

A general decrease in mobilization of SO_4, Fe(II), Mn(II), As, Co (results not shown) and Ni, and a slow breakthrough of O_2 and NO_3 was observed with subsequent ASR cycles and within cycles in all aquifer layers (Figure 2.5). The decrease of SO_4 becomes more obvious during pilot 2 as the source concentration is more constant. Mn(II) on the contrary only shows a general concentration decrease during pilot 1. The leaching of reactive aquifer constituents and their coating with reaction products are held responsible for the gradual extinction of hydrogeochemical reactions, and thereby for the progressive reduction of water quality changes of the source water (see section 2.5).

The long standstill phase (2002-2007) has set back the oxygenation state of the aquifer system, because Fe(II), Mn(II) and As restart, during pilot 2, with relatively high concentration levels in all well screens. Well M25-3 shows, however, a remarkably stable quality (Figure 2.5). This corresponds with its very low total number of pore flushes by the end of cycle 14 ($PV_{T,D}$ = 47) and with layer D's high content of reactive constituents (Table 2.4). The return to anoxic conditions during the standstill period, especially in the ASR proximal zone, is linked to mineralization of neoformed SOM that accumulated around the ASR well, as discussed earlier.

Effects of storage time

During storage, anoxic conditions in aquifer layer D returned within about 25 days, leading to increasing concentrations of SO_4, Fe(II), Mn(II), TIC, Ca and Mg, and more irregular increments of As, Co and Ni, while SiO_2 remained more or less constant (Figure 2.8). The Mg content of dissolving Mg-calcite ($Ca_{0.88}Mg_{0.12}CO_3$) was derived by the strong positive correlation between TIC, Ca and Mg in M8-3 during storage (Figure 2.8). Water quality changes resulting from storage were more pronounced closer to the ASR well, and were larger during cycle 14 than during cycle 3 (Figures 2.5 and 2.7). These observations probably reflect higher biomass accumulation closer to the ASR well and for later cycles when Heel (containing 50% more DOC) instead of Herten source water was used.

Chemical incompatibility is noted during the first 70 days of cycle 3, when both O_2 and Fe(II) show significant concentration levels (Figure 2.8). Probably both constituents only become mixed in the monitoring well screen and are extracted from different aquifer parts as the Fe(II) oxidation rate is very high at pH 6.7-7.4. Cycle 3, despite its special nature due to the addition of ca. 0.5 mmol O_2/L during injection, showed quality changes that are representative for what normally happens during storage phases longer than 1 month, and for what happens during the long standstill periods.

2.5 RESULTS: QUANTIFICATION OF HYDROGEOCHEMICAL PROCESSES

2.5.1 Results of mass balances

A detailed mass balance analysis was performed using REACTIONS+ for wells M8-1 and M25-1 in layer A and for M8-3 and M25-3 in layer D, in order to quantify the main hydrogeochemical reactions occurring during the injection phase of each cycle. The oxidized amounts of pyrite, SOM, siderite, and concentrations of desorbing anoxic cations (Fe(II), Mn(II), and NH_4^+) were calculated, as well as the amounts of dissolved siderite and calcite. The results of the mass transfer calculations are presented in Figure 2.9, whereas the contribution of the different reductants to overall O_2 consumption is shown in Figure 2.10. For interpretation it should be born in mind that: (1) O_2 was the principal oxidant with a far minor role for NO_3; (2) O_2 was only partly consumed in wells M8-1, M25-1, and M8-3

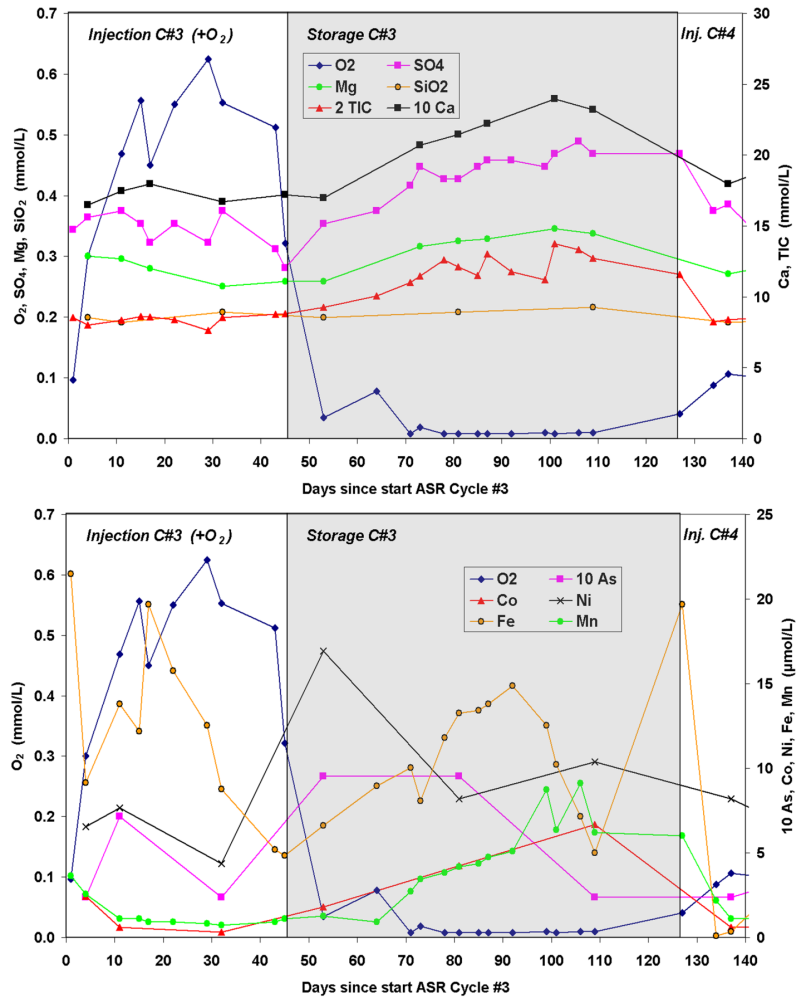

Figure 2.8 Detailed plot of major and minor constituents of source water in M8-3 (layer D), during cycle 3 when about 0.5 mmol O_2/L was added to the source water. Cycle 3 lacked a recovery phase.

during practically all cycles; whereas (3) O_2 was completely consumed in well M25-3 during practically all cycles; and (4) minor changes should not be given importance because of the following. Irregularities in Figures 2.9 and 2.10 are mainly due to inaccuracy of the mass balances resulting from unnoticed fluctuations in input concentrations (especially regarding Ca and SO_4), analytical noise (especially for pH, TIC and O_2), and differences in time (14-21 days since start of injection). The time differences relate to data availability and differences in length of injection periods. Nevertheless some interesting general conclusions are drawn.

Mass transfers by oxidation and dissolution were, for each layer, higher in the distant wells (M25-1 and M25-3; Figure 2.9), because of the slow oxidation kinetics and consequently

slow acidity production resulting in dissolution of carbonate minerals. On the other hand, the nearby wells M8-1 and M8-3 already showed a clear downward trend in pyrite oxidation due to aquifer leaching (section 2.5.2) and starting in cycle 8. This leaching also seems to reduce the extent of pyrite oxidation in the distant wells, which are still remote from the leaching front. This is explained by an increased amount of SOM oxidation due to less O_2 capture by pyrite in the leached zone.

Siderite and calcite showed, on average, more dissolution (both) and oxidation (siderite only) during cycles 6-14 than during cycles 1-5. This is partly related to larger degrees of subsaturation for these minerals in Heel (used during cycles 6-14; Table 2.1) versus Herten source water. Calcite depletion is noticed at M8-1 in aquifer layer A, probably starting after cycle 6, bearing in mind that values <0.05 mmol $CaCO_3$/L (Figure 2.9) may as well be equal to zero due to analytical noise.

The oxidation of adsorbed / desorbing Fe(II), Mn(II) and NH_4^+ played a role in decreasing order for M8-3 (19.4%; average value of all cycles), M25-3 (10.7%), M25-1 (7.4%) and M8-1 (0%), as shown in Figure 2.10. This process was more important in layer D than A, because of its five times higher CEC (Table 2.4), the closer position of the O_2 front due to a higher reactivity of this layer, and the lower flow velocity through this layer, with consequent better reloading of the exchange complex with 'reduced' cations during recovery.

Several peaks show up in Figure 2.9. The ones for pyrite and SOM oxidation during cycles 3 and 5, respectively, are explained in the section below. The others for siderite and calcite dissolution/oxidation during cycles 6-7 are hard to explain.

Effects of dosing O_2 or NO_3

The addition of 0.5 mmol O_2/L to Herten water (already containing 0.28 mmol O_2/L) during cycle 3 led to clear peaks in pyrite and SOM oxidation only in the remote wells M25-1 and M25-3 (Figure 2.9). The high rates of flow versus reaction explain the lack of enhancement of these processes in M8-1 and M8-3. Absence of synchronous peaks in siderite and calcite dissolution suggests these reactions were also kinetically limited. During the storage phase of cycle 3, pyrite and SOM oxidation continued, with larger effects in wells at 8 than at 25 m distance since the O_2 concentration was larger near the ASR well; in well M8-3 it took about 25 days until all O_2 was depleted (Figure 2.8). The continued oxidation resulted in dissolution of carbonates (Mn-siderite and Mg-calcite) leading to a steady increase in Ca, Mg, TIC, Fe(II) and Mn(II) concentrations (Figure 2.8).

The dosing of 0.22 mmol $NaNO_3$/L to Herten water (already containing 0.02 mmol NO_3/L) during cycle 5 did not enhance oxidation and dissolution except for M25-3. Slow reaction kinetics explains the arrival of NO_3 in all observation wells with the exception of M25-3 where denitrification by SOM was 100% in agreement with the large SOM content in layer D (Table 2.4).

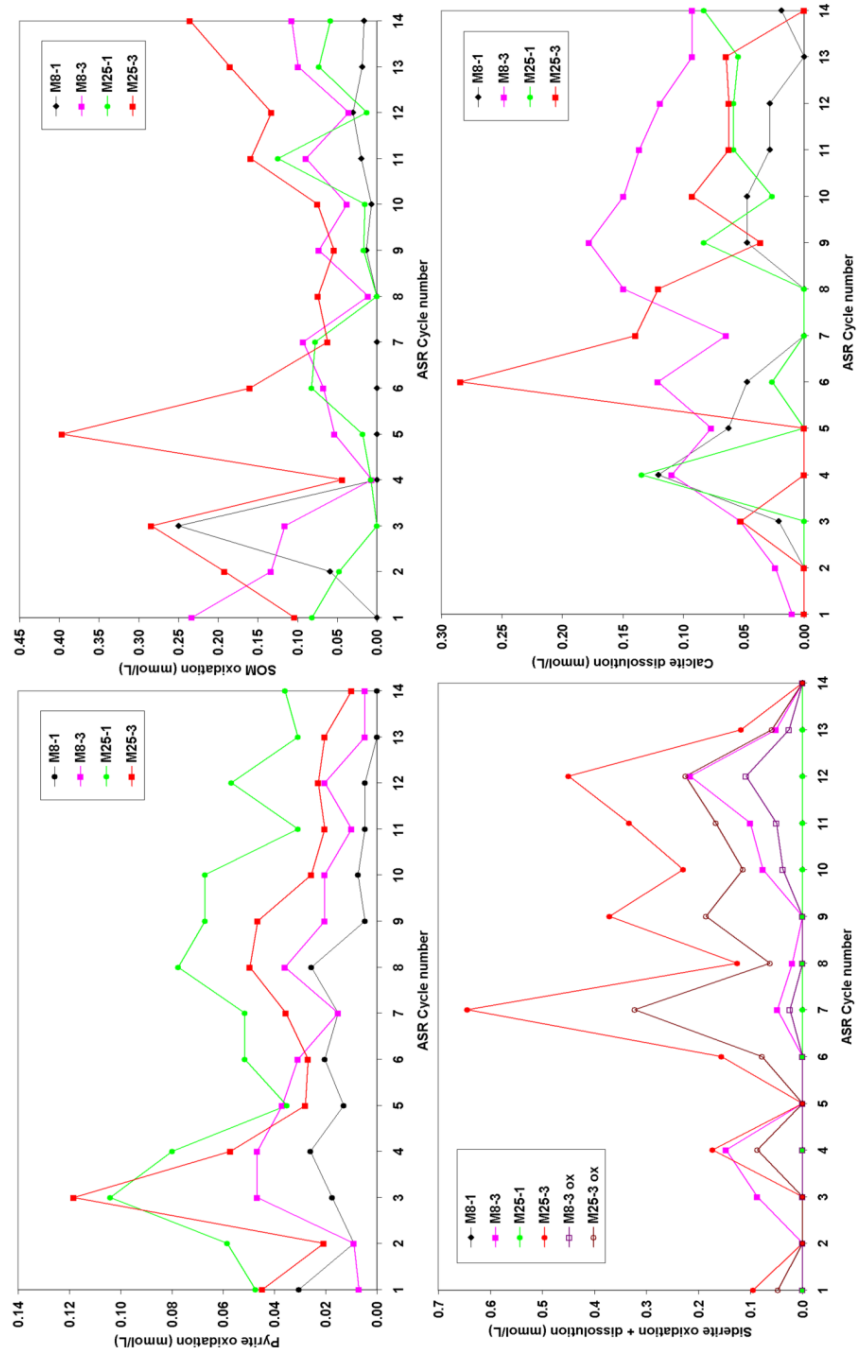

Figure 2.9 Amounts of oxidation and dissolution of reactive aquifer components (pyrite, SOM, siderite and calcite) during the injection phases (14-21 days after start) of the 14 ASR cycles at the Herten pilot. Source water consisted of Herten (cycles 1-5) and Heel drinking water (cycles 6-14). About 0.5 mmol O_2/L was added during cycle 3, and 0.22 mmol $NaNO_3$/L during cycle 5.

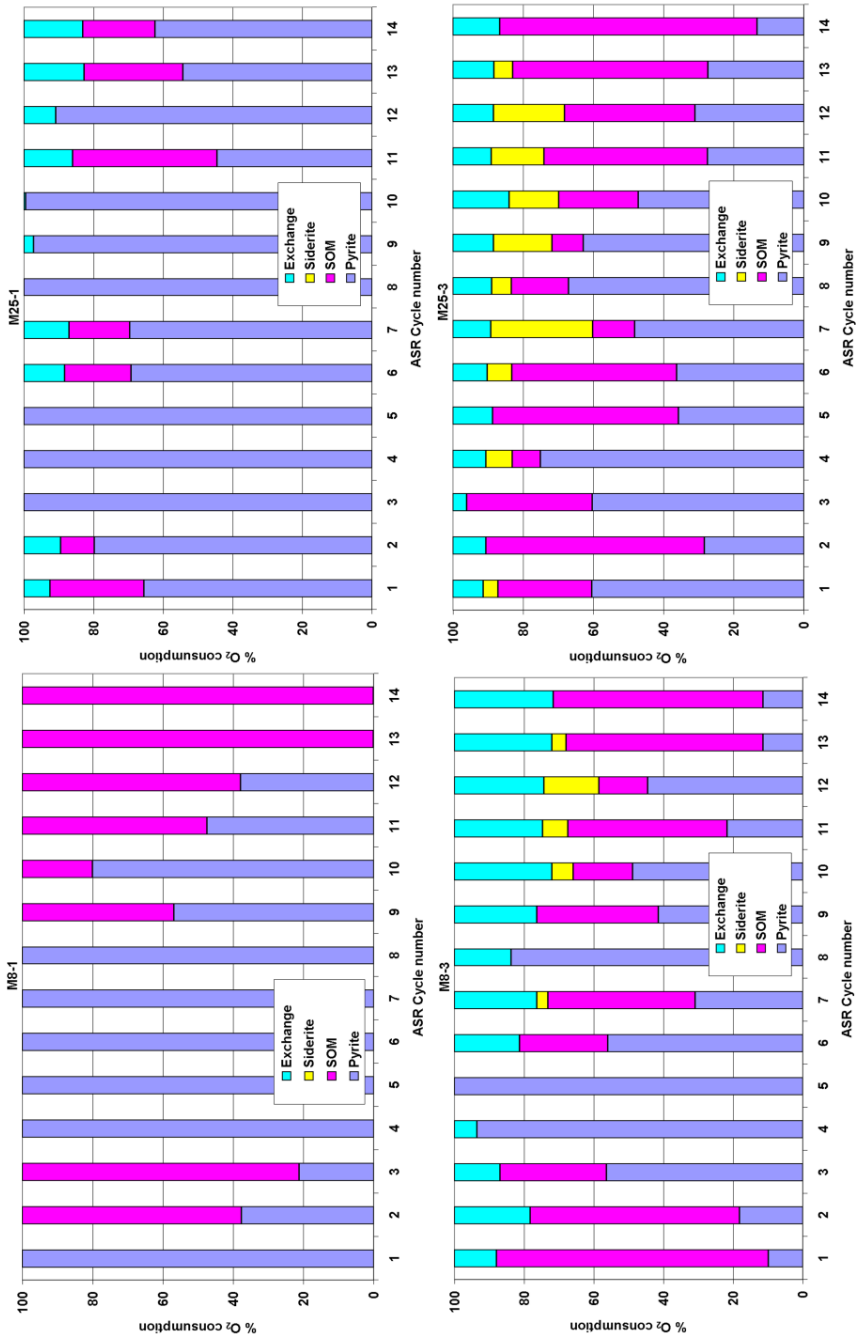

Figure 2.10 Proportion of the different reductants consuming oxygen during subsequent injection phases (14-21 days after start) in aquifer layer A (M8-1, M25-1; without siderite) and layer D (M8-3, M25-3; containing siderite). Exchange indicates the oxidation of exchangeable Fe^{2+} + Mn^{2+} + NH_4^+.

2.5.2 Aquifer leaching

The leaching progress of pyrite, calcite, and siderite shown in Figure 2.11 was calculated for aquifer layers A (M8-1 and M25-1) and D (M8-3 and M25-3), with Eq. 2.7 (showing the leaching progress) and with Eq. 2.5 (showing the leaching end point). The leaching rates (values not shown), defined by the average slope of the leaching progress with pore volumes, indicate that leaching proceeded at a faster rate in (1) layer A because of lower initial mineral contents (Table 2.4), and (2) in the remote wells (M25-1, M25-3), as compared to the respective proximal ones, due to high rates of flow versus reaction enhancing the reaction progress for these most distant wells. Whether leaching was practically completed in an observation well also depended, of course, on the number of pore volumes, which by the end of cycle 14 was as follows: 1600 (M8-1), 462 (M8-3), 164 (M25-1) and 47 (M25-3).

The leaching appears as a relatively steady process. It was retarded, however, for calcite during cycles 1-3 probably due to mineral supersaturation of the source water, and it slowed down for pyrite after cycle 8 possibly due to pyrite coating with ferrihydrite and slower reaction kinetics for the remaining pyrite crystals (being larger or less accessible).

Calculations were also performed for SOM (not shown in Figure 2.11). At the end of cycle 14, SOM was leached in layer A by 33% in M8-1, and 5% in M25-1, and in layer D by 1.3% in M8-3 and 0.2% in M25-3. A significant SOM fraction is likely recalcitrant to oxidation speeding up the leaching progress but not accounted for in our calculations. The

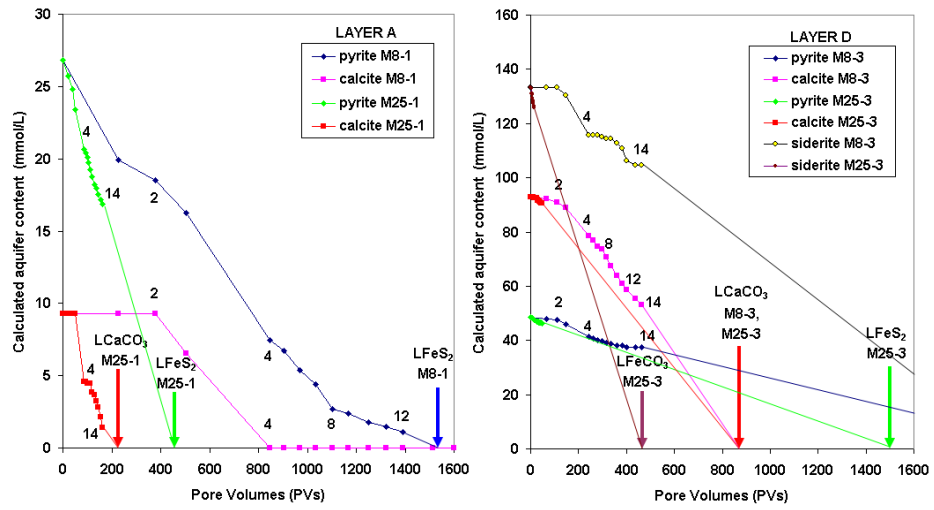

Figure 2.11 Calculated leaching of aquifer layer A (left; no siderite present) and D (right) during ASR cycles 1-14 and thereafter. Calculated is the average mineral content between the ASR well and the observation well. LX = leach factor for X. Numbers within graph refer to cycle number.

neoformation of SOM can, however, not be neglected in the well proximal zone as indicated in section 2.4.3.

2.5.3 Rates of oxidation reactions

Oxygen was the main oxidant with its consumption rate mainly depending on the position in the aquifer system (aquifer layer, distance to ASR well), input level (enhanced in cycle 3), and ASR phase (injection or storage). Consumption parameters (explained in Figure 2.4) are compared in Table 2.7, while a close up of O_2 behavior is shown in Figure 2.12 for cycles 13 and 14, when O_2 was not only measured by periodical sampling but also on-line during continuous, low flow pumping of wells M8-1 and M25-1. Figure 2.12 confirms that retarded, partial O_2 breakthrough during injection and O_2 consumption during storage is approximated by first-order decay.

We conclude from Table 2.7 that the average daily O_2 consumption ($\Delta O_2/t_{50}$) during injection cycles 13-14, compared to injection cycles 1-2, decreased in all observation wells, but most in aquifer layer A and especially in the wells closer to the ASR well: 57% in M8-1, 30% in M25-1, 21% in M8-3 and 11% in M25-3. This trend is in line with the observed leaching rates. The daily O_2 consumption declines with travel distance in each aquifer layer, as a result of lower O_2 concentrations downgradient from the ASR well. These lower concentrations result in a lower rate due to first-order dependence on O_2 concentration. The decreasing delay in O_2 breakthrough during injection ($T½_{INF}$ decreasing) and the decreasing O_2 consumption

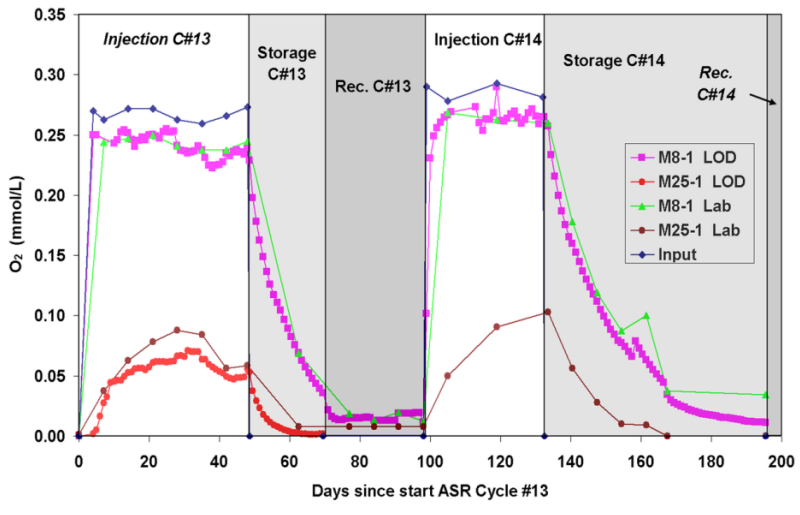

Figure 2.12 Oxygen behavior in aquifer layer A during ASR cycles 13 and 14, with distinction between samples analyzed in the laboratory (Lab) and on-line measurements in a flow-through cell (LOD).

rate during storage ($T½_{STO}$ increasing) are best displayed by M8-3. Also these parameters testify of progressive leaching. O_2 addition during cycle 3 raised the daily consumption during injection in all wells, but had a variable effect on $T½_{INF}$ and $T½_{STO}$.

Table 2.7 Parameters of oxygen behavior during selected ASR cycles, for observation wells M8-1 and M25-1 in aquifer layer A, and for M8-3 and M25-3 in aquifer layer D. Parameters explained in Figure 2.4.

Parameter	Unit	ASR Cycle #				
		1	2	3	13	14
$O_{2(IN)}$	**mmol/L**	**0.29**	**0.29**	**0.78**	**0.27**	**0.29**
M8-1						
t_{50}	d	0.36	0.36	0.36	0.40	0.40
$O_{2(0)}$	mmol/L	<0.01	<0.01	<0.01	<0.01	0.02
$\Delta O2 / t_{50}$	mmol/L/d	0.102	0.120	0.648	0.034	0.061
$T½_{INF}$	d	10	0.5	<0.5	<3	<3
$T½_{STO}$	d	-	-	18	7.9	12.6
M25-1						
t_{50}	d	3.5	3.5	3.6	3.9	3.9
$O_{2(0)}$	mmol/L	<0.01	<0.01	<0.01	<0.01	<0.01
$\Delta O_2 / t_{50}$	mmol/L/d	0.076	0.078	0.086	0.052	0.056
$T½_{INF}$	d	5	5	17	3.5	3
$T½_{STO}$	d	-	-	5	3.4	7.4
M8-3						
t_{50}	d	1.2	1.2	1.3	1.4	1.4
$O_{2(0)}$	mmol/L	<0.01	<0.01	<0.01	<0.01	0.02
$\Delta O_2 / t_{50}$	mmol/L/d	0.146	0.138	0.160	0.104	0.121
$T½_{INF}$	d	31	7	3	<3	<3
$T½_{STO}$	d	-	-	<3	<7	7
M25-3						
t_{50}	d	12.1	12.1	12.3	13.6	13.6
$O_{2(0)}$	mmol/L	<0.01	<0.01	<0.01	<0.01	<0.01
$\Delta O_2 / t_{50}$	mmol/L/d	0.024	0.024	0.060	0.021	0.021
$T½_{INF}$	d	>>68	>>38	20	>>36	>>23
$T½_{STO}$	d	-	-	<1	-	-

2.6 DISCUSSION

2.6.1 Drinking water standards

After injection of drinking water which met all drinking water standards, the water recovered frequently showed exceedances of the acceptable value for O_2 (<0.063 mmol/L), Mn(II) (>0.9 µmol/L) and $SI_{CALCITE}$ (<-0.2), and only once for Ni (>0.34 µmol/L). Exceedance for O_2 and $SI_{CALCITE}$ were judged of minor importance due to easy remediation by either admixing or aeration. Exceedance for Mn(II) (up to 6.4 µmol/L), however, was judged in 2009 essential for the nogo decision on ASR application in the province of Limburg. Concentrations above the standard have been associated with unusual look (brownish-red color), taste, or smell

of the water. This decision may be revoked when mitigation of the Mn mobilization in the aquifer can be demonstrated, for instance, by dosing the source water with a pH buffer such as Na_2CO_3 or NaOH. A test with dosing a pH buffer was not performed in Herten, but will be simulated in later work with column studies and reactive transport modeling. In addition, the low Fe(II) concentrations and pH around 7.1 in the recovered water appear favorable to examine the effects of a simple post-treatment procedure involving aeration and rapid sand filtration. Also, the mixing of recovered water with higher quality water might help solving the Mn(II) and calcite undersaturation problems.

2.6.2 Comparison with related studies

The Herten ASR experiment compares well with a deep well injection experiment conducted at the DIZON pilot plant near Someren (Southern Netherlands) in 1994 (Stuyfzand et al. 2005a). During injection, acidic conditions due to oxidation reactions with pyrite and SOM were buffered by HCO_3^- already present in the source water. As opposed to the Herten aquifer, As, Co and Zn did not mobilize, probably due to more efficient scavenging by neoformed Fe (hydr)oxide precipitates. Nevertheless, serious concerns regarding the feasibility of future ASR applications were posed by the relatively rapid return to anoxic conditions in the injected bubble after 2.5 years of uninterrupted flushing with oxic source water. Mineralization of biomass was deduced from the high concentrations of dissolved Fe(II), Mn(II), NH_4, and TOC (0.21, 0.022, 0.19, and 0.35 mmol/L, respectively) in recovered water after 106 days of storage similar as for the Herten pilot. These concentrations dropped to safe limits after about two hours of pumping, testifying of the limited extent of this zone.

At Bolivar, South Australia, a full-scale ASR trial was undertaken injecting oxygenated, nutrient-rich reclaimed water into a carbonate aquifer (Vanderzalm et al. 2006). Likewise, during storage, raised Mn(II) and Fe(II) concentrations were observed in groundwater from the ASR well, whereas at the 4 m radius there was no evidence for their mobilization. This led to the conclusion that Fe (hydr)oxides and Mn oxides were used as electron-acceptors for the mineralization of biomass around the ASR well. As the storage phase progressed, DOC in the ASR well increased presumably due to metabolism of previously immobile organic matter via the decay of biomass and any remaining particulate organic matter. This metabolism also resulted in nutrient increase, such as NH_4 and P.

The aquifer type, its mineralogy, and the manganese problems encountered here compare well with various ASR systems in the Potomac-Raritan-Magothy aquifers in New Jersey (Lucas et al. 1994). Iron-bearing minerals such as pyrite, marcasite, and siderite were exposed to oxygenated drinking water resulting in oxidation reactions and increased dissolved iron concentrations. In the Chesapeake ASR system in Virginia USA (Ibison et al. 1995), elevated Mn(II) concentrations were recorded in the recovered water due to the presence of a Mn-bearing siderite in the aquifer. In both cases, pH adjustment methods of the source water (using NaOH) were successful in gradually delaying the onset of dissolved Fe(II) and Mn(II) in the recovered water.

Arsenic did not pose major concerns for the smooth operation of the Herten ASR pilot despite the aquifer's pyritiferous nature, usually associated with high As concentrations (Stuyfzand 2001, Jones and Pichler 2007, Vanderzalm et al. 2007). The manganese rich nature of the siderite on the other hand, proved to be the decisive factor that hindered the success of the entire pilot. This marks the importance of a detailed initial site exploration which takes into account not only the main existing phases but also their trace chemical composition.

2.7 CONCLUSIONS

We identified the main hydrogeochemical processes taking place during ASR applications in a typical anoxic sandy aquifer and we addressed their role on water quality changes. The water quality was mainly changed by oxygen consumption with pyrite, sedimentary organic matter, and exchangeable Fe(II), NH_4^+, and Mn(II), and, if present, the consequent dissolution of carbonate minerals (calcite, siderite, ankerite). Anomalously high concentrations of Fe(II), Mn(II), NH_4, As, and TIC were observed in the ASR proximal zone during storage, pointing to oxidant consumption by neoformed organic material.

The mobilization of SO_4, Fe(II), Mn(II), As, Co, and Ni was observed to decline during consecutive ASR cycles, probably due to leaching of reactive aquifer constituents (pyrite producing SO_4, Fe, As, Co, and Ni; siderite producing Fe(II) and Mn(II)) and their coating with reaction products. Fe(II) and Mn(II) removal during recovery was demonstrated by particle tracking and pointed at sorption to neoformed ferrihydrite.

We used a mass balance approach to compare and quantify the leaching progress of reactive minerals with subsequent pore volumes in two aquifer layers. In layer A, where initial mineral contents were lower and flow velocities higher, we calculated a full depletion of pyrite and calcite in the proximal observation well (8 m) but not in the more distant one (25 m) implying that the leaching front is now situated somewhere inbetween. In layer D, on the other hand, complete leaching was not identified.

Moreover, the presence of Mn-siderite in layer D hindered the smooth operation of the ASR plant. Manganese mobilization led to frequent drinking water standard exceedances in this pilot. This, in combination with expected treatment difficulties and high costs convinced water utility WML in 2009 to abandon the idea of ASR application in this type of aquifer. Yet this may not be the end of it, because methods such as pretreating the aquifer or lowering the aggressivity of the source water towards siderite (by adding a pH buffer like Na_2CO_3 or NaOH) were not tested. Future column tests and reactive transport modeling may demonstrate that ASR is feasible in that way.

CHAPTER 3

Reactive transport modeling of the Herten ASR pilot to assess long-term water quality improvements and potential solutions

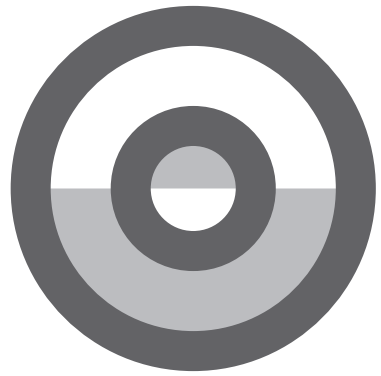

Published as:

Antoniou, E. A., Stuyfzand, P. J. and Van Breukelen, B. M. (2013). Reactive transport modeling of an aquifer storage and recovery (ASR) pilot to assess long-term water quality improvements and potential solutions. Applied Geochemistry 35(0): 173-186.

ABSTRACT

This reactive transport modeling study presents a follow up to the mass balance-based identification and quantification of the main hydrogeochemical processes that occurred during an aquifer storage and recovery (ASR) trial in an anoxic sandy aquifer (Herten, the Netherlands). Kinetic rate expressions were used to simulate oxidation of pyrite, soil organic matter (SOM), and ferrous iron, and dissolution of calcite and Mn-siderite. Cation exchange, precipitation of Fe- and Mn-(hydr)oxides, and surface complexation were treated as equilibrium processes. The PHREEQC model was automatically calibrated with PEST to observations from the first ASR cycle, and was then allowed to run for all 14 cycles to evaluate its long term performance. A sensitivity analysis was conducted to find the most controlling model parameters. Pyrite was ranked as the most important reductant, followed by SOM, whereas Fe(II) was least important. Moreover, the pH and oxygen gradients were found to enhance the rate of pyrite over SOM oxidation with distance away from the ASR well. The increasing sorption capacity of precipitating Fe-hydroxides was reflected by the decreasing Fe(II) concentrations with subsequent cycles whereas Mn(II) showed a tendency to mobilize during recovery and remain above standards. Oxidation and dissolution rates were found to depend on travel time and injection rate as well as on the presence or absence of flow. Oxygen enrichment of the injection water increased oxidation rates and therefore accelerated the aquifer's leaching from its reactive species. We specifically focused on impeding the release of Mn(II) to the groundwater, a process that acted as a restraining factor for the feasibility of ASR application at this site. The undesirable side-effects of oxygen enrichment as well as the Mn(II) issues were found to be partly suppressed by enriching the source water with pH buffers according to scenario simulations.

Keywords: ASR, aquifer recharge, reactive transport modeling, pyrite, siderite, manganese

3.1 INTRODUCTION

Aquifer storage and recovery (ASR) is a method to balance water supply with demand. It consists of injecting water in an aquifer during a period of excess, in order to keep it stored until there appears necessity (Pyne 2005). The stored water is then pumped back and distributed as drinking, industrial, or irrigation water. During ASR, water quality problems may arise when oxygenated water is injected into an anoxic environment where for instance pyrite, siderite, and sedimentary organic material (SOM) become oxidized (Stuyfzand 1998a, Appelo et al. 1999). Water quality may deteriorate further during an extended storage or recovery phase. Reactive transport modeling (RTM) of an ASR pilot gives further insight into the governing hydrogeochemical processes and their spatial and temporal behavior over time. RTM can thus be used as a predictive tool in order to perform risk assessment and to optimize ASR management.

Over the course of the last decade, there have been a few documented studies of simulated ASR applications with RTMs. Gaus et al. (2002) implemented a geochemical PHREEQC model capable of modeling dissolution of fluorite, the most likely process responsible for the increase in fluoride concentration in the recovered water of their pilot. The model was capable of simulating ASR cycles including radial flow and diffusive mixing as a consequence of dual porosity. Petkewich et al. (2004) developed a 3-D RTM with PHAST to simulate the evolution of water chemistry during ASR applications at Charleston, South Carolina. Simulations indicated calcite equilibrium and cation-exchange reactions were sufficient to explain hydrochemical changes during the course of the ASR pilots. Greskowiak et al. (2005) used PHT3D to model the reactive multicomponent transport at the Bolivar ASR site, South Australia. The major geochemical processes considered in the model were microbially mediated redox reactions, driven by the mineralization of dissolved organic carbon, mineral dissolution/precipitation (calcite and iron sulfides), and ion exchange. Brown and Misut (2010) performed scenario simulations for hypothetical well screens in Cretaceous aquifers in the New York city area, USA. They implemented a 3-D PHAST model testing the sensitivity of varied injectant and groundwater composition as well as the initial content of pyrite. All reactions were assumed to be at thermodynamic equilibrium. Their model was able to monitor the changes in pyrite and goethite content in time. Wallis et al. (2011) developed a reactive transport model on the fate of arsenic during ASR. They implemented a 3-D PHT3D model capable of simulating the release of arsenic during kinetically controlled oxidation of pyrite, surface complexation, and cation exchange reactions. Calcite, siderite, and hydrous ferric oxide were included in the model as equilibrium reactions. The aforementioned studies illustrate that ASR results in a diverse set of hydrogeochemical reactions with effects on different combination of solutes depending on the injection water and hydrogeochemical aquifer composition.

At the current ASR pilot site (Herten, the Netherlands), an observation based mass balance approach was used before to identify and quantify the chemical mass transfer from sediment

to water and vice versa (Chapter 2). The main hydrogeochemical reactions with the aquifer consisted of the oxidation of pyrite, SOM, and adsorbed Fe(II) and Mn(II) in all layers, and the dissolution of carbonates (calcite and Mn-siderite) mainly in the deepest aquifer layer. All reactions, except for the dissolution of siderite, showed a significant extinction over time, testifying of a general decrease in the aquifer's reduction capacity. Fe(II) and Mn(II) removal during recovery, pointing at sorption to neoformed ferrihydrite, was observed by particle tracking from the more distant observation well to the ASR well. Moreover, a decrease in mobilization of SO_4, Fe(II), and Mn(II) was observed during consecutive ASR cycles.

In the present subsequent study, the ASR pilot was simulated using a more comprehensive modeling approach, which consisted of a 1-D PHREEQC RTM, capable of simulating subsequent ASR cycles in a radial flow setting. The model consisted of kinetically simulated oxidation/dissolution reactions, cation exchange, and surface complexation. The model simulated pyrite and SOM oxidation, the simultaneous precipitation of Fe-hydroxides, and the dissolution of carbonates (siderite and calcite). Sorption of dissolved Fe(II) and Mn(II) on the Fe-hydroxide precipitates and the subsequent desorption later during recovery, were also part of the simulations. As opposed to a mass balance approach, the use of kinetic expressions for the simulation of oxidation and dissolution reactions enables the possibility to determine reaction parameters. These expressions with calibrated parameters can then subsequently be used for prediction purposes and scenario modeling.

The general objective of this study was the acquisition of a better understanding of the specific processes identified to be taking place in the Herten aquifer, as well as their quantification based on kinetic rate expressions. In contrast to the aforementioned ASR RTM studies, at this site SOM oxidation was important, whereas Mn acted as a restraining factor for ASR implementation. A specific objective was to assess the predictive capability of an ASR RTM. For this purpose, we followed a novel approach where the model calibrated with data from the first ASR cycle was allowed to run a series of 14 later cycles and its longer term performance was validated by comparing the model predictions to the actual observations of these later ASR cycles. In other words, we followed a realistic and practical approach that combines permissible calibration running times and reliable validation results. The model was subsequently used to study the temporal and spatial leaching of minerals around the ASR well. We demonstrate another capability of such a model in monitoring and predicting the aquifer's gradual "deactivation", a natural process promoted by subsequent ASR cycles. We finally inquired by means of scenario simulations on the possibility to enhance this "deactivation" and optimize the operation of the ASR plant regarding the recovered water quality by the addition of oxygen and/or sodium hydroxide to the injectant. In this line, we specifically focused on impeding the release of Mn(II) in the groundwater, a process that acted as a restraining factor for the feasibility of ASR applications in Herten.

3.2 MATERIAL AND METHODS

3.2.1 Description of ASR site and ASR cycles

The Herten ASR trial site consists of one ASR well that works both as an injection and recovery well, and two monitoring wells, M8 and M25, situated at 8 and 25 m distance, respectively (Figure 2.2). The system is placed in a deep and confined sandy aquifer consisting of 4 sublayers with different permeability and geochemical characteristics (section 3.2.5). In the aquifer prevails a small SE-NW regional hydraulic gradient of 0.00043 which, as concluded by the behavior of chloride during the various cycles (Chapter 2), did not cause any critical drifting of the injected bubble. The ASR well is screened along the entire aquifer depth (between 159.4 and 169 m depth), whereas the two observation wells contain three piezometers each with a 1 m long screen (Figure 2.2).

The experiment ran in the period of 2000-2009 and consisted of 2 pilots and 14 cycles (Figure 2.3b, Table 2.2). During the first pilot (October 2000 - May 2002), 5 ASR cycles were performed. Cycles 1, 2 and 5 were undertaken without a storage phase, while during cycle 3 no recovery was performed, and cycle 4 consisted of an injection phase only. During cycle 3, the injection water was enriched with oxygen (on average 0.78 mmol L^{-1}), and with nitrate (0.22 mmol $NaNO_3$ L^{-1}) during cycle 5, in order to study the effects of enhancing the oxidation processes. The second pilot (September 2007 - May 2009) started after a 5 years stand-still phase with the previously stored bubble still in place. Nine further ASR cycles were performed during the second pilot. The first four cycles lacked a storage phase, whereas the last five cycles consisted of long injection phases with shorter recoveries. During the various cycles there were meaningful variations in the injection/recovery rates (Table 2.2).

3.2.2 Conceptual model and modeling approach

The reactive transport model was developed with the PHREEQC (v. 2.17) code. Several modifications and additions were performed to the standard thermodynamic and kinetic database as described in section 3.2.3. The conceptualization consisted of simulating the evolution of geochemical reactions along two flow paths, in aquifer layers A and D, respectively. Such an approach was considered acceptable as the geochemistry of each layer was relatively homogeneous (Chapter 2) and the flow direction was primarily in longitudinal direction (due to proximity to the ASR well). Three-dimensional modeling is usually necessary whenever a background flow prevails in the system with direct impact on the operation of the well field. Radial 1-D modeling was considered valid as regional flow was negligible (0.045 m d^{-1}) and initial 3-D modeling showed the hydrochemistry of the layers did not influence each other (< 5% selecting a large vertical dispersivity of 0.1 m). This helped keeping running times within acceptable levels allowing sufficient calibration runs to be performed.

Layer C was not simulated because of its reactivity being comparable to layer A and the lower measurement frequency for screens M8-2 and M25-2. It was also unclear whether screen M25-3 was part of layer C or D (or both). Therefore, it was not used for the calibration process.

In order for the two flow lines to account for radial flow, cell lengths decreased with distance according to equations 3.1 and 3.2 (Appelo and Postma 2005):

$$length(1) = \frac{total\ length\ flow\ path}{\sqrt{n_{total}}} \tag{3.1}$$

where *length(1)* is the length of the first cell and n_{total} is total number of cells.

$$length(n) = length(1) \times \left(\sqrt{n} - \sqrt{(n-1)}\right) \tag{3.2}$$

where *length(n)* is the length of cell number n.

A large number of cells was selected to make the residence time in the model domain sufficiently long to enable simulation of recovery phases. In other words, the model domain should be large enough in order to avoid losing any fraction of the source water outside of the model boundaries and therefore making that fraction unrecoverable. Layer A and D were discretized into 700 and 200 cells, respectively, allowing a travel distance larger than the maximum front positions (Figure 2.3b). The number of shifts, for each injection, storage or recovery phase was the product of the cell number representing an observation well times the number of pore volumes that flushed the well, as calculated analytically in Chapter 2. Time steps, reflecting the residence time in each cell, were calculated by dividing the total time of each stress phase (injection, storage, or recovery) by the number of shifts. Longitudinal dispersivity was set to 0.1 m, assuring a good simulation of conservative solute transport, as verified by the chloride behavior during pilot 2 (Figure 3.3 and 3.4). The injected source water was assumed to fully displace the native groundwater. In reality, after the breakthrough of source water during cycle 1, native water was never again traced in any of the observation wells, indicating that the bubble grew over time.

3.2.3 Kinetically simulated processes

The following processes were assumed to be kinetically-limited: pyrite and sedimentary organic matter (SOM) oxidation, oxidation of dissolved ferrous iron, and dissolution/ precipitation of calcite and manganous-siderite. The rate expression used for pyrite oxidation was taken from Williamson and Rimstidt (1994). This expression has been successfully used in similar studies before (Appelo et al. 1998, Saaltink et al. 2003, Prommer and Stuyfzand 2005, Descourvieres et al. 2010):

$$r_{pyrite} = k_{pyr} m_{O_2}^{0.5} m_{H^+}^{-0.11} \left(\frac{A_{pyr}}{V}\right)\left(\frac{m}{m_0}\right)_{pyr}^{0.67} \left(1 - \Omega_{pyr}\right) \tag{3.3}$$

where k_{pyr} is a rate constant [mol dm^{-2} s^{-1}] with a value of $10^{-10.19}$ at 25°C, m_{O2} is the dissolved oxygen concentration [mol L^{-1}], m_{H+} is the proton concentration [mol L^{-1}], A_{pyr}/V is the ratio of initial pyrite surface area to solution volume [m^2 L^{-1}], m/m_0 is a factor that accounts for changes in surface area resulting from the progressing reaction, and Ω_{pyr} is the saturation ratio of pyrite (Prommer and Stuyfzand 2005).

The rate expression used for the oxidation of sedimentary organic matter (SOM) is a Monod type expression used by Van Cappellen and Gaillard (1996):

$$r_{SOM} = m_{SOM}\left(\frac{m}{m_0}\right)_{SOM}\left(r_{\max(O_2)}\frac{m_{O_2}}{k_{O_2}+m_{O_2}} + r_{\max(NO_3)}\frac{m_{NO_3}}{k_{NO_3}+m_{NO_3}} \times \frac{k_{O_2}^{in}}{k_{O_2}^{in}+m_{O_2}}\right) \tag{3.4}$$

where m_{SOM} and $m_{0,SOM}$ are the current and initial amount of SOM [mol L^{-1}], respectively, $r_{max(O2)}$ and $r_{max(NO3)}$ are maximal rate constants with values of 1.57 x 10^{-9} and 1.67 x 10^{-11} [s^{-1}], respectively, and k_{O2} and k_{NO3} are the half-saturation constants (Parkhurst and Appelo 1999). Their values are 2.94 x 10^{-4} and 1.55 x 10^{-4} [mol L^{-1}], respectively. The term $(m/m_0)_{SOM}$ was proposed in some models to account for the tendency of part of the sedimentary organic carbon to survive. Assuming such a term, the overall rate becomes second order (Parkhurst and Appelo 1999, User's Guide to PHREEQC, p. 42). The term $k_{O_2}^{in}/\left(k_{O_2}^{in}+m_{O_2}\right)$ was included in the rate expression in order to inhibit denitrification in the presence of oxygen. We assumed as an approximation that $k_{O_2}^{in} = k_{O_2}$, according to van Cappellen and Gaillard (1996). Oxidation of SOM coupled to sulfate- and iron-reduction was assumed to be irrelevant with respect to the short temporal scale of the ASR pilot and was therefore neglected. Oxidation of dissolved organic carbon (DOC) from the injection water was disregarded as concentrations were smaller than 0.08 mmol C L^{-1} and comparable concentrations were measured in the observation wells indicating that DOC degradation was negligible over this timescale.

Carbonate minerals pointing to a manganese-containing siderite were identified in small contents and especially in layers B and D (0.45% and 0.25% d.w., respectively). This mineral was considered as the main source of Mn^{2+} found in relatively high concentrations in the recovered water. In Chapter 2, the molar Fe:Mn ratio in the mineral was determined with a mass balance approach as 0.95:0.05. PHREEQC was instructed to simulate the dissolution of such manganous-siderite by defining the appropriate formula for the mineral ($Fe_{0.95}Mn_{0.05}CO_3$). The kinetic expression was taken by Descourvieres (2010):

$$r_{sid} = \left(k_1\left[H^+\right]^{0.65} + k_2\left[CO_2\right]^{0.65} + k_3\right)\left(\frac{A_{sid}}{V}\right)\left(\frac{m}{m_0}\right)_{sid}^{0.67}\left(1 - \Omega_{sid}\right) \tag{3.5}$$

where brackets indicate activities, k_1, k_2, k_3 are rate constants with values of 2.6 x 10^{-7}, 10^{-8} and 2.2 x 10^{-12} [mol cm^{-2} s^{-1}], respectively, A_{sid}/V is the ratio of initial siderite surface area to

solution volume [m^2 L^{-1}] and Ω_{sid} is the saturation ratio of the Mn-siderite. The solubility of the manganous-siderite was assumed to be equal to the one of siderite.

The small contents of calcite especially available in layer D were allowed to dissolve/ precipitate kinetically according to Plummer et al. (1978):

$$r_{cal} = \left(k_1\left[H^+\right] + k_2\left[CO_2\right] + k_3\left[H_2O\right]\right)\left(\frac{A_{cal}}{V}\right)\left(\frac{m}{m_0}\right)^{0.67}_{cal} \quad (3.6)$$

where k_1, k_2 and k_3 are temperature dependent constants [cm s^{-1}].

The oxidation of Fe^{2+} to Fe^{3+} was also simulated kinetically. This required a modification of the PHREEQC database in order to decouple the two valence states of iron and calculate the kinetic oxidation of Fe^{2+} to Fe^{3+} in water (Parkhurst and Appelo 1999). This way, the gradual decrease in Fe^{2+} concentration, observed during injection 1, was successfully simulated. The oxidation rate is given by Singer and Stumm (1970):

$$r_{Fe^{2+}} = -\left(k\left[OH^-\right]^2 P_{O_2}\right)m_{Fe^{2+}} \quad (3.7)$$

where P_{O2} is the partial pressure of oxygen [atm], $m_{Fe^{2+}}$ is the total molality of ferrous iron in solution [mol L^{-1}] and k is a rate constant with a value of 1.33 x 10^{12} [L^2 mol^{-2} atm^{-1} s^{-1}] at 25°C. This constant was allowed to adjust during calibration since, according to Stumm and Lee (1961), the rate increases about 10-fold for a 15°C temperature increase. Moreover, according to Davison and Seed (1983), the rate constant for the oxidation in natural freshwaters in the pH range 6.5–7.5 has a value of 3.33 x 10^{11} (with a range of 2.5–5 x 10^{11}). Dissolved ferric iron was simulated in thermodynamic equilibrium with ferrihydrite.

3.2.4 Processes in thermodynamic equilibrium

Cation exchange was simulated as an equilibrium process. The precipitation of Fe-hydroxides, a process that follows pyrite oxidation if oxygen is still available, was assumed to be fast and was therefore modeled as an equilibrium-based reaction. The precipitates form, on top of pyrite crystals, a surface which has high sorption capacity. The Dzombak and Morel (1990) database was used to simulate surface complexation of heavy metal ions on hydrous ferric oxide coupled to goethite. Small amounts of Mn-oxides were identified in layer D and were also included in the model as an equilibrium phase.

3.2.5 Model geochemistry and hydrochemistry

Average contents of minerals and SOM were based on geochemical analyses (given in % d.w.) performed by Buijs & van der Grift (2001) and used as initial contents in the model (Table 2.4). Initial contents of SOM and Fe-hydroxides showed large variations during the measurements and were further calibrated (Table 3.1). The conversion to moles per liter as required in PHREEQC was performed assuming a porosity of 0.3 and a bulk density of 1.855. For the specification of native and injected solutions we used average measured concentrations (Table 2.1). Inflow chemistry was kept fixed throughout each injection phase but was adjusted for every cycle taking into account of the small variations.

The native groundwater is characterized as pH-neutral, calcareous, deeply anoxic, oligohaline, unpolluted water of the $Ca(HCO_3)_2$-type. Ferrous iron concentration was rather high (0.1 mmol/L) and methane low (<2 µmol/L). Hydrochemical stratification in the aquifer was minimal, showing slightly higher Fe(II), Mn(II), Mg, and HCO_3 concentrations in the deeper parts, notably in layer D. The water was generally slightly undersaturated with respect to calcite (Saturation Index = -0.35) and oversaturated with respect to siderite (Saturation Index = +1.0). The model considered a homogenous distribution of the initial native water as measured in the observation wells before the initiation of the experiment.

Drinking water from the Herten pumping station was selected as the source water for the first pilot. This water was an aerated mixture of water pumped from aquifers shallower (50-110 m BGL) and deeper (190-220 m BGL) than the ASR target aquifer. For the second pilot, the source water was obtained from pumping station Heel (at 6 km distance) and showed some distinctive differences in chloride and sulfate concentrations compared to the previously used source water. Injected water quality was rather constant during each pilot, with chloride and sulfate fluctuations of ca. 15% and oxygen fluctuations of ca. 10%.

3.2.6 Automatic model calibration

The models for layer A and D were automatically calibrated using observations obtained during the first ASR cycle from monitoring wells M8-1, M8-3, and M25-1. The calibration was performed using the PEST package (Doherty 2005), following a procedure similar to earlier studies (Dai and Samper 2004, Van Breukelen et al. 2004, Karlsen et al. 2012). PEST optimizes the sum of weighted least squares between the model outputs and the field observations by changing assigned model parameters within given ranges of uncertainty. Calibration was performed in two steps. PEST was first instructed to calibrate the exchange coefficients for Ca, Mg, K, Fe (selectivity coefficients with respect to Na), whereas the coefficient of Mn was kept equal to the PHREEQC database. Then a second calibration round included the initial amount of Fe-hydroxides (equilibrium phase) and SOM in both layers, the reactive surface areas of pyrite, calcite, and siderite (A/V), and the rate constant for the kinetic oxidation of ferrous iron (k_{Fe2+}). The four selectivity coefficients were again allowed to change. Both models A and D were calibrated simultaneously to keep certain parameters (A/V, selectivity coefficients, k_{Fe2+}) equal. The two layers, being part of the same hydrogeological formation (Kiezelooliet formation) were not expected to show differences in the nature of their common minerals and exchangers. Initial contents of minerals (involved in kinetic reactions) and CEC were kept fixed to a mean value even though they showed some variation for each layer (Table 2.4). The reasoning behind this was to avoid calibrating more than one parameter related to the same rate expression and therefore to avoid high correlations between these parameters. The order of preference for the selection of the parameter allowed to calibrate for each process was: 1) reactive surface areas, 2) initial mineral contents, 3) rate constants.

Parameters were calibrated by means of breakthrough curves for Alkalinity, Ca, Mg, Na, K, O_2, pH, Fe(II) and Mn(II). The fluctuating SO_4 concentrations in the injectant, with a range of 0.1 mmol L^{-1} with respect to an average of 0.27 mmol L^{-1} together with the absence of sufficient information on its temporal variation, excluded sulfate from being a reliable process parameter for pyrite oxidation. The error associated with concentrations above 1 mg L^{-1} was treated as 95% confidence interval and weights were applied using the inverse of the standard deviation of this confidence interval (Dai and Samper 2004). For concentrations below 1 mg L^{-1}, an accuracy of 10% was expected. Weights of each observation (w_i) were thus calculated as

$$w_i = \frac{1.96}{\%error_i \times C_i} \tag{3.8}$$

where C_i is the concentration of observation i.

Table 3.1 Calibrated model parameters.

Parameter	Value	Units	Literature range		
$logK_{Na/Ca}$	0.83	-	0.29 – 2.44[a]		
$logK_{Na/Mg}$	0.57	-	0.16 – 1.62[a]		
$logK_{Na/K}$	0.76	-	0.15 – 2.60[a]		
$logK_{Na/Fe}$	0.59	-	0.44[b]. 0.5[c]		
$FeO(OH)_A$	0.12	mol L^{-1}			
$FeO(OH)_D$	0.09	mol L^{-1}			
SOM_A	0.86	mol L^{-1}			
SOM_D	2.09	mol L^{-1}			
A_{pyr}/V	0.44	$m^2 L^{-1}$	sand: 0.02 - 0.36	silt: 0.23 - 1.17	clay: 0.7 - 1.3 [d]
A_{cal}/V	2.98 x 10^{-4}	$m^2 L^{-1}$	sand: (0.4 - 1.8)x10^{-1}	silt: (1.1 - 7.7)x10^{-2}	clay: (3 - 4)x10^{-4} [d]
A_{sid}/V	2.9 x 10^{-4}	$m^2 L^{-1}$			
k_{Fe2+}	3.6 x 10^{11}	L^2 mol^{-2} atm^{-1} sec^{-1}	1.33 x 10^{12} at 25 °C [e]		
			2.5 x 10^{11} at 20.5 °C [f]		
			2.5 – 5 x 10^{11} [g]		

[a] from Karlsen et al. 2012
[b] from Parkhurts and Appelo 1999
[c] from Charlet and Tournassat 2005
[d] from Descourvieres et al. 2010
[e] from Singer and Stumm 1970
[f] from Stumm and Lee 1961
[g] from Davison and Seed 1983

3.3 RESULTS AND DISCUSSION

3.3.1 Calibration and validation results

Modeling results are presented for both flowlines A and D in Figure 3.1 and Figure 3.2, respectively. The cations are presented in the second row of graphs whereas the redox-sensitive elements are presented in the third row. Cycle 1 depicts calibration results while cycle 2 was run for short-term validation purposes. Generally, model results compare well with observed concentrations of the various elements. Chloride and sulfate observations showed a fluctuating behavior in contrast to the model output which assumed a stable input throughout the whole injection phase. In reality, variations up to 0.16 mmol L^{-1} were measured in both chloride and sulfate concentrations of the injectant during the same cycle. Nonetheless, the difference between sulfate observations in well M8-1 versus M25-1 and the associated modeled concentrations is similar, indicating that the extent of pyrite oxidation was well simulated.

The gradual oxygen breakthrough during the first injection was probably due to inhibition by labile organic material that derived from the drilling material and accumulated around the ASR well (Chapter 2). This process was not included in the model and O_2 was over predicted during the first days of injection (especially in layer D where travel times are higher). Increased initial concentrations of total inorganic carbon (TIC), especially in layer D, testified of this process, which gradually decreased during the following injections (Figure 3.2 and 3.6).

During injection the pH always increased due to the injectant having higher pH than the native water (Table 2.1). The acidifying effects caused by oxidation reactions during injection were observed during recovery, when water with lower pH crossed monitoring wells M8 (Figure 3.1 and 3.2). Well M25-1 did not show such behavior since the oxygen front never reached it during injections 1 and 2. The increasing acidity with distance observed in Figure 3.1 was responsible for an enhanced conversion of abundant HCO_3 into CO_2 leading to a decrease in bicarbonate with distance, in contrast to TIC which increased due to carbonate dissolution (results not shown). During injection, Fe(II) and Mn(II) in well M25-1 decreased more gradually as compared to M8-1 due to longer travel time and therefore less pore flushes with the infiltrate, delaying the equilibration with the exchanger (which required about 35 days for well M25-1). We therefore initially observe the combined effect of Fe(II) oxidation that derived both from the exchanger and from pyrite oxidation whereas after about 35 days we only observe the effect of Fe(II) oxidation that derived from pyrite. The decreasing mobilization in time is due to higher O_2 availability for the pyrite-deriving Fe(II) after all cation exchange-deriving Fe(II) is oxidized. During recovery, Fe(II) and Mn(II) concentrations increased due to pyrite and Mn-siderite dissolution, as well as desorption from Fe-hydroxides in response to competition with protons from the incoming acidic water.

After obtaining satisfactory predictions for cycle 2, the model was allowed to run for all 14 cycles in order to evaluate its longer term performance. From cycle 6 onwards, the injected solution was switched to Heel water composition. The model's predictive capacity for layers A and D is presented in Figure 3.3 and Figure 3.4, respectively. The general model fit was satisfactory for both layers. The sulfate input during pilot 2 was more stable and therefore SO_4 concentrations could be used as a confirmation that pyrite oxidation was properly simulated. Na, K, Ca, and Mg were simulated well throughout all cycles as well as the long-term gradual decline in Fe(II) and partly Mn(II). This decline resulted from increasing sorption to Fe-hydroxides (Figure 3.5) connected to the gradual build-up of Fe-

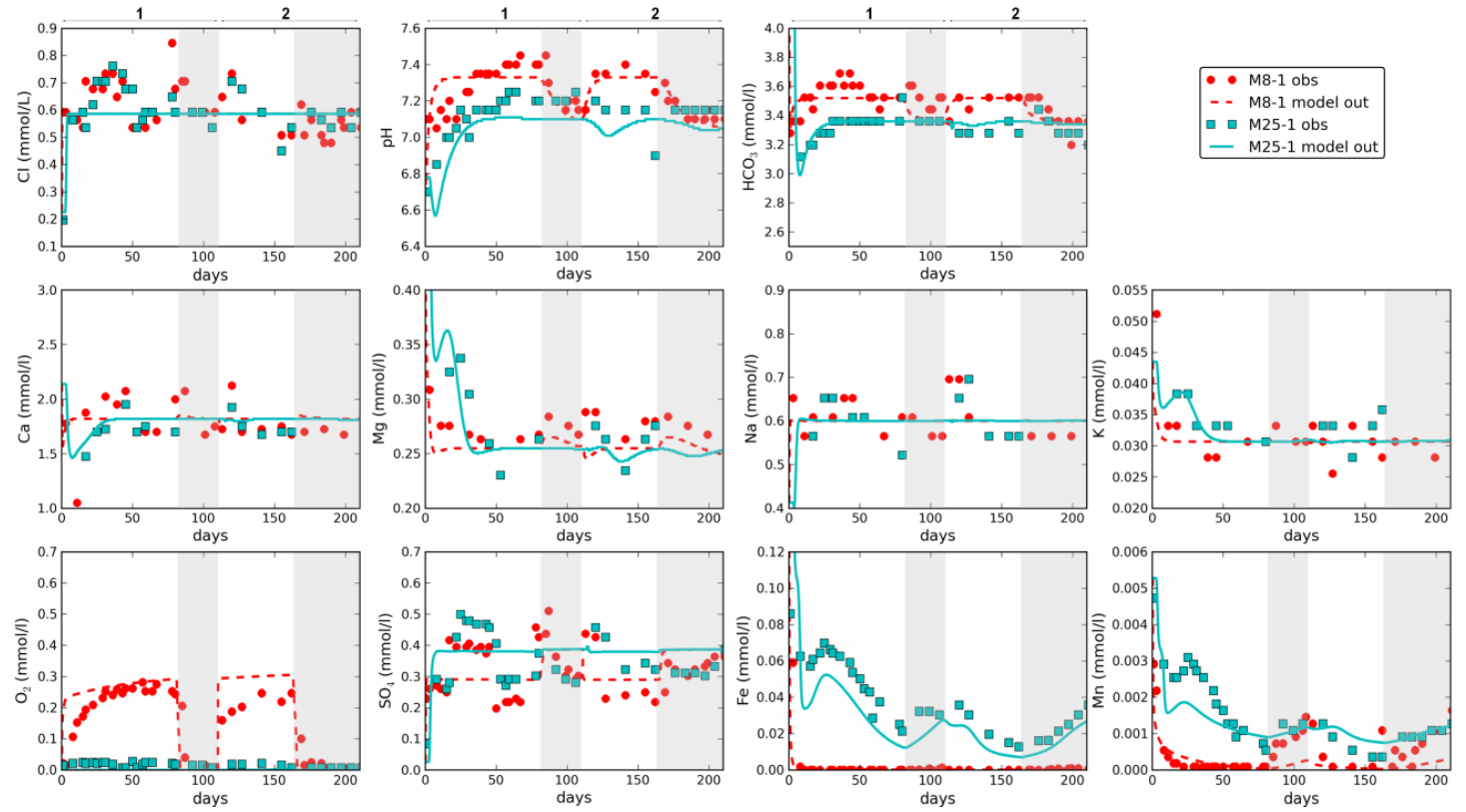

Figure 3.1 Layer A - Observations and model output for various elements during cycle 1 and 2 (white = injection, grey = recovery).

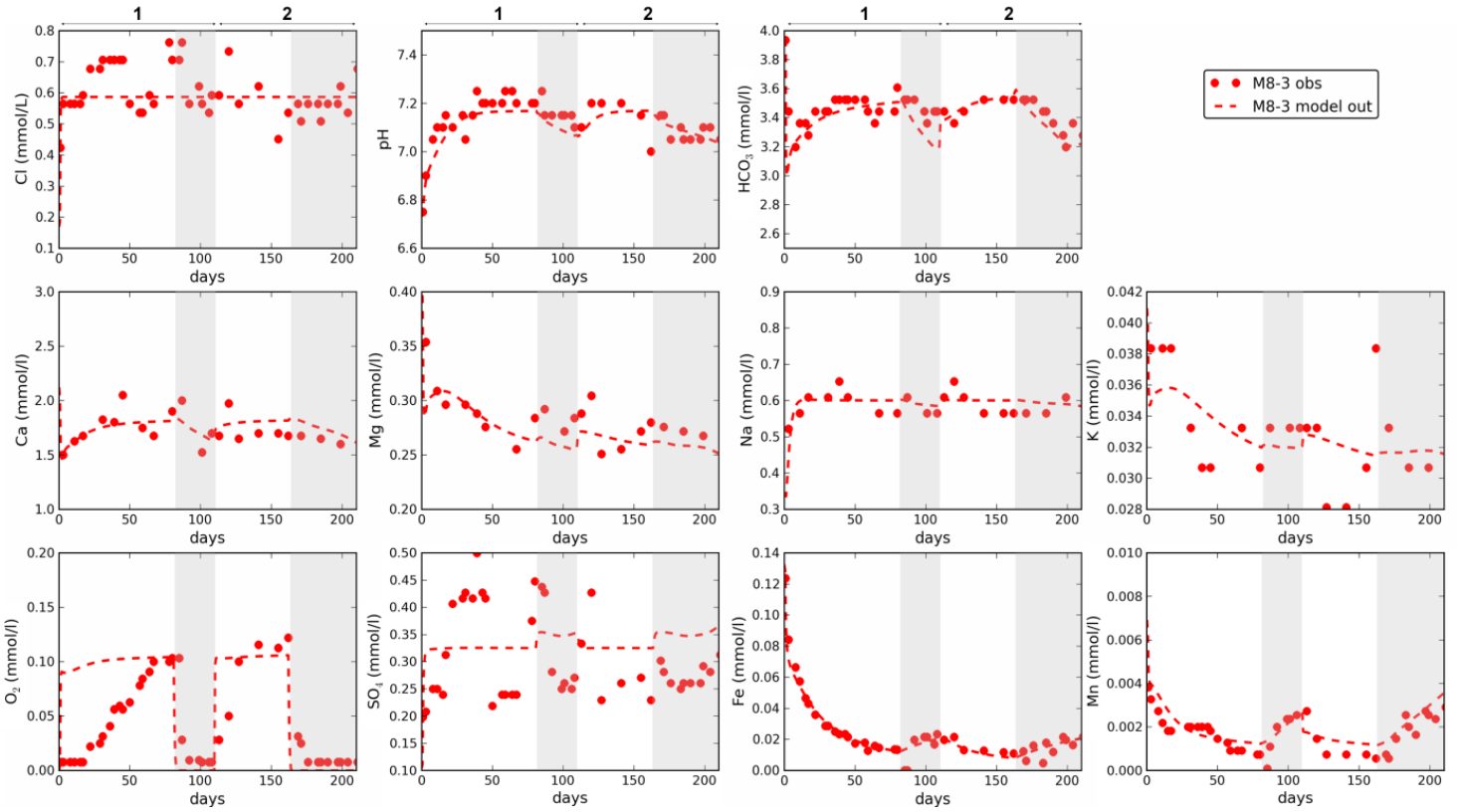

Figure 3.2 Layer D - Observations and model output for various elements during cycle 1 and 2 (white = injection, grey = recovery).

hydroxide precipitates with subsequent cycles. From cycle 10 onwards we observed some deviations in pH predictions (up to 0.4 units overestimation) at well M8-1 during storage and subsequent recovery phases. Such discrepancies might be related to the fact that, as opposed to what the model predicts, the small amounts of calcite remaining in layer A do not dissolve sufficiently to buffer the acidity produced from the O_2 consumption during storage.

According to the modeled output, during the first 7 days of injection, Fe(II) gets initially sorbed on Fe-hydroxides (Figure 3.5). Once the oxygen front reaches M8-3 (after 3.5 days), desorbing ferrous iron gets oxidized to ferric iron and precipitates again as Fe-hydroxide (sorption to Fe-hydroxides remains the dominant process until day 7). During recovery, incoming Fe(II) initially sorbs on these newly formed Fe-hydroxides, until the pH drops below a threshold (~7) and Fe(II) desorbs in response to competition with protons. From cycle 10 onwards, longer injection phases were applied, as compared to recoveries, shifting these processes further away from well M8-3. During recoveries, the pH does not drop below the threshold and Fe(II) does not desorb anymore. Moreover, Figure 3.5 shows how, during injection, cations from the injection water exchange with Fe(II) from the exchange sites (Appelo et al. 1999). During recovery, the exchange complex gets reloaded with Fe(II) deriving from pyrite and Mn-siderite dissolution.

Cycle 3 was studied separately in order to determine the ability of the model to simulate increased oxidation reactions and related processes triggered by an oxygen-enriched injectant (Figure 3.6). Initial simulations using the previously derived oxidation rates resulted in sudden oxygen consumption (within 3 days) once injection stopped (results not shown). As a consequence, sulfate increased rapidly and did not agree with the observed gradual increase, implying that pyrite oxidized more slowly. Oxygen observations during storage show a rather odd behavior (0.04 mmol/L at day 53 and 0.08 mmol/L at day 64) posing concerns about the reliability of the measurements/analyses. Nevertheless, these low concentrations indicated that oxygen consumption during storage was slower. Following a fitting trial and error procedure, O_2, SO_4 and partly pH predictions during storage improved significantly by reducing pyrite and SOM oxidation rates during storage by a factor of 2 and 2.8, respectively (Figure 3.6). A rate limitation was to be expected as the groundwater flow velocity dropped to zero. The produced acidity from oxidation reactions was buffered by the dissolution of carbonates (Mn-siderite and calcite) leading to an increase in Ca, Mg, TIC, Fe(II), and Mn(II) concentrations. The modeled pH decreased until oxygen was completely depleted. Subsequently, pH increased due to the afore mentioned carbonate dissolution reactions. The modeled pH shows some clear discrepancies with the observed pH, which shows a decreasing behavior throughout the whole storage phase. This is a hard to explain phenomenon which, in conjunction with a small decrease in Fe later in the storage phase, could indicate re-precipitation of iron containing carbonate (SI approaching 0). Decreasing pH during storage at well M8-1 was also observed during cycle 12, 13, and 14 but there are no Fe observations to allow comparison with cycle 3.

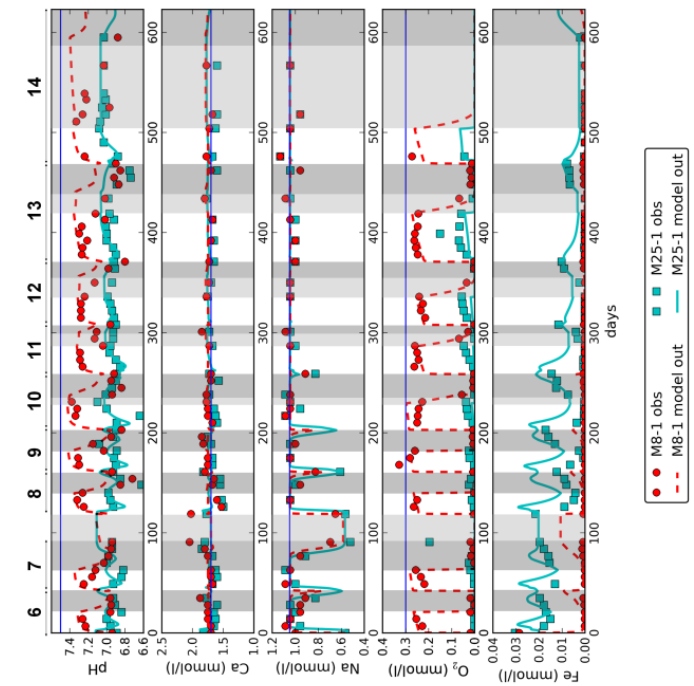

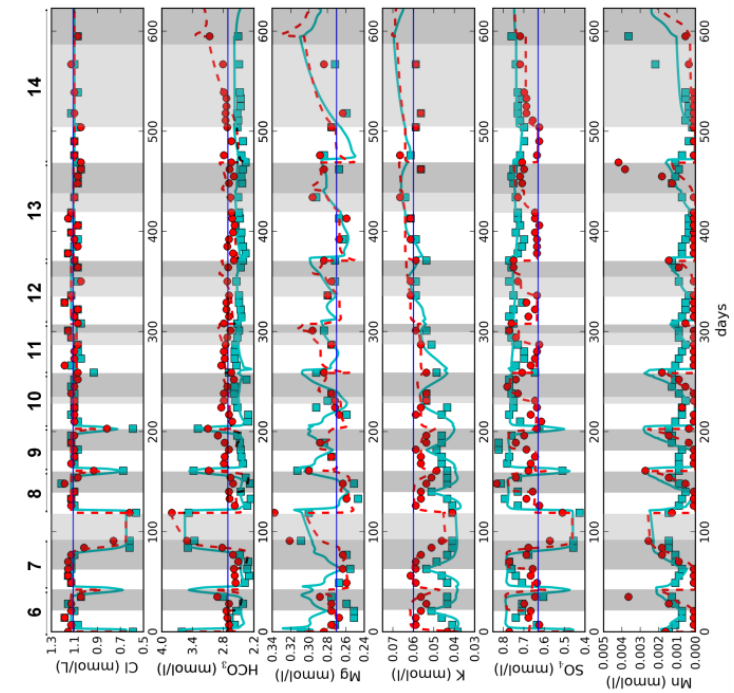

Figure 3.3 Layer A - Observations and model output for various elements during cycles 6 – 14 (white = injection, light grey = storage, dark grey = recovery). Blue line indicates average input concentration during injection phases

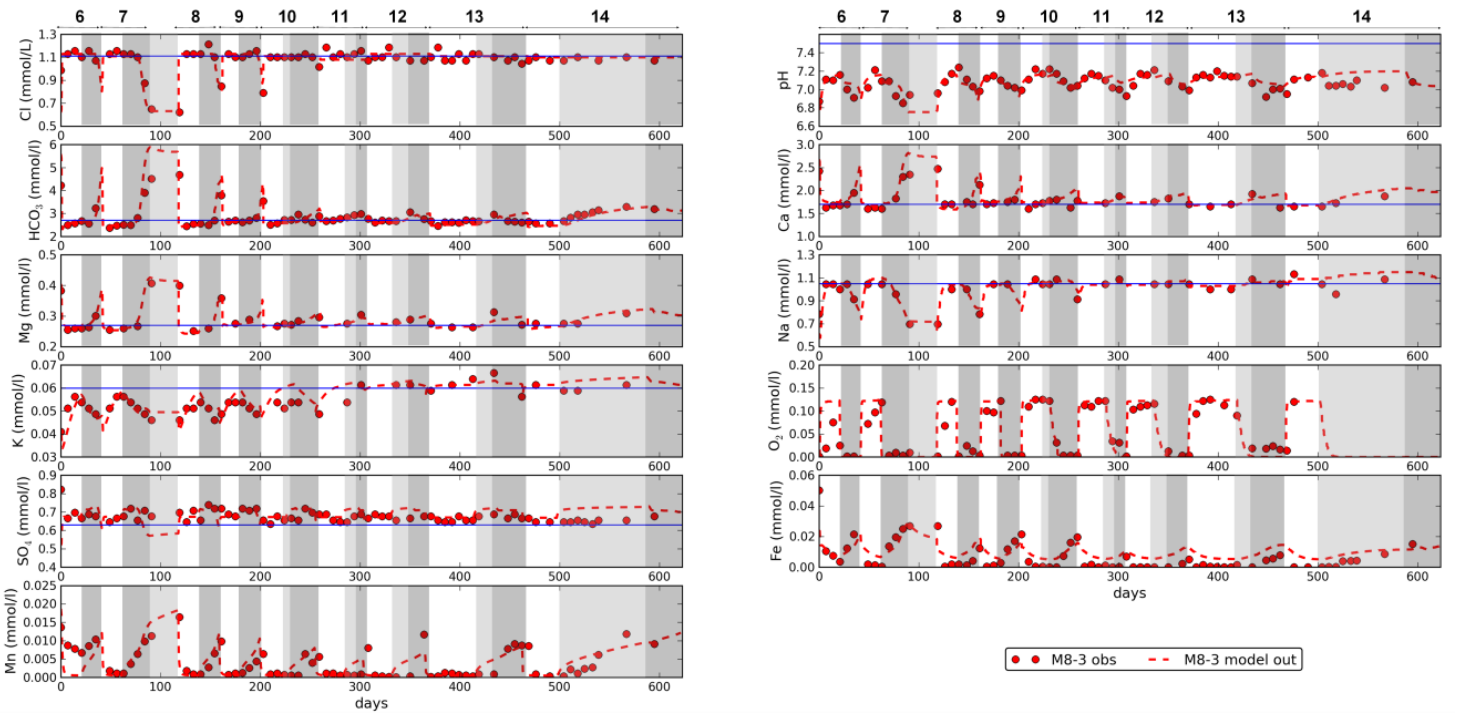

Figure 3.4 Layer D - Observations and model output for various elements during cycles 6 – 14 (white = injection, light grey = storage, dark grey = recovery). Blue line indicates average input concentration during injection phases

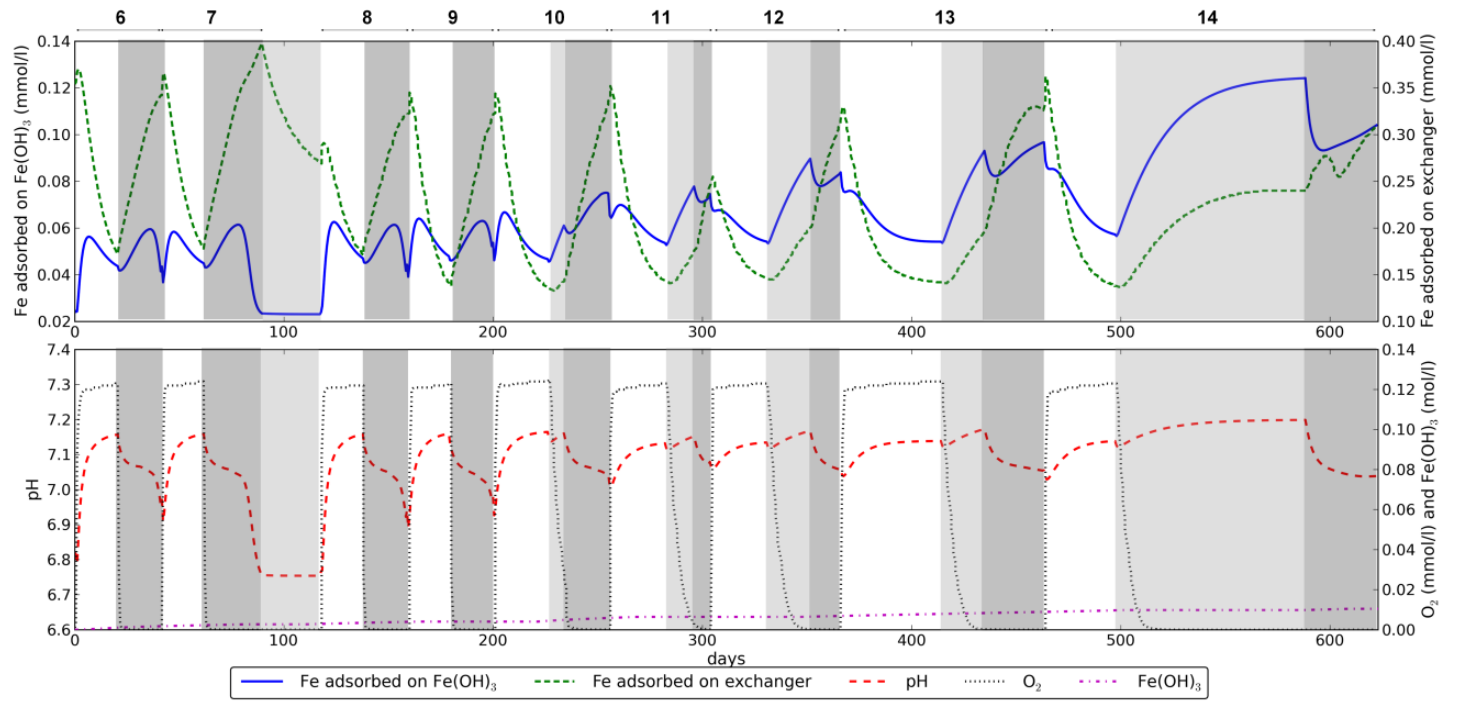

Figure 3.5 Simulated adsorbed concentrations of Fe on Fe-hydroxide precipitates (primary y axis) and on the exchanger (secondary y axis) in well M8-3 (white = injection, light grey = storage, dark grey = recovery).

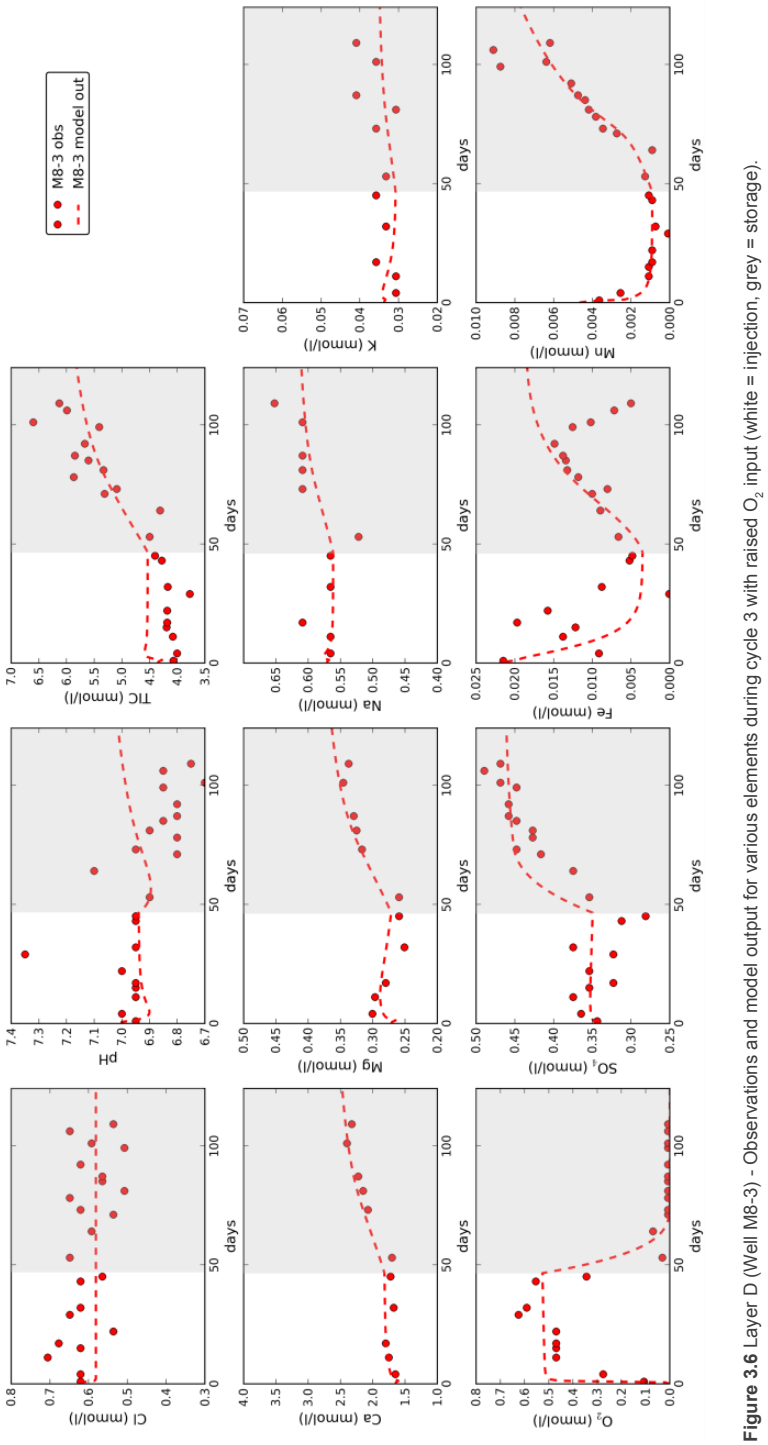

Figure 3.6 Layer D (Well M8-3) - Observations and model output for various elements during cycle 3 with raised O_2 input (white = injection, grey = storage).

Decreased oxidation rates in well M8-3 during storage were also obtained from the mass balance calculations (Chapter 2). Even though a clear decrease was not proved for cycle 3, it was proved for cycles 13 and 14. Slower denitrification during storage has been demonstrated before (Stuyfzand et al. 2002) and was explained by the prevailing stagnant conditions which limit the contact of oxidant with the reactive crystals.

3.3.2 Modeled oxidation and dissolution rates

In order to make reductant oxidation rates comparable and to assess the proportions of the different reductants to oxygen consumption, the modeled oxidation rates were multiplied with the electron transfers required for each reaction. The oxidation of pyrite releases 14 electrons (7 from each sulfur atom in the mineral) per unit of pyrite, whereas the oxidation of SOM releases 4 electrons. Ferrous iron releases one electron when it oxidizes to Fe(III). Oxidation/dissolution rates as well as the relative proportions during injection 1 (as percentage over time) are presented in Figure 3.7 for layer A and D.

Initial mineral content, travel time, pH, and oxygen concentration are the main parameters that influence the magnitude of oxidation/dissolution rates. A strong spatial difference in modeled oxidation rates was observed between wells M8-1 and M25-1 in layer A (Figure 3.7). Since a homogeneous initial mineral content was assumed for each layer, the higher rates in M8-1 were attributed to shorter travel times and therefore higher receiving oxygen concentrations.

During injection 1, pyrite shows the highest relative contribution of ~ 56% at well M8-1 rising to ~ 74% at downgradient well M25-1. The second most important reductant, SOM, has a contribution of ~ 41% at well M8-1 but decreases to ~ 24% at well M25-1. This increasing relative contribution of pyrite with distance, as opposed to SOM, is related to the gradients in oxygen and pH, which enhance pyrite over SOM oxidation (see kinetic expressions in section 3.2.3). Oxidation of ferrous iron is least important and, apart from a substantial starting proportion related to oxidation of sorbed Fe(II) during the preceding recovery phase (if any) and of desorbing Fe(II) due to cation exchange (~12% and ~ 7% at wells M8-1 and M25-1, respectively), it decreases over time to ~ 3% at both wells, deriving entirely from pyrite. At well M8-3, pyrite and SOM show relative contributions of ~ 56% and ~ 37%, respectively. Ferrous iron oxidation showed a maximum contribution of ~ 11% during the initial oxygen breakthrough followed by a later decrease to 4%. The different reactivities observed between wells M8-1 and M8-3 come in good accordance with mineral contents in layers A and D (Table 2.4 and 3.1).

Siderite dissolution contributed indirectly to overall oxygen consumption only for layer D albeit being of little significance. Mn-siderite dissolution leads to release of Fe(II) to the groundwater which oxidizes to Fe(III) in the presence of oxygen. The maximum proportion of this reductant to overall oxygen consumption was calculated as only 1.5%. The contribution of Mn(II) oxidation did not exceed 0.2% and was considered negligible.

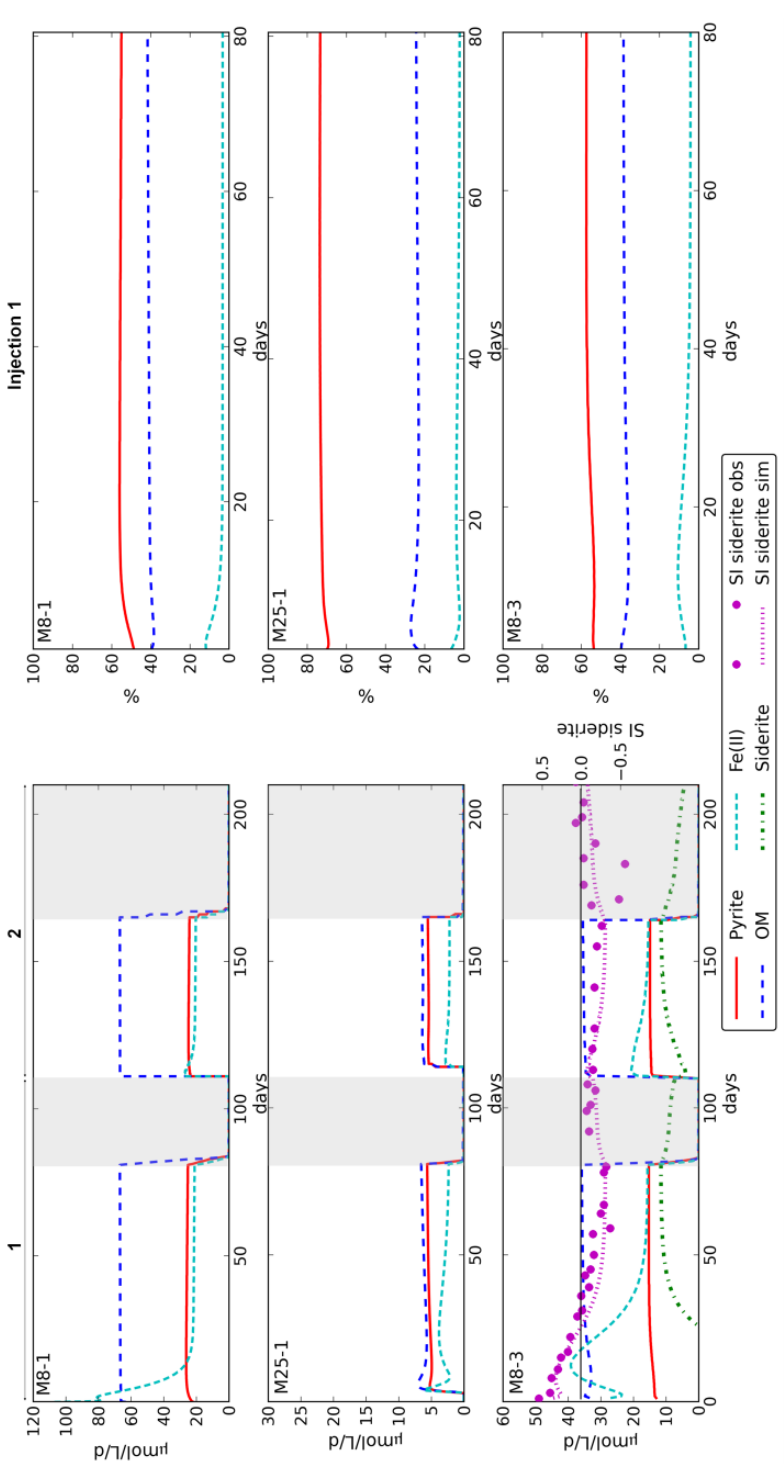

Figure 3.7 Well M8-1 (above), M25-1 (middle), and M8-3 (below). Oxidation/dissolution rates during cycle 1 and 2 (left) and proportions of oxygen consumption by the different reductants (right) based on electron transfers during injection 1 (% µmol e⁻ L⁻¹ day⁻¹). $SI_{siderite}$ is plotted on the secondary axis. White and grey shaded areas indicate injection and recovery periods, respectively.

For both layers, the saturation index of pyrite remained negative indicating the tendency of pyrite to oxidize. The modeled dissolution of Mn-siderite and its saturation index over time is also presented in Figure 3.7. During injection 1, Mn-siderite started dissolving after 27 days when the saturation index dropped below 0, due to the infiltration water being undersaturated with regards to siderite, while dissolution occurred over the complete duration of injection 2. This delayed start of siderite dissolution was caused by an increased desorption of Fe(II) due to cation exchange, keeping the saturation index positive. Dissolution of Mn-siderite continued during recovery phases but at reduced rate.

The variation in modeled oxidation and dissolution rates during subsequent injection cycles is depicted in Figure 3.8. The injection rate of the ASR well influences the magnitude of oxidation and dissolution rates. Higher injection rates translate to higher oxygen availability and therefore higher oxidation capacity especially further downgradient. This is clearly depicted by elevated oxidation rates of all reductants during injection 5 (59 m^3/h) and during injections 6-10 (50 m^3/h) as compared to injections 11-14 (40 m^3/h) and injections 1-2 (45 m^3/h), particularly for wells M25-1 and M8-3 (Figure 3.8, Table 2.2). The modeled oxidation rates of pyrite and SOM, during injection 3 (O_2 enriched), increased by a factor of 1.5 and 1.45 at well M8-1, 3.4 and 8.1 at well M25-1, and 1.9 and 2.3 at well M8-3, respectively. This behavior indicates that the longer the travel time (and provided oxygen is not yet depleted), the higher the relative increases in oxidation rates become as consequence of a higher relative increase in oxygen breaking through. During injection 3, the relative contributions of the different reductants to oxygen consumption remained similar to injection 1. The maximum dissolution rate of siderite, measured at the end of injection 1 and injection 3, respectively, increased by a factor of 1.6.

A comparison was made between the modeled oxidation/dissolution rates and the ones obtained from the mass balance calculations in Chapter 2 (Table 3.2). The rates deduced by the mass transfers showed more variation between ASR cycles because their calculation included measured concentration variations in the observation wells, analytical noise and fluctuations in input quality. Averaging the rates for all 14 cycles revealed that the rates obtained by the mass balance approach were generally higher. The mass balance rates were presented 14-21 days after the start of each injection in order to exclude initial effects such as oxidation of desorbing Fe(II). This resulted in less competition for pyrite and SOM oxidation and therefore higher calculated rates.

The depyritization front was simulated during the various cycles, assuming a homogeneous initial content for each layer (Figure 3.9). Over time the content of pyrite decreased, whereas the content of neoformed Fe-hydroxide increased as result. A lower permeability, as in layer D, increases the spatial gradient of the pyrite oxidation rate and its remaining content. Complete pyrite depletion did not occur yet in any of the monitoring wells. The overestimated oxidation rate of pyrite in Chapter 2 was translated into a more advanced leaching progress (almost complete pyrite depletion in well M8-1) which is now not the case.

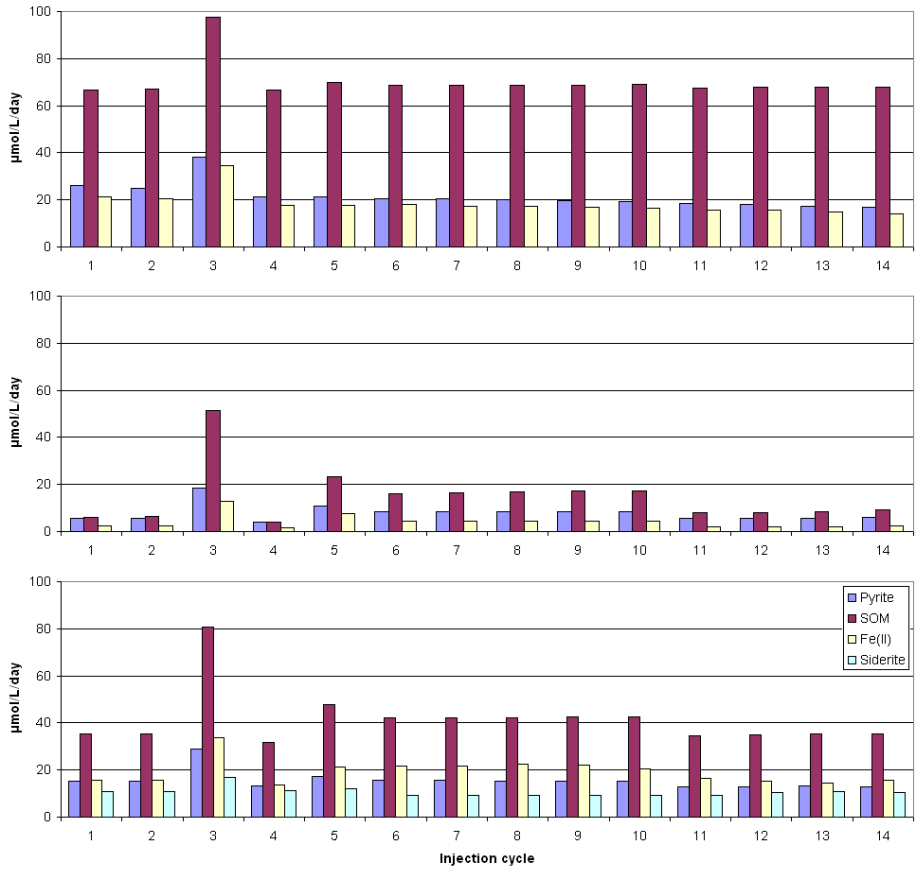

Figure 3.8 Oxidation rates in monitoring well M8-1 (above), M25-1 (middle) and M8-3 (below), during all injection cycles.

Table 3.2 Mean oxidation/dissolution rates for all 14 ASR cycles as deduced by the mass balance calculations (Antoniou et al.) and by the reactive transport model. Rates in µmol/L/day.

	M8-1		M25-1		M8-3		
	Pyrite	SOM	Pyrite	SOM	Pyrite	SOM	Siderite
Mass balances	33	80	16	13	18	53	27
Model	22	70	8	15	16	42	11

Nevertheless, a major net decrease occurred in layer A and especially during pilot 1, due to longer injection phases and enriched oxidant concentrations. The increased oxidation, due to O_2 enrichment of the source water, taking place during injection 3, despite its shorter duration, is clearly depicted by the larger downward shift of its content, especially further away from the ASR well. The modeled precipitation of neoformed Fe-hydroxides in layer D

was limited to the proximity of the ASR well due to lower permeability. The increased pyrite oxidation during injection 3 caused a more extended Fe-hydroxide precipitation, especially in layer A.

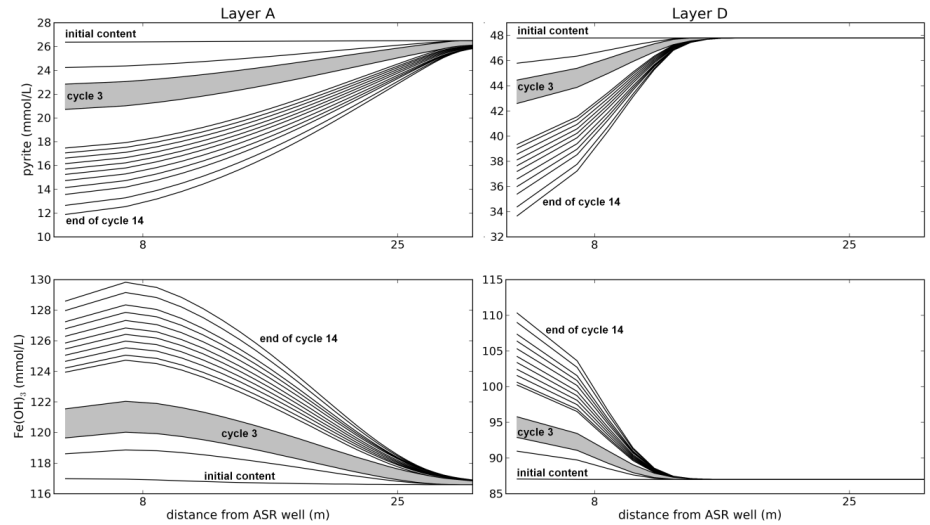

Figure 3.9 Pyrite content (above) and neo-formed Fe-hydroxide precipitates (below) versus distance at the end of each cycle. The positions of monitoring wells M8 and M25 are marked on the X axis.

3.3.3 Model uncertainty

A reasonable overall match was obtained using the set of calibrated parameters, as obtained by PEST. A further step was to study the parameter sensitivities with respect to all observations. We examined the effect of each calibrated parameter on modeled results and summarized the effects of the most sensitive parameters in Figure 3.10. For each analyzed parameter, a highest and a lowest relevant value were used and the effect of each value on model results was evaluated. The lowest and highest values for selectivity coefficients and reactive mineral surfaces were chosen based on the literature (Table 3.1). Initial SOM and Fe-hydroxide contents were varied based on the minimum and maximum measured values.

Modeled O_2 concentration is, as expected, highly sensitive to the pyrite reactive surface area and initial SOM content. Mn(II) shows high sensitivity to SOM content, especially during recovery, as well as to $\log K_{Na/Ca}$ during both injection and recovery. The pronounced Mn(II) increase during recovery is related to the complete absence of O_2 and more acidic conditions in the beginning of recovery, allowing for a more pronounced Mn-siderite dissolution. Fe(II) on the other hand is mostly influenced during injection when altering the initial Fe-hydroxide content and the $\log K_{Na/Ca}$. Higher $\log K_{Na/Ca}$ values give larger dominance of Ca on the CEC and lower proportions of other cations including Fe and Mn; therefore,

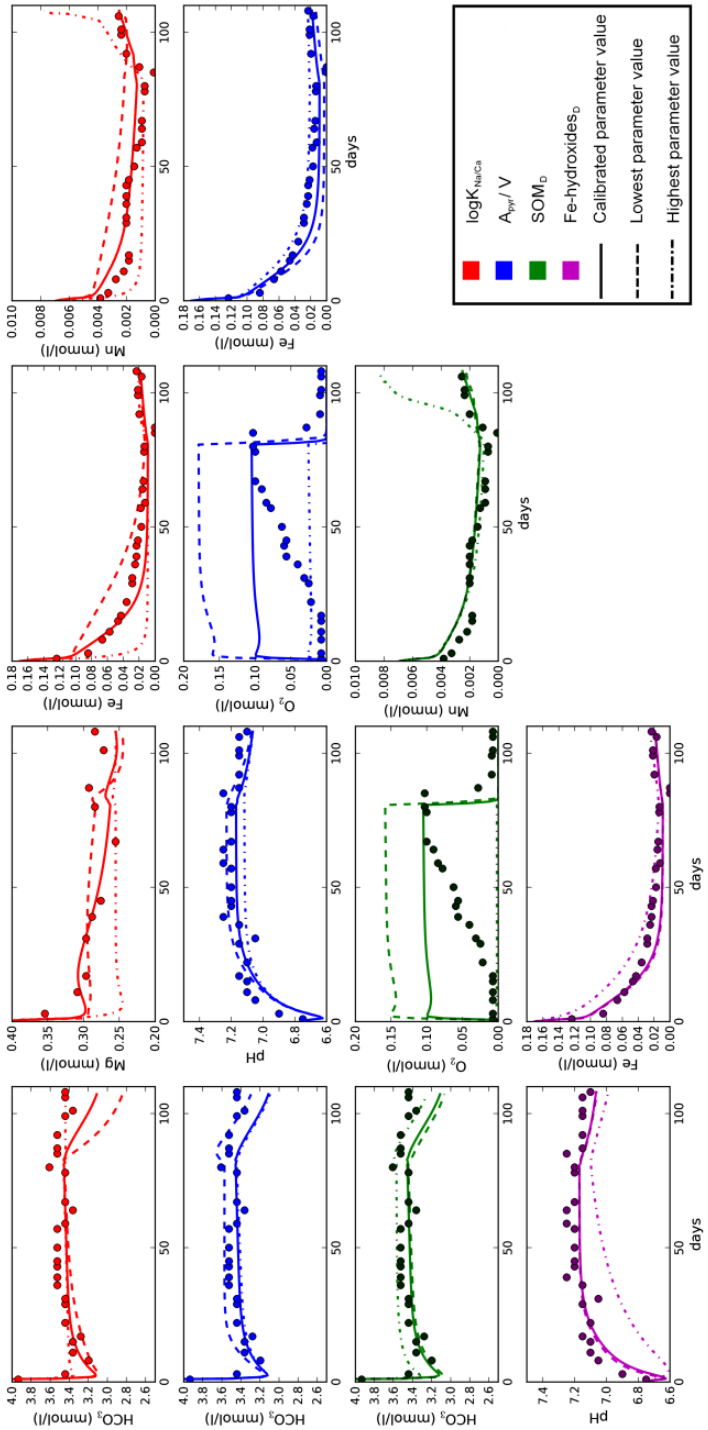

Figure 3.10 Sensitivity analysis results depicting the amount of influence of each calibrated parameter to the various observation groups.

with higher logKNa/Ca, less Fe and Mn are available for oxidation resulting in a quicker decline in Fe(II) and Mn(II). A higher initial amount of Fe-hydroxides translates to more sorption sites for dissolved Fe(II) and Mn(II) that subsequently get oxidized when the O_2 front arrives, causing the pH to drop. Bicarbonate shows some sensitivity to all calibrated parameters.

3.3.4 Scenario modeling

During ASR practice, the injectant can be enriched with oxidizing and/or pH-buffering agents. This is useful for: 1) coating the reactive minerals (pyrite) with Fe-hydroxides, 2) keeping the aquifer (sub)oxic for longer periods, and 3) buffering the acidity produced by oxidation reactions. Furthermore, all of these may prevent the mobilization of Fe(II), Mn(II), and for some cases arsenic (Stuyfzand et al. 2005b). Oxygen and nitrate can both be used as oxidizing agents but, from an esthetic point of view, the first is strongly preferred. As pH-buffering agents, sodium hydroxide and particularly sodium carbonate are usually preferred (Ibison et al. 1995).

Cycle 3 was used for scenario simulations in order to evaluate the effects of enriching the injectant with different agents. Four scenarios were simulated using normal injectant as in cycle 1 and 2 (scenario 1), adding sodium hydroxide (scenario 2), adding additional oxygen (scenario 3), and finally, adding both agents together (scenario 4).

As described earlier, scenario 3 represents the actual injectant composition used during cycle 3, which lead to increased oxidation reactions and dissolution of carbonates. A general concentration increase for all depicted cations was observed (Figure 3.11). Even though the pyrite oxidation rate increased, also siderite dissolved faster, releasing Fe(II) and Mn(II) in the water. A simple base addition (e.g., NaOH or Na_2CO_3), simulated as scenario 2, would prevent the pH to drop to low levels and as result prevent strong dissolution of carbonate minerals during storage (after the complete consumption of oxidants). This option would result in low amount of dissolution of Fe(II) and Mn(II) in the groundwater. If the purpose is to accelerate the aquifer's leaching from its reactive species and form an extended, and therefore more efficient, zone of Fe-hydroxide precipitates then oxygen enrichment should be combined with a pH-buffering agent (scenario 4). The amount of agent to be added depends on the levels of dissolved Fe(II) and Mn(II) that are desired and could be optimized by using the model presented.

There are possible side effects related to the addition of pH-buffering agents and these should be carefully taken into account. Injection of sodium hydroxide increases the concentration of dissolved sodium and this ion should not exceed the drinking water limit of 3.75 mmol L^{-1}. The saturation index for calcite will also increase (Figure 3.11) and precipitation of carbonate minerals may be induced. If this happens close to the ASR well, clogging problems may arise. Therefore, special attention should be paid regarding the amounts of base injected and the related risk for aquifer clogging due to calcite crystallization.

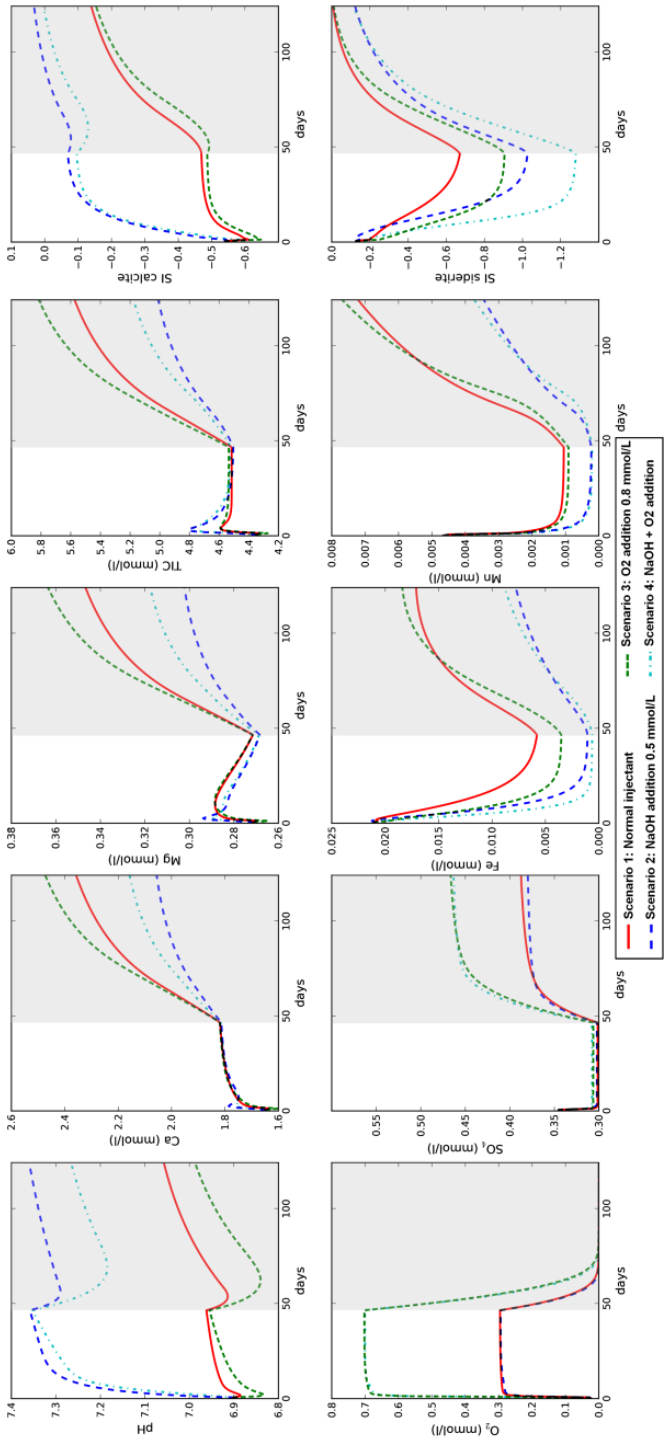

Figure 3.11 Model output for various elements for 4 different scenarios during cycle 3 at well M8-3 (white = injection, grey = storage).

3.4 CONCLUSIONS

In the present study, the main hydrogeochemical reactions taking place in two aquifer layers during an ASR pilot were simulated using a 1-D radial RTM. During every injection phase, aerobic water was injected causing oxidation reactions with the main aquifer reductants, namely pyrite, SOM, and to lesser extent Fe(II). The resulting acidification caused dissolution of carbonate minerals (calcite and Mn-siderite) as testified by the increasing TIC during storage phases. These dissolution reactions as well as desorption from Fe-hydroxides released Fe(II) and Mn(II) in the water during recovery phases. The model calibrated for cycle 1 was allowed to run for all 14 ASR cycles in order to evaluate its longer term performance. Such an approach offered a good combination between tolerable calibration running times and reliable validation results. A sensitivity analysis was then performed to evaluate the effect of model parameter variation on model predictions. Despite the change in injected solution composition from cycle 6 onwards, the general model fit for the 11 investigated parameters was satisfactory. The simulated pyrite oxidation agreed with the sulfate observations, whereas Na, K, Ca, and Mg concentrations indicated that cation exchange was simulated well. The model suggested an increasing sorption capacity due to a gradual build-up of Fe-hydroxide precipitates resulting by prolonged injection phases. Modeled Fe(II) suggested a long term subsurface removal, while Mn(II) showed a tendency to easily desorb.

Oxidation and dissolution rates at three aquifer locations (monitoring wells) were calculated for all injection cycles and compared to each other. It was concluded that initial mineral content, travel time, and injection rate play a key role in the magnitude of oxidation and dissolution rates. Shorter travel time and higher injection rate translate to higher available oxygen concentrations at a given aquifer location implying higher oxidation rates. Pyrite was ranked as the most important reductant, followed by SOM and then Fe(II). Moreover, the pH and oxygen gradients with distance were found to enhance the rate of pyrite over SOM oxidation. The relative increase in oxidation and dissolution reactions at a given aquifer location due to oxygen enrichment was found to be proportional to the travel time meaning that more distant locations showed a higher relative increase. The oxygen and sulfate observations during storage supported the idea that oxidation rates drop during stand still as a consequence of the prevailing stagnant conditions.

The model was used to monitor the “deactivation” of the aquifer from its main reductants, a natural process promoted by subsequent ASR cycles. For this purpose, the pyrite leaching fronts and the Fe-hydroxide precipitation fronts as simulated were monitored in the two aquifer layers during 14 ASR cycles. A higher permeability caused more extended pyrite depletion. Oxygen enrichment performed during cycle 3 increased the depyritization extent in both layers. It also caused a more extended Fe-hydroxide precipitation, enhancing the overall sorption capacity in the aquifer for Fe(II) and partly for Mn(II). The model proved that oxygen enrichment and higher injection rates can accelerate the aquifer’s leaching

from its reactive species. However, this measure will also cause increased carbonate dissolution increasing the dissolved Fe(II) and Mn(II) concentrations in the aquifer. Scenario simulations showed that, if oxygen enrichment is combined with pH-buffering agents (e.g. NaOH or Na_2CO_3), dissolution of Fe(II) and Mn(II) can be controlled without impeding an accelerated aquifer leaching.

CHAPTER 4

Optimizing aquifer storage and recovery performance through reactive transport modeling

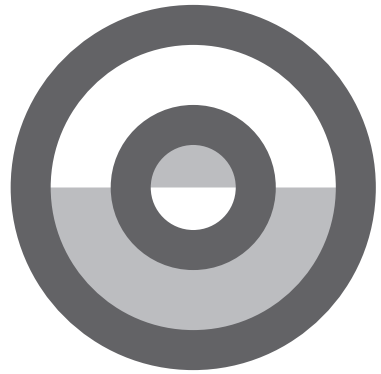

Article in press:

Antoniou, E. A., Van Breukelen, B. M. and Stuyfzand, P. J. Optimizing aquifer storage and recovery performance through reactive transport modeling. Applied Geochemistry

ABSTRACT

Water quality deterioration is a common phenomenon that may limit the recovery of injected water during aquifer storage and recovery (ASR). Quality deterioration is often caused by the oxidation of reduced aquifer components by oxygenated source water, the subsequent pH decline, and induced dissolution of carbonate minerals. We use a previously calibrated reactive transport model (PHREEQC) to optimize ASR depending on source water quality and kind of pretreatment. We give quantitative projections on the performance increase over successive cycles with respect to specific water quality indicators. We simulate the response of a representative, deeply anoxic aquifer upon injection of three different commonly applied oxygenated water types: pre-treated drinking water, desalinated seawater, and urban storm water. The model is coupled to a Python script that automatically stops recovery and starts the next injection phase when certain specified concentration thresholds are exceeded. This setup enables realistic simulations to gradually create a buffer zone around the ASR well that allows 100% recovery at a specific stage of aquifer development. Each source water type was associated with different issues causing the deterioration of the abstracted water quality with respect to Fe(II), Mn(II), and As. The injection of pre-treated drinking water caused Mn(II) exceedances that disappeared after a number of cycles, provided that the recovery would halt as soon as the Mn(II) exceedances would occur. The injection of desalinated water caused persisting Fe(II) exceedances, which substantially slowed the creation of an effective buffer zone; whereas, the injection of urban storm water caused similar issues with respect to arsenic. For both cases, it was shown that enriching the source water with O_2 and/or NaOH had major positive effects by accelerating the creation of an efficient buffer zone. Finally, we simulated a long-term operational rest of the ASR plant to evaluate water quality effects during potential migration of the stored water due to lateral groundwater flow, as dependent on source water composition and pretreatment method. Exceedances of drinking water guidelines occurred long before the arrival of the native water. Fe(II) and Mn(II) exceedances, after having used desalinated and drinking water, respectively, were observed after a bubble migration of 9% and 40%, respectively, and were associated with the slightly acidic pH conditions promoting the dissolution of Mn-carbonate and preventing an efficient sorptive removal. The arsenic exceedances, after using urban storm water, were associated with the arsenic wave deriving from the pyrite oxidation and reaching the ASR well after 34% of bubble migration. Enrichment of the source water with O_2 and/or NaOH was also helpful in protecting the water quality around the ASR well for a longer time during a bubble migration scenario. The Fe(II) breakthrough occurred after 59% of desalinated bubble migration (instead of 9%) whereas As broke through after 70% of urban storm bubble migration (instead of 34%). This study illustrates that reactive transport modeling with a calibrated model is a useful tool to a-priori test the potential effectiveness of various operational options in ASR application on improving recovered water quality and the recovery efficiency.

Keywords: ASR, aquifer recharge, buffer zone, reactive transport modeling, scenario simulations, bubble drift, pyrite, iron, manganese, arsenic, recovery efficiency

4.1 INTRODUCTION

Aquifer storage recovery (ASR) is a method to balance water supply with demand. During periods of excess water, water is injected and stored in an aquifer for subsequent recovery for use in times of water demand (Pyne 2005). Sources of water suitable for injection and use within previous ASR applications include treated drinking water (Stuyfzand 1998a, Izbicki et al. 2010), treated or untreated groundwater (Pyne 2005), rainwater (Dillon and Barry 2005, Barry et al. 2007), high quality reclaimed wastewater (Vanderzalm et al. 2006, Maliva et al. 2007), urban storm water (Vanderzalm et al. 2010), and desalinated seawater (Mukhopadhyay et al. 2004, Rashid and Almulla 2005). The injection of oxygenated (surface) water into an anoxic environment, during ASR, may result in deterioration of the recovered water quality. Redox reactions involving reactive phases such as pyrite, carbonates and sedimentary organic material (SOM) may result, at least during the initial ASR cycles, in elevated concentrations of released Fe(II), Mn(II), arsenic and other trace elements such as nickel and cobalt (Stuyfzand 1998a, Pyne 2003). The removal of these elements requires further post-treatment of the recovered water, thus increasing the costs of the plant operation.

Minimizing the post-treatment requirements by achieving the largest possible recovery efficiency without water quality deterioration is the ultimate goal of most ASR plants. A buffer zone separates the stored water from the surrounding groundwater and defines the transition of injected water to native groundwater quality (Pyne 2005). In this study we investigate, by means of numerical simulations, how a careful buffer zone implementation may help to achieve high recovery efficiencies in a relatively short time. The “buffer zone” definition was therefore slightly modified into ‘the volume of source water required to separate the stored water from the native water in order to achieve a 100% recoverable bubble with respect to the various quality deteriorating elements’. The concept of such an approach is depicted in Figure 4.1 for a one dimensional linear flow line extending from the ASR well.

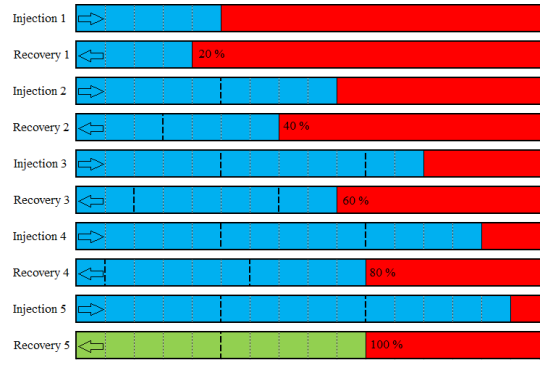

Figure 4.1. Simplified representation of a linear flow line extending away (to the right) from the ASR well. Here, a buffer zone (green cells), which allows 100% recovery efficiency with respect to the water quality, is gradually created. The mixing zone between the native (red cells) and the source (blue/green cells) water is depicted, for simplicity, as a sharp interface. Dashed lines indicate the equal volumes (5 cells) injected during each ASR cycle.

In Chapter 3 we successfully simulated the evolution of groundwater quality along one-dimensional radial flowlines representing two aquifer sublayers during a 9-year ASR pilot in Herten, the Netherlands. The aquifer consisted of 4 sublayers, each with different hydraulic and geochemical properties while the site consisted of one ASR well and two monitoring wells, M-8 and M-25 situated at 8 and 25 m distance, respectively (Figure 2.2). The PHREEQC (v. 2.17) model was calibrated based on cycle 1 and was sequentially validated by successfully predicting the water quality evolution during 14 subsequent cycles. In this study, we used this calibrated PHREEQC model and assumed the abstracted water quality to be solely defined by one aquifer layer (layer D) which played a decisive role in the water quality development due to the substantial amounts of pyrite and Mn-siderite present. In other words, we assumed ASR operations to be taking place in a homogeneous aquifer identical to layer D of the Herten pilot, and investigated the effect of three types of source water (pretreated drinking water from the previous study, desalinated seawater and urban stormwater) on the abstracted water quality with respect to Fe(II), Mn(II), and As. Mixing of water recovered from different aquifer layers was thus not considered for simplicity. This idealized situation served, however, as a worst case scenario for this specific ASR site where the recovered water quality cannot be improved by mixing (dilution) with higher quality water deriving from less “polluting” layers (layers A-C, Figure 2.2).

The scope of this study was to show how scenario modeling can be used to optimize an ASR system. For three representative source water types used for drinking water purposes pretreated drinking water, desalinated seawater, and urban storm water), we investigated how to implement an efficient buffer zone following an optimized cycling scheme. This optimization was achieved with the aid of a Python script coupled to PHREEQC which allowed recovery to halt when certain element concentrations exceeded predefined thresholds. We investigated whether an enrichment of the source water with O_2 and/or NaOH aids in accelerating the buffer zone build-up (i.e., uses less source water). We finally evaluated whether a migration of the injected water during storage has any adverse effects on the water quality due to water-aquifer reactions. We assessed that for each source water type in combination with the O_2 and/or NaOH enrichment.

4.2 MATERIAL AND METHODS

4.2.1 Reaction network

The most relevant redox processes and the respective rate expressions used were described in Chapter 3 and are summarized in Table 4.1. The oxidation of pyrite and sedimentary organic matter by oxygen from the source water, as well as the calcite and Mn-siderite dissolution were included in the model and simulated kinetically based on calibrations performed during the aforementioned study (Table 4.2). The trace element composition of pyrite was approximated as $FeAs_{0.008}S_{1.992}$ to allow for As release in the groundwater during the oxidation of pyrite. Iron and manganese react with the oxygen from the source water either in solution (homogeneous oxidation) or while adsorbed on metal oxide surfaces (heterogeneous oxidation). The homogeneous oxidation takes place when the cations (mainly calcium) from the injected water

exchange with iron and manganese releasing them in solution. Depending on the injection rate, the exchange reactions may be restricted to the initial stages of injection because after a while, the O_2 front will lag behind the injected water front and the released Fe(II) and Mn(II) will not be in contact with O_2 (Appelo et al. 1999). The homogeneous oxidation of Mn(II) was not included due to extremely slow reaction rates (Diem and Stumm 1984). The heterogeneous oxidation of adsorbed Fe(II) and Mn(II) was not included in the original model (Chapter 3). Including it in the new model had negligible effects on the dissolved Fe(II) concentrations and on the water quality in general due to the low initial ferrihydrite content. Recalibrating the model was considered superfluous. The two reactions were included for integrity reasons since they are relevant processes that may acquire a significant role when the initial ferrihydrite content is higher. In that case, a model recalibration may be required.

The kinetic simulation of the iron and manganese oxidation required a modification of the PHREEQC database in order to decouple the valence states of iron and manganese and calculate the kinetic oxidation of Fe^{2+} to Fe^{3+} and of Mn^{2+} to Mn^{4+} in water (Parkhurst and Appelo 2013). Oxidation of As(3) to As(5), cation exchange, and the formation of ferrihydrite that follows the oxidation of Fe(II) were simulated as equilibrium processes.

Finally, the oxidation of dissolved organic carbon (DOC) present in the source water was ignored in the original model due to the low measured concentrations (<0.08 mmol/L) which showed recalcitrant behavior towards oxidation. Higher DOC concentrations in the source water are however expected to oxidize at faster rates. Therefore a first-order degradation rate with a rate constant of 0.1 (d^{-1}) (Schäfer 2001) was introduced during the scenario simulating the injection of urban storm water (Section 4.3.2).

The sorption to ferrihydrite was simulated by using the surface complexation model of Dzombak and Morel (1990). In this two-layer model, chemical binding is distributed over weak (low affinity) and strong (high affinity) sites, which exist in a proportion of 0.2 and 0.005 mol sites / mol ferrihydrite, respectively. The increasing complexation capacity with increasing amounts of ferrihydrite precipitates was modeled by coupling the moles of the surface sites to the mass of ferrihydrite in the system (Appelo and Vet 2003). The binding constants (apparent dissociation constants) for sorption of the most relevant elements (Fe, Mn, As, HCO_3, PO_4, SO_4) on the ferrihydrite surface complex (Hfo) were obtained from the WATEQ4F database included with PHREEQC. The adsorption constant of silicic acid (H_4SiO_4) was obtained from Swedlund and Webster (1999) and was added to our modified PHREEQC database.

4.2.2 Source water types

The compatibility of different source water types with the Herten aquifer was tested by means of scenario simulations. Representative source water compositions were obtained from other lab/full scale ASR studies and are summarized in Table 4.4. The desalinated water produced in Kuwait using multistage flash technology (Mukhopadhyay et al. 1998) contained, as expected, very low amounts of dissolved salts and was significantly undersaturated with respect to calcite.

Table 4.1. Kinetic reaction network considered in the model

Nr	Process	Reaction equation	Reference
1	Pyrite oxidation	$r_{pyrite} = k_{pyr} m_{O_2}^{0.5} m_{H^+}^{-0.11} \left(\frac{A_{pyr}}{V}\right)\left(\frac{m}{m_0}\right)_{pyr}^{0.67} \left(1-\Omega_{pyr}\right)$	Williamson and Rimstidt (1994)
2	SOM oxidation	$r_{SOM} = m_{SOM}\left(\frac{m}{m_0}\right)_{SOM}\left(r_{max(O_2)}\frac{m_{O_2}}{k_{O_2}+m_{O_2}}\right)$	Van Cappellen and Gaillard (1996)
3	Calcite dissolution	$r_{cal} = \left(k_1\left[H^+\right]+k_2\left[CO_2\right]+k_3\left[H_2O\right]\right)\left(\frac{A_{cal}}{V}\right)\left(\frac{m}{m_0}\right)_{cal}^{0.67}$	Plummer et al. (1978)
4	Mn-siderite dissolution	$r_{sid} = \left(k_1\left[H^+\right]^{0.65}+k_2\left[CO_2\right]^{0.65}+k_3\right)\left(\frac{A_{sid}}{V}\right)\left(\frac{m}{m_0}\right)_{sid}^{0.67}\left(1-\Omega_{sid}\right)$	Descourvieres et al. (2010)
5	Fe^{2+} oxidation (homogeneous)	$r_{Fe^{2+}} = -\left(k\left[OH^-\right]^2 P_{O_2}\right)m_{Fe^{2+}}$	Singer and Stumm (1970)
6	Fe^{2+} oxidation (heterogeneous)	$r_{Fe^{2+}_{ads}} = -k \times m_{Fe^{2+}_{ads}} \times m_{O_2}$	Tamura et al. (1976)
7	Mn^{2+} oxidation (heterogeneous)	$r_{Mn^{2+}_{ads}} = -k \times m_{Mn^{2+}_{ads}} \times P_{O_2}$	Davies and Morgan (1989)

Table 4.2. Model aquifer parameters. Initial contents and calibrated reactive surface areas of each mineral (A) to solution volume (V).

CEC	pyrite	SOM	calcite	Mn-siderite	ferrihydrite	A_{pyr}/V	A_{cal}/V	A_{sid}/V
mol/L							m^2/L	
0.2	0.05	2.09	0.093	0.133	0.09	0.44	2.98×10^{-4}	2.9×10^{-4}

Table 4.3. Native groundwater quality (layer D in Herten aquifer). TIC stands for "Total Inorganic Carbon" and SI for "Saturation Index".

Temp	pH	O_2	Cl	SO_4	TIC	NO_3	Na	K	Ca	Mg	SiO_2	PO_4	Fe	Mn	As	SI_{cal}	SI_{sid}
°C		mmol/l										µmol/l					
13.2	6.8	<0.02	0.17	<0.03	8	<0.01	0.35	0.04	2	0.51	0.35	2.6	127	7	0.13	-0.4	0.7

Table 4.4. Composition of the three source water types used in simulations.

Source water	temp	pH	O_2	Cl	SO_4	HCO_3	Na	K	Ca	Mg	NO_3	DOC	SiO_2	SIcal
	°C		mmol/l											
Pretreated drinking water (Antoniou et al. 2012)	13	7.5	0.28	1.11	0.64	2.71	1.05	0.06	1.71	0.27	0.02	0.092	0.14	-0.14
Desalinated water (Mukhopadhyay et al. 1998)	30	6.9	0.28	1.63	1.24	0.30	2.04	0.04	0.84	0.57	0.03	<0.005	0.04	-1.93
Urban storm water (Vanderzalm et al. 2010)	12	7.1	0.28	0.76	0.11	1.46	0.83	0.09	0.57	0.18	<0.001	0.525	-	-1.13

In all source water types: Fe < 0.1, Mn < 0.1, As < 0.01, NH_4 < 50 µmol/L

The urban storm water from a mixed residential and industrial catchment area in the City of Salisbury (South Australia) was characterized by both a relatively high DOC concentration and calcite undersaturation (Vanderzalm et al. 2010). None of the tested water types showed any exceedances of drinking water guidelines making them good candidates for potable water ASR.

4.2.3 Transport parameters

Due to the absence of a well package in PHREEQC, the concepts of injected volume and well rates are not directly available like in other 3D modeling software (Modflow, PHAST). Transport

in PHREEQC is described by means of shifts and time steps for a specified number of cells. Shifts refer to the number of times the solution in each cell will be shifted to the next higher numbered cell. This is therefore the only parameter that can be used to simulate the extension of the ASR bubble with distance and is hence used to simulate the injected and the abstracted volumes. The time step is calculated by dividing the total time (in seconds) with the respective number of shifts. Reactive transport was simulated along a flow line that extends from the ASR well on a radially decreasing grid (Chapter 3). The number of cells should be able to accommodate the maximum number of shifts performed during any of the simulated injections. This number of cells ensures that the conservative dispersed front of the injected water stays within the simulated volume. The longitudinal dispersivity was set to 0.1 m, assuring a good simulation of the conservative solute transport, as verified in the original model.

The original PHREEQC model was further coupled to a Python script that allowed for the recovery to automatically halt when certain element concentrations in the recovered water exceeded specified thresholds (Fe = 3.6, Mn = 0.9, As = 0.13 µmol/L). The script was able to read the model output after each recovery shift (using the new DUMP and INCLUDE$ functions introduced in PHREEQC v. 3.0), and if concentrations were below the specified thresholds, another shift would be performed. When a threshold was exceeded then injection would start again. This approach was necessary to simulate the gradual creation of a buffer zone that would allow 100% bubble recovery at a specific stage of aquifer development (Section 4.3.4).

The effects of bubble migration were modeled by slowly letting the native water approach the ASR well. This was performed by increasing accordingly the time step simulating the background groundwater flow towards the ASR well. The linear flow of native water could not be simulated with the radial grid used to simulate ASR around the well. After the buffer zone was developed, the grid was converted into a linear 1-m cell grid by looking at the cumulative cell length and copying (using the COPY command in PHREEQC) the respective cells from the radial grid.

4.3 RESULTS AND DISCUSSION

The results are structured as follows: The injection of pretreated drinking water is analyzed first. The hydrogeochemical effects are analyzed during a single and multiple ASR cycles and attention is given to the behavior of Fe(II), Mn(II), and As. Optimizing the recovery efficiency is evaluated next for the three source water types. Optimization is assessed by means of buffer zone creation and source water enrichment. Finally, the effects of bubble migration are assessed.

4.3.1 Analysis of a single ASR cycle

Fe(II) and Mn(II) behavior

For this simulation, Mn-siderite was excluded to rule out its influence on the Fe(II) and Mn(II) concentrations and thereby better inspect their behavior solely due to the

oxidation and the sorption/desorption processes. The injection and recovery phases were divided into 100 shifts with a duration of 2.4 hours each, and the source water (pretreated drinking water; Table 4) during injection reached a distance of 10 m (50% conservative breakthrough). The simulated travelled distance of the injected front was comparable to the one observed taking place in layer D in the Herten aquifer (Chapter 3), whereas the chosen time step was considered suitable for the simulation of fast kinetic reactions, such as the oxidation of ferrous iron and manganese. A significant bromide contrast between the source and native water was artificially created to compare its conservative behavior with Fe(II) and Mn(II) and to observe the gradual evolution of the dispersive mixing.

The simulated O_2 front during injection was significantly retarded due to various oxidation processes (Figure 4.2). The 10-day storage was responsible for complete consumption of the remaining O_2. During injection, the development of the simulated dissolved Fe(II) and Mn(II) fronts was the combined result of (1) the displacement by the injection water, (2) the homogeneous oxidation after their release from pyrite (during its oxidation) and from the exchange complex by mainly calcium in the source water, and (3) the heterogeneous oxidation of their fractions adsorbed to iron-oxide. Small amounts of released Fe(II) and Mn(II) sorb during the injection to ferrihydrite as simulated by the adsorbed Fe(II) and Mn(II) "wave" moving outward from the ASR well (first 3 m). The heterogeneous oxidation had a negligible influence on the overall O_2 consumption and on the development of the dissolved fractions due to the small ferrihydrite content. During the recovery, Fe(II) and Mn(II) desorb from the outer sorption zone due to decreasing pH conditions related to the inflowing native water having a lower pH than the injection water (Buamah et al. 2008). Both cations sorb again as they approach the ASR well due to the additional ferrihydrite formed during injection. However, the sorbing fractions are small and the bulk dissolved content increases in the ASR well (Figure 4.2).

Including the Mn-siderite has a direct effect on the behavior of the dissolved Fe(II) and Mn(II) (results not shown). A minor dissolution of this mineral during the storage and recovery, driven by the undersaturation of the injection water with respect to this mineral (SI = -2.2), resulted in the release of Fe(II) and Mn(II). The released Fe(II) did not pose any concerns in Herten since after a couple of ASR cycles it sorbed again on the ferrihydrite surfaces before reaching the ASR well. Mn(II), however, showed a much less effective removal with consecutive cycles due to its high pH requirements for an efficient sorptive removal.

As behavior

Arsenic did not pose major concerns in the Herten aquifer. Despite the appreciable levels (up to 0.15 µmol/L) recorded in the monitoring wells during the injection pointing to the mobilization by oxidative pyrite dissolution, the recovered concentrations did not exceed the WHO drinking water guideline (0.13 µmol/L). The simulated behavior of arsenic after its release during the pyrite oxidation was a combined result of the adsorption and desorption processes mainly governed by the native water composition.

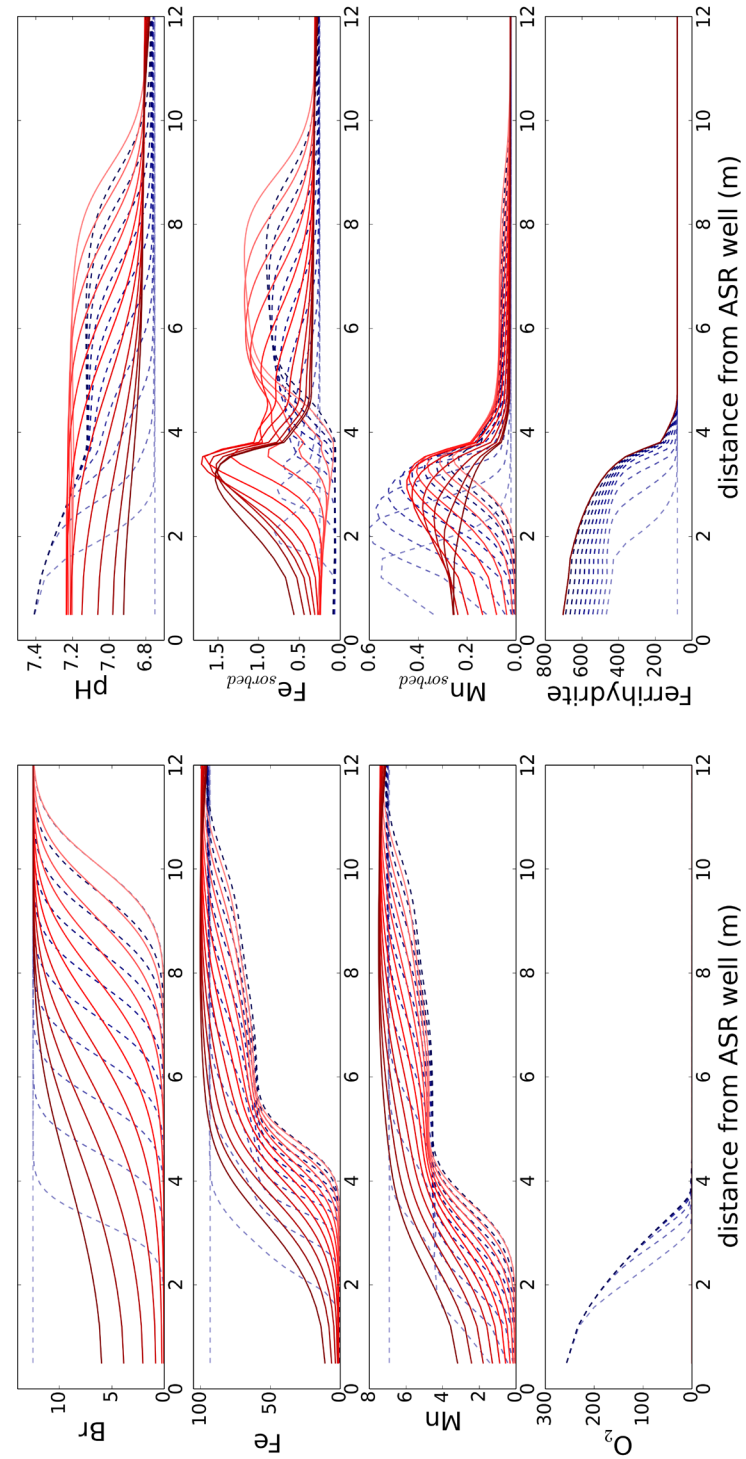

Figure 4.2. Spatial evolution of the dissolved and adsorbed (on ferrihydrite) Fe(II) and Mn(II) during successively a 10-day injection, storage, and recovery phase. Ferrihydrite formation, O_2, and conservative Br are also plotted. Blue dashed lines represent injection (daily from light to dark blue). Red lines represent recovery (daily from light to dark red). All aqueous concentrations and solid contents are expressed in µmol/L.

We analyzed the influence of the native phosphate and ferrous iron concentrations on the simulated behavior of arsenic around the ASR well. Generally, when arsenic is mobilized during the pyrite oxidation (as As(3) arsenite) it oxidizes to As(5) (arsenate), which in turn sorbs on the existing and newly formed ferrihydrite surfaces. This process takes place during the injection, storage and recovery phases as long as there is available oxygen to oxidize the pyrite and arsenic released. In the absence of phosphate, the mobilized As sorbs efficiently on ferrihydrite without much effect on the recovered water quality (Figure 4.3, Row 1). According to the simulations, the drinking water guideline is only exceeded when recovering > 90% of the injected water, a recovery ratio that is much higher than the actual initial ratio applied in Herten (30%). Including, however, the phosphate concentration measured in the native groundwater (2.6 µmol/L) posed significant competition to the negatively charged As(5) (arsenate) for the sorption sites of ferrihydrite due to the negative charging of the ferrihydrite surface (Appelo and Vet 2003). As a result, desorption of As occurs as soon as the native groundwater with high PO_4^{3-} concentration contacts the ferrihydrite surface during the recovery. Nevertheless, as modeled in Figure 4.3 (Row 2), the simulated "wave" of the desorbing As does not reach the ASR well before recovering 90% of the injected water. A similar pattern was observed during the recovery between the monitoring wells and the ASR well in the Herten aquifer. Besides phosphate, dissolved silica has been found to compete with arsenic for the sorption sites on ferrihydrite (Swedlund and Webster 1999). Including the measured native silica concentration (0.32 mmol/L) resulted in additional arsenic mobilization (results not shown). The effect, however, was smaller as compared to the effect of phosphate and, again, the simulated arsenic wave did not reach the ASR well before recovering 100% of the injected water.

In contrast to the effect of phosphate and silica, the sorption of arsenate is enhanced by sorption of Fe(II), because it charges the surface positively (Appelo and Vet 2003). The "abundant" native Fe(II) in the Herten aquifer was possibly the main reason for the lack of As in the abstracted ASR water. Decreasing the native Fe(II) concentration (to 27 µmol/L – 70% decrease) resulted in the simulated As wave reaching the ASR well after having abstracted 80% of the injected water and the concentration greatly increasing in the final fraction of the recovered volume (Figure 4.3 - Row 3). Low Fe (and Mn) concentrations may also be expected in aquifers with high HCO_3^- in the native water (e.g. during aquifer freshening) which promotes the precipitation of Fe/Mn-carbonates. Moreover, the HCO_3^- anion, when in high concentrations, poses major competition for the adsorption sites on ferrihydrite (Gao et al. 2011) and may displace arsenic and especially arsenite since they both form neutral surface complexes (Appelo and Vet 2003). Such aquifers, therefore, are also prone to arsenic exceedances during ASR activities.

4.3.2 Effects of multiple cycles on abstracted water quality

The model was allowed to run for 10 fully-recovering (100%) cycles and the spatial distributions of the various concentrations were plotted at the end of each injection and each

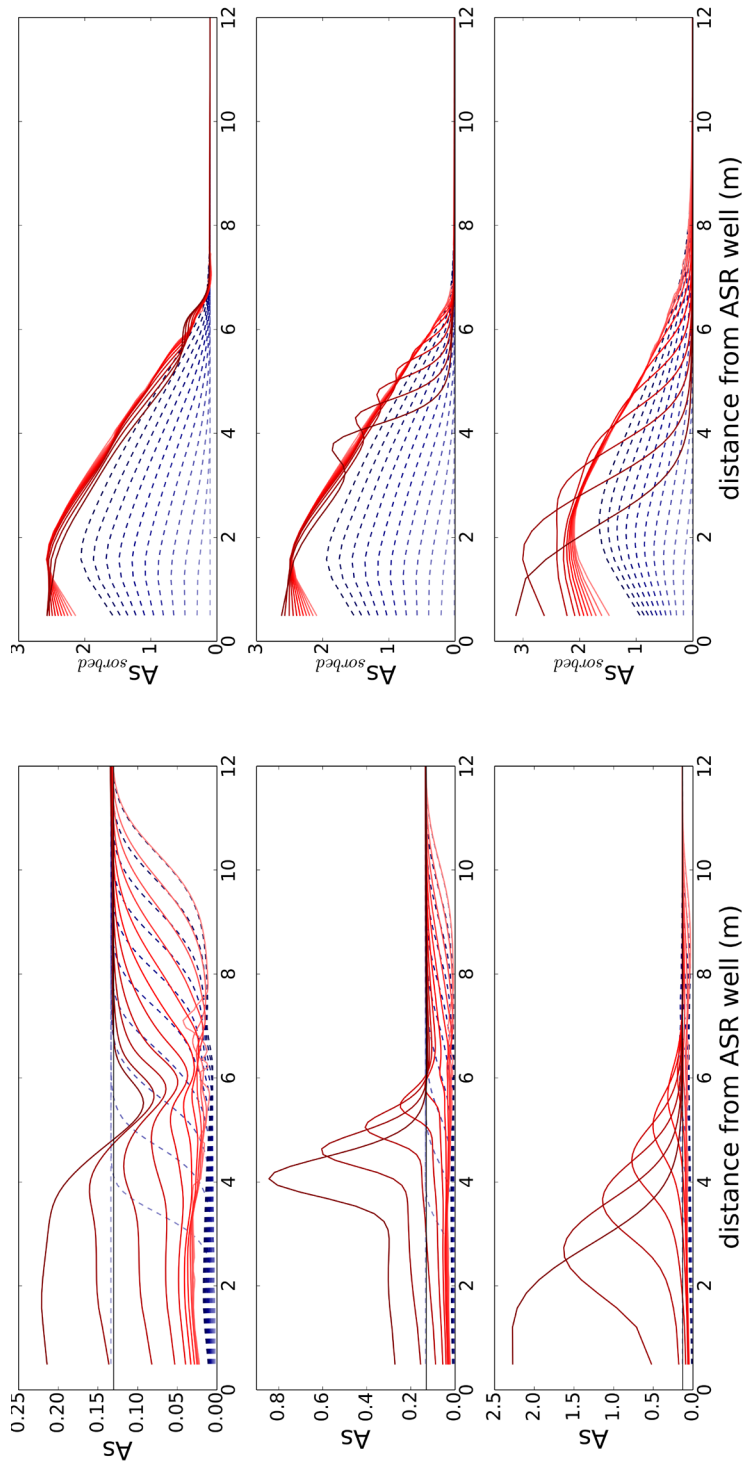

Figure 4.3. Spatial evolution of dissolved (left) and adsorbed (on ferrihydrite, right) arsenic (total) during one ASR cycle (10 days injection, 10 days storage and 10 days recovery) for 3 scenarios: (Row 1) native groundwater composition without PO_4, (Row 2) native groundwater composition including measured PO_4, (Row 3) native groundwater composition with PO_4 but with low Fe(II). Blue dashed lines represent injection (daily from light to dark blue). Red lines represent recovery (daily from light to dark red). All aqueous concentrations and solid contents are expressed in µmol/L.

recovery phase. This approach helped visualizing how, in the absence of Mn-siderite, the abstracted water quality gradually improves solely due to the cumulative water-sediment reactions. The model results are presented in Figure 4.4. The most important observation is that the simulated dissolved Fe(II) and Mn(II) fronts gradually penetrate deeper into the aquifer with every ASR cycle. The transient character of the well operation where the recovery stops (at 100%) before the native iron concentration reaches the well (Figure 4.4), causes an incomplete refill of the exchanger and allows the oxygen in the following injection to penetrate further into the aquifer (Appelo et al. 1999). This additional oxygen, in combination with a cumulative increase of iron hydroxide precipitates (Figure 4.4) provides expanding adsorptive surfaces with every cycle (Van Beek 1983, Rott and Friedle 1985). Also, the gradually increasing pH conditions slowly facilitate the Fe(II) and Mn(II) adsorption on the ferrihydrite surfaces. As a result, the recovery efficiency with respect to Fe(II) and Mn(II) gradually increased. The model predicted a gradual concentration build-up for adsorbed As (Figure 4.4) resulting in a gradual improvement in the recovery efficiency also with respect to As.

4.3.3 Optimization – building a buffer zone

Usually, the first stages (cycles) of a new ASR application are dedicated to “prepare” the aquifer for a safe ASR usage. Such preparation can be achieved by different means, such as by creating a buffer zone that separates the stored water from the surrounding native water or by injecting oxidant-rich water in order to accelerate the aquifer depletion/ deactivation of its reactive phases which deteriorate the water quality. This deactivation is usually due to the increased Fe-hydroxide precipitation at the surface of the pyrite crystals, which inhibit pyrite’s further oxidation and at the same time increase the sorption capacity of the sediments (Evangelou 1995). A combination of both techniques is usually followed.

An efficient way to achieve a recovery efficiency of 100% with respect to a specific element is by performing a series of ASR cycles where the recovery stops as soon as the recovered concentration of the element exceeds the drinking water guideline. Despite these first cycles producing less water compared to the injected volume, the abstracted water can, of course, still be used as drinking water. An element-specific buffer zone is thus created, which allows for a recovery efficiency of 100%.

For the three types of source water, we simulated during 10 consecutive cycles the gradual evolution of the recovery efficiency with respect to iron, manganese, and arsenic (Figure 4.5). Mn-siderite was now introduced as it reflected the main problematic phase. The injection always consisted of a fixed volume of water (100 cell shifts), whereas the recovery automatically halted when the drinking water guideline with respect to any of these elements was exceeded in the ASR well. This way, the ASR bubble increased progressively in volume while at the same time a buffer zone was created shifting the processes responsible for the water quality deterioration further away from the ASR well. The cycling was stopped when a recovery efficiency of 100% with respect to each element was achieved. Each scenario had

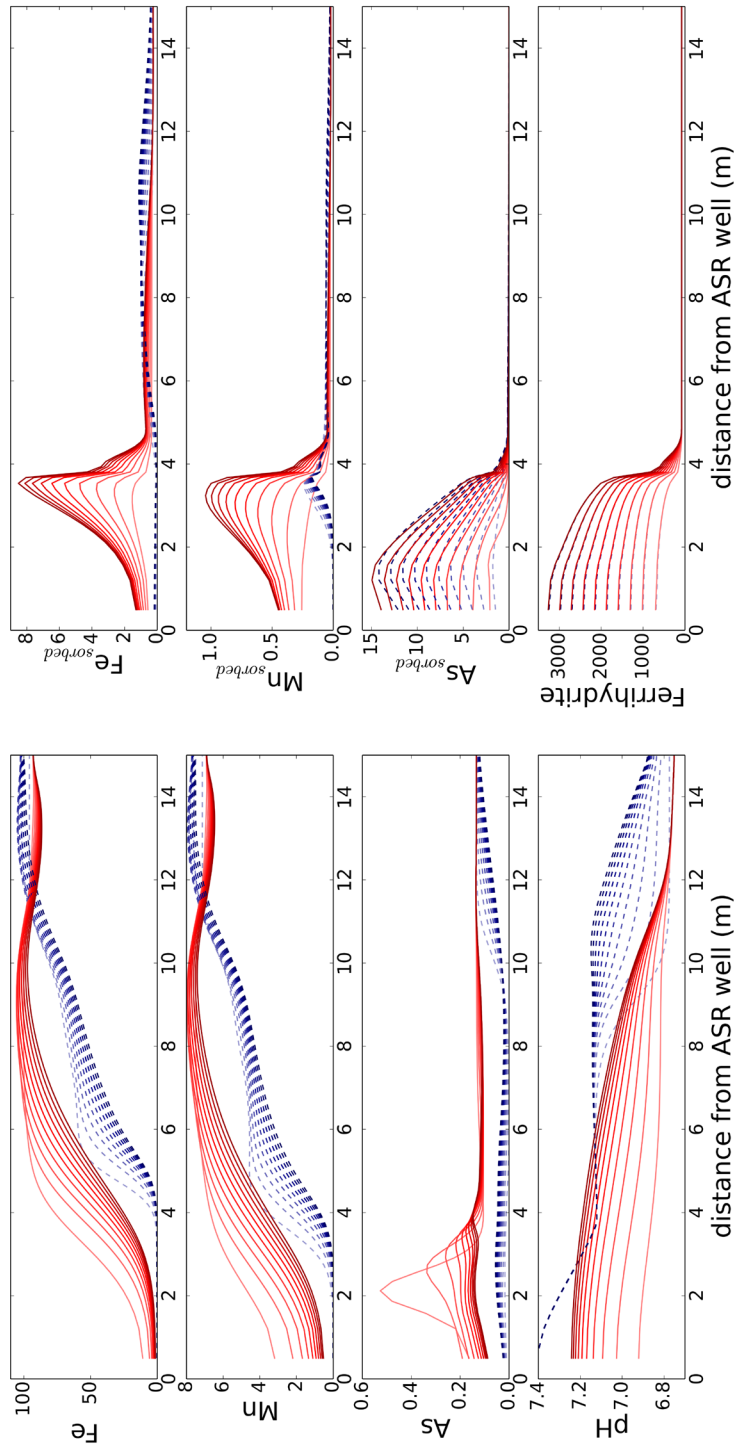

Figure 4.4. Spatial evolution of dissolved and adsorbed (on ferrihydrite) Fe(II) and Mn(II) at the end of each injection, storage and recovery phase of 10 ASR cycles. Ferrihydrite formation and pH are also plotted. Blue dashed lines represent the end of each injection phase (injection 1: light blue, injection 10: dark blue). Red lines represent the end of each recovery phase (recovery 1: light red, recovery 10: dark red). Pretreated drinking water was used as a source. All aqueous concentrations and solid contents are expressed in µmol/L.

different cycling requirements before achieving 100% recovery efficiency, thus resulting in different bubble volumes.

Scenario 1: Pretreated drinking water

Iron related problems were almost absent during the injection of the pretreated drinking water, in line with the observations during the Herten ASR pilot. The simulated pH did not decrease to such low levels (pH > 6.8) that would complicate the sorption of Fe(II). Manganese showed higher cycling requirements (5 cycles) before getting efficiently removed, whereas arsenic was absent straight from the beginning of the simulated ASR operation (Figure 4.5a).

Scenario 2: Desalinated seawater

The slightly lower pH of the desalinated source water in combination with the oxidation reactions resulted in a simulated pH value of ~6.3 in the aquifer (result not shown) promoting some additional Mn-siderite dissolution as compared to the injection of the pretreated drinking water (Table 4.4). Additionally, the low pH conditions inhibited the effective sorptive removal of Fe(II) and Mn(II) during recovery. This increased the required number of cycles to 8 (80% with respect to the drinking water injection) before achieving 100% efficiency with respect to manganese, whereas iron showed a very slow improvement allowing only ~40% recovery efficiency after increasing the number of cycles to 25 (Figure 4.5b).

Scenario 3: Urban storm water

The injection of urban storm water was mainly characterized by the consumption of an appreciable O_2 fraction (~24%) by DOC in the source water decreasing, as a consequence, the extent of the simulated pyrite oxidation and the consequent ferrihydrite formation (results not shown). In contrast with the other two types of source water, arsenic exceeded the drinking water guideline in the recovered water at recovery ratios > 70% (Figure 4.5C). The oxidation of DOC generated HCO_3^- which competed with arsenic for available sorption sites during recovery (Appelo et al. 2002). The lower pH conditions (~6.5) impeded again the efficient Fe(II) and Mn(II) sorption during the recovery which led to their break-through in the ASR well right away. The injection of urban storm water delayed the optimization with respect to iron (by 200% compared to the drinking water scenario) as observed in Figure 4.5c. The simulated arsenic, however, posed a persisting problem limiting the recovery efficiency to ~80% and delaying the implementation of an effective buffer zone. During the urban storm water scenario, we furthermore tested restarting the injection before arsenic exceeded the drinking water standards (results not shown). This early restart, however, did not improve the temporal evolution of the recovery efficiency. In fact, the simulated cycling schemes in Figure 4.5c proved to be the most efficient ones for each element.

As already mentioned, the break-through of the arsenic wave during the first cycle was dependent on the concentrations of various elements and compounds such as phosphate, silicate, and ferrous iron. The influence of these elements becomes unnoticeable during

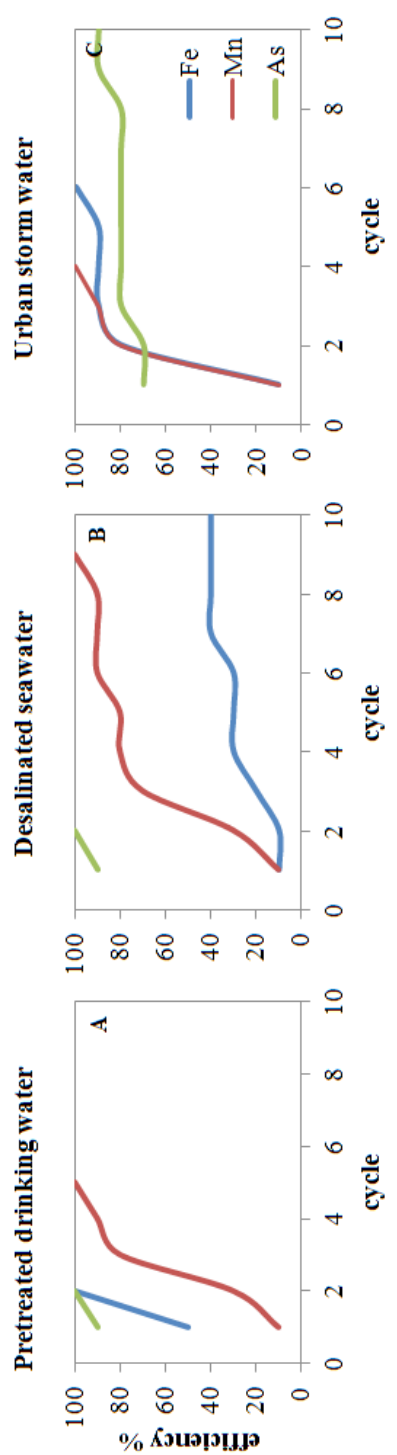

Figure 4.5. Recovery efficiency improvement with increasing number of ASR cycles with respect to Fe(II), Mn(II), and arsenic for the 3 source water types. Each cycle: 10 days injection, 10 days storage and 10 days recovery.

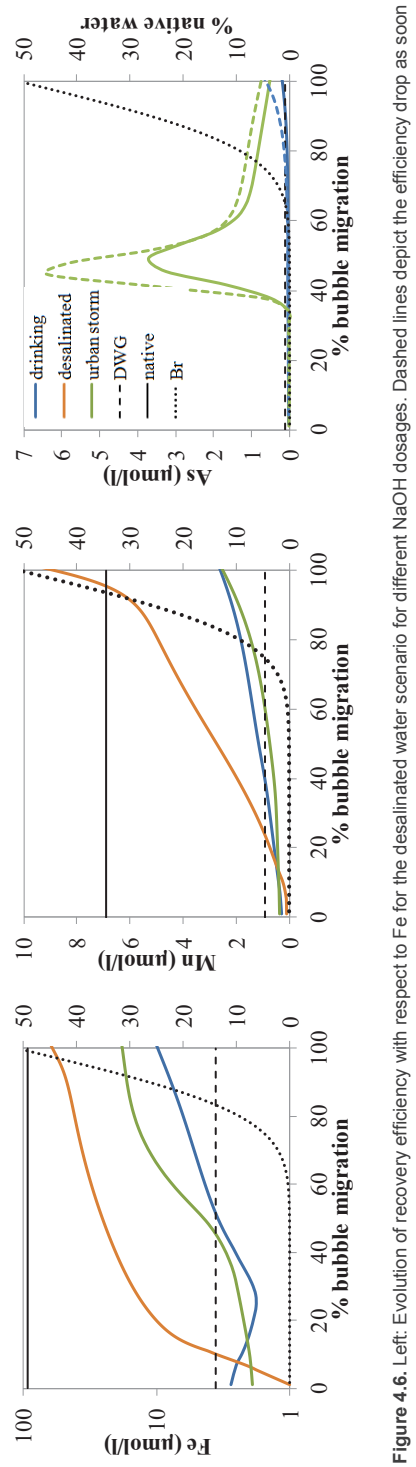

Figure 4.6. Left: Evolution of recovery efficiency with respect to Fe for the desalinated water scenario for different NaOH dosages. Dashed lines depict the efficiency drop as soon as dosing stops. Right: pH of recovered water by the end of each cycle for the different dosing scenarios.

the simulated creation of the buffer zone since the native water is sequentially pushed further and does not interfere with the sorption sites in the storage zone. Care should be taken, however, when the source water itself contains substantial phosphate and/or silicate concentrations, as this may have adverse effects on the arsenic behavior.

4.3.4 Optimization – dosing agents

The implementation of a buffer zone can be accelerated by using pH-buffering agents such as NaOH and Na_2CO_3 to increase the alkalinity and pH of the aquifer around the ASR well, and to prevent the dissolution of carbonate minerals as a response to undersaturated source waters or acidifying water-aquifer interactions. Additionally, an efficient sorption of Fe(II) and especially Mn(II) on the Fe-hydroxides (and Mn-oxides) formed during the injection of oxic water requires a pH > 7.5 (Buamah et al. 2008). The effect of dosing a pH buffer has been experimentally tested in real scale ASR pilots in Virginia and South Carolina which suffered from Fe and Mn concentration exceedances in the recovered water (Ibison et al. 1995, Pyne et al. 2013). It has also been shown by numerical simulations (Chapter 3) that the Mn(II) mobilization in the Herten aquifer can be reduced by enriching the source water with 0.8 mmol/L of O_2 and/or 0.5 mmol/L of NaOH. We used NaOH in our simulations because of its ease of injection and handling and its high base solubility. However, due to the relatively high cost in comparison to other sources of soluble base, NaOH may not be the ideal chemical for practical treatment.

The usefulness of this treatment technique is studied in more detail in the following by assessing its effectiveness with respect to the different source water types and by identifying the relevant issues associated with each one of them. O_2 and NaOH dosing in the model was performed in increments in order to observe how Fe(II) and Mn(II) behave. The results are depicted in Figure 4.6 for the desalinated and in Figure 7 for the urban storm water scenarios.

The Fe(II)-related problems, encountered when using desalinated water, were successfully treated with low NaOH dosages, which accelerated the implementation of an efficient buffer zone. The small pH increase was enough to reduce the dissolution of Mn-siderite around the ASR well and improve the recovery efficiency with respect to Fe(II) (Figure 4.6). The abstracted Mn(II) was of secondary importance and did not break through before Fe(II) did. Stopping the NaOH dosage resulted in a sudden drop in the recovery efficiency towards the scenario without NaOH addition (dashed lines). It is expected that NaOH dosage should be continued, even after 100% efficiency is reached. In this particular case of desalinated water, the cycling requirements compared to the scenario without NaOH depend on the NaOH dosage and follow the linear relationship $y = -0.32x + 71.7$ (R^2 = 0.988), where x is the NaOH concentration added and y is the percentage of cycling requirements relative to the scenario without NaOH dosage. For example, a 100 µmol/L dosage of NaOH should continue for a number of cycles equal to 40% (20 cycles) of the number of cycles required when no NaOH is added to the desalinated water (49 cycles). This relationship was found to be valid for x ≥ 30 µmol/L.

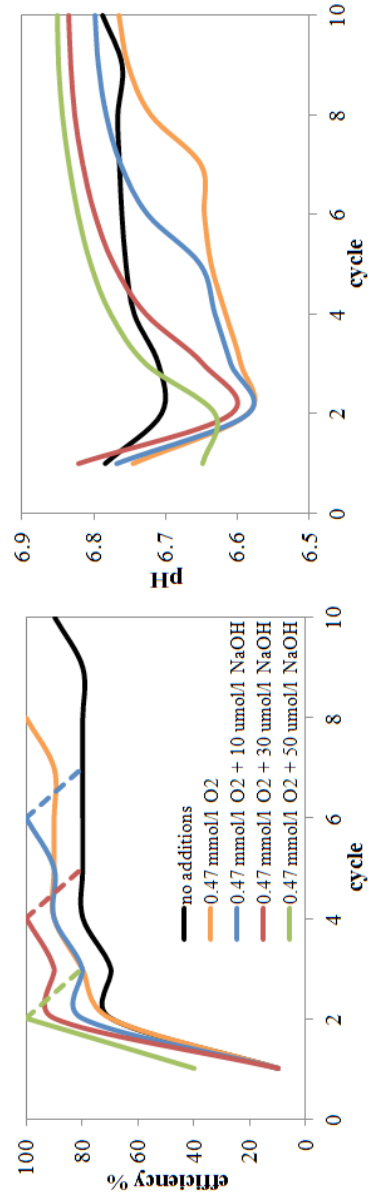

Figure 4.7. Left: Evolution of recovery efficiency with respect to As for the urban storm water scenario for different O_2 and NaOH dosages. Dashed lines depict the efficiency drop as soon as dosing stops. Right: pH of recovered water by the end of each cycle for the different dosing scenarios.

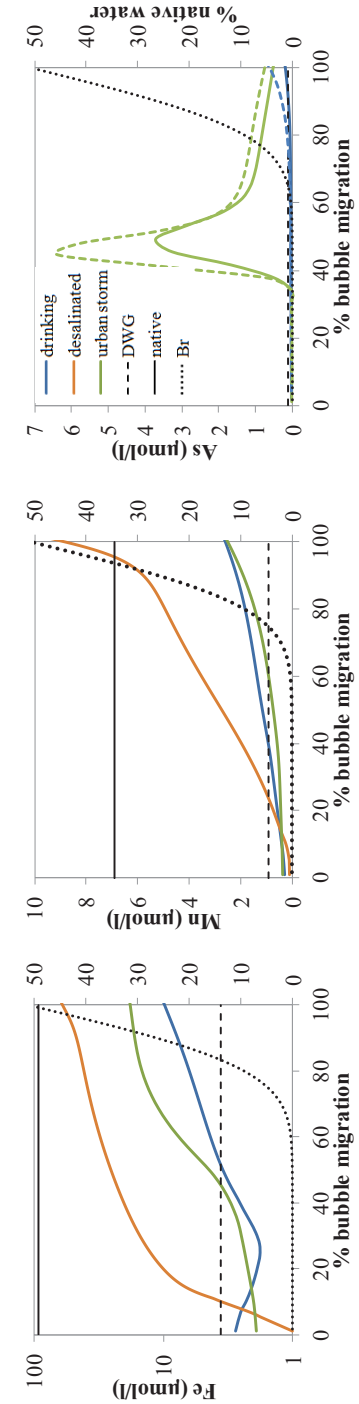

Figure 4.8. Evolution of water quality in the ASR well during a 100% complete bubble migration after having created a 100% efficient buffer zone with the 3 types of source water. The evolution of As is also presented (blue/green dashed line) for a scenario with low native Fe(II) concentration (27 µmol/L). The dispersed native water front is plotted on the secondary y axis. DWG = Drinking Water Guideline.

Building a buffer zone using urban storm water proved to be a more complicated task. Enriching the source water with O_2 (0.47 and 0.63 mmol/L) resulted in an increased pyrite oxidation and consecutively in a more extended ferrihydrite precipitation. This enhanced ferrihydrite formation, in combination with a pH decrease (Figure 4.7), facilitated the sorption of arsenic and accelerated the implementation of an efficient buffer zone with respect to this element. The increased acidification, however, promoted the dissolution of Mn-siderite, which, due to enhanced Mn(II) and especially Fe(II) concentrations, limited the successful implementation of a buffer zone. In other words, the treatment turned Fe(II) into the efficiency-controlling element since its concentration exceeded the drinking water guideline before As did. In order to improve the As sorption without causing Fe or Mn problems, a fixed O_2 dosage (0.47 mmol/L) was combined with various levels of NaOH addition (Figure 4.7). The discontinuation of the treatments resulted in a declining recovery efficiency indicating again that the dosage should be continued even after the As-specific buffer zone is achieved. In this case, however, the source water treatment should continue for a number of cycles equal to the one required without dosage. The positive effects of the various treatment methods are summarized in Table 4.5. We conclude that, when using pH buffers and O_2 enrichment to improve the recovery efficiency during the implementation of a buffer zone, the behavior of all critical elements should be carefully monitored since, by changing the aquifer conditions, we might also change the order of the efficiency-limiting elements.

Adding NaOH or any other buffer solution to the source water should be in agreement with the permissible dissolved elemental concentrations in the groundwater. In the Netherlands, a health-based standard value of 6.52 mmol/L has been established for the dissolved Na. Above 8.7 mmol/L, sodium may affect the taste of drinking water. Even after a NaOH dosage, sodium levels remain well below such levels rendering the technique safe from that perspective. The bulk prices range between US $300-500/ton for high purity (99%) sodium hydroxide, depending on the ordered amount. For the highest NaOH dosage tested (0.1 mmol/L) the corresponding costs would thus be 1.2 – 2 dollar cents/m^3 water.

The precipitation of calcite may occur around the ASR well upon the injection of water to which a pH buffer such as NaOH has been dosed. A total calcite precipitation of about 0.5 mmol/L was estimated to take place around the ASR well during the maximum NaOH dosage tested (0.1 mmol/L during the desalinated water scenario). Such concentrations could potentially cause clogging issues and injectivity problems, so care should be taken when applying this technique to the field.

4.3.5 Effects of bubble migration

The migration of the ASR bubble could be an issue depending on the background groundwater flow velocity and the duration of the storage phase. In case of bubble migration, the inflow of mixed and eventually native groundwater may result in further water quality degradation. The effects of the bubble migration after reaching 100% recovery efficiency were modeled by slowly letting the native water approach the ASR well. The simulated water quality at the ASR well was monitored for a period required for the complete bubble migration (at 0.02 m/d for the specific aquifer layer) or, in other words, until the native water reached the ASR well (50% breakthrough) (Figure 4.8).

It is clear that the bubble migration caused water quality deterioration long before the arrival of the native water. For the drinking water, a bubble migration of 40% (340 days) was enough to cause Mn(II) exceedances in the ASR well, whereas Fe(II) surpassed the drinking water guideline after 52% (442 days) of bubble migration. The low pH conditions associated with the injection of the desalinated water, promoting the Mn-siderite dissolution and inhibiting an efficient sorptive removal, resulted in Fe(II) problems after only 9% (198 days) of bubble drift. The high cycling requirements before achieving a 100% efficiency using desalinated water makes this a far worse scenario than when using drinking water. The desalinated water scenario resulted also in the Mn(II) exceeding the drinking water guideline after 23% (506 days) of bubble drift. As discussed earlier, the injection of urban storm water resulted in water quality deterioration mainly with respect to arsenic. Building a buffer zone aimed at deflecting the arsenic wave away from the well, so that it does not appear before achieving 100% recovery efficiency. As expected, the arsenic wave reached the well after 34% (272 days) of bubble migration reaching its peak at 49% (392 days) far above background concentrations (Figure 4.8). The concentration then decreased again as PO_4 (not shown) and higher Fe(II) concentrations reached the ASR well. Even though the water quality reached prohibitive levels before the arrival of the native water, this does not mean that the native water composition is an irrelevant factor. The spatial distribution of the sorptive surfaces during the development of the buffer zone is directly related to the native water composition and may influence indirectly the water quality during a future bubble migration. As observed in Figure 4.8, the lack of Fe(II) in the native water during the development of the buffer zone results, during the urban storm water scenario, in a stronger As breakthrough (dashed lines) reaching its peak after the bubble has migrated by 45% (360 days).

The source water treatment (with O_2 and/or NaOH) during the creation of the buffer zone not only serves in accelerating the buffer zone completion but also in protecting the water quality around the ASR well during a long stand-still period where bubble migration may occur. As observed in Figure 4.9, the Fe(II) exceedances were successfully delayed with increasing NaOH concentrations used, due to the higher pH conditions around the ASR well. The early Fe(II) onset after only 9% of bubble migration was shifted to 59% (413 days) when the buffer zone was created by adding 100 µmol/L of NaOH to the desalinated source water.

Similar results were obtained for the breakthrough of Fe(II) and As during bubble migration after having combined the injection of urban storm water with O_2 and NaOH treatment (Figure 4.10). The more extended ferrihydrite formation associated with the increased pyrite oxidation contributed to a more effective As sequestration. At the same time, the pH was maintained at levels that did not promote the dissolution of Mn-siderite and that did not inhibit an effective sorptive removal of Fe(II) and Mn(II), as happened during the O_2 enrichment

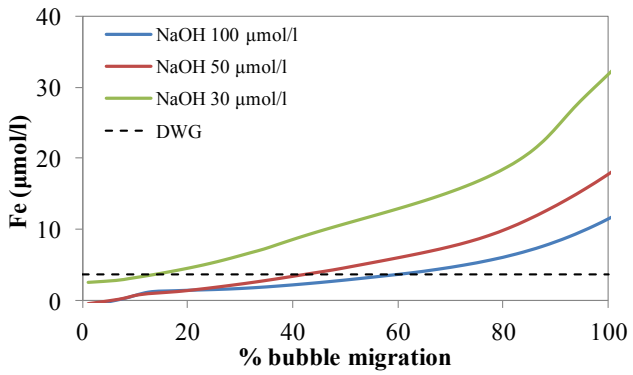

Figure 4.9. Evolution of Fe(II) concentration in the ASR well during a 100% complete bubble migration after having created a 100% efficient buffer zone with desalinated water and NaOH addition. DWG = Drinking Water Guideline.

alone. The Mn(II) concentration (results not shown) improved only slightly (due to its higher pH requirements) and broke through at 70% (455 days) together with the As, whereas the Fe(II) exceeded the drinking water guideline at 64% (416 days) of bubble migration (for a 0.47 mmol/L O_2 and 50 µmol/L NaOH addition). Besides a later breakthrough, the arsenic peak was also dampened and reached a concentration of only 1.4 µmol/L. Accelerating the buffer zone build-up using the NaOH-enriched drinking water had only small positive effects during a subsequent bubble migration (Table 4.5).

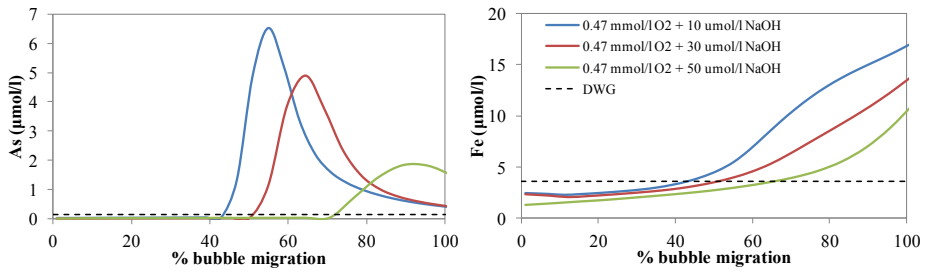

Figure 4.10. Evolution of As and Fe(II) concentrations in the ASR well during a complete bubble migration after having created a 100% efficient buffer zone with urban storm water and O_2 / NaOH addition. DWG = Drinking Water Guideline.

Table 4.5. Summary of tested enrichment techniques for the 3 source water types and the effect of bubble migration.

source water type	efficiency-defining element	dosage tested		% decrease in cycling requirements for 100% efficient buffer zone	bubble migration before water quality deterioration (%)	
		O_2 (mmol/l)	NaOH (µmol/l)		without dosage	with dosage
drinking water	Mn	0	50-100	20-40	40	42-47
desalinated water	Fe	0	30-100	75-94	9	13-59
urban storm water	As	0.47	10-50	60-87	34	47-70

4.3.6 Approach limitations

In our approach, the ASR application has been simplified to a repetition of equal cycles composed of infiltration, storage and recovery, with the recovered volume never exceeding the preceding infiltrated volume. In reality, this is frequently not the case. Years with more and less availability of water to infiltrate will alternate, while contrary fluctuations in the water demand will exert pressure to use parts of the buffer zone. In addition, the ASR cycling frequently cannot be schematized as a steady sequence of infiltration, storage and recovery, because of the fluctuations in the water availability and the demand. For example, recovery may be needed earlier leaving no storage phase, and after recovery it may take months before the next infiltration cycle will start, thus creating an additional storage phase. Such scenarios can be modeled as well, but are beyond the scope of this paper.

As already mentioned, our approach did not consider mixing of water recovered from different aquifer layers in the ASR well. The mixing proportion of different aquifer layers can be calculated when the transmissivity of each screened layer is known. In this case, multiple PHREEQC models are required to simulate the recovered water quality from each layer.

4.4 CONCLUSIONS

The injection of pre-treated drinking water caused Mn(II) exceedances which, however, disappeared after a number of cycles, provided that the recovery would halt as soon as the Mn(II) exceedances would occur. We showed this way how to build an effective buffer zone that would allow a 100% recovery efficiency of the subsequent cycles. The injection of desalinated water caused persisting Fe(II) exceedances which substantially slowed down the creation of an effective buffer zone, whereas the injection of urban storm water caused similar issues with respect to arsenic. The oxygen concentration and the pH of the source water were the key parameters controlling the processes in the storage zone and the quality of the recovered water. It was shown that enriching the source water with O_2 and/or NaOH had major positive effects by accelerating the creation of an efficient buffer zone.

Enriching the desalinated water with 100 µmol/L of NaOH was enough to drastically improve the recovery efficiency and quickly build an effective buffer zone. Similarly, enriching the urban storm water with 0.47 mmol/L of O_2 was enough to inhibit the persisting As concentrations whereas an additional 50 µmol/L NaOH addition quickly suppressed the Fe(II) and Mn(II) concentrations to safe levels.

The effects of bubble migration during a long stand-still phase were studied for the three types of source water. Exceedances of drinking water guidelines with respect to Fe(II) and Mn(II) occurred long before the arrival of the native water and were associated with the slightly acidic pH conditions promoting the dissolution of Mn-carbonate and preventing an efficient sorptive removal. Arsenic exceedances were also associated with inefficient sorptive removal after arsenic was released during pyrite oxidation. Enrichment of the

source water with O_2 and/or NaOH was also helpful in protecting the water quality around the ASR well for a longer time during a bubble migration scenario. Scenario modeling with a calibrated reactive transport model proved to be a useful and practical tool to optimize an ASR system with respect to water quality. The numerical simulations showed that ASR using other types of source water besides drinking water can be viable for the potable water supply, provided of course, that the initial quality of the source water does not exceed any drinking water guidelines.

CHAPTER 5

Aquifer pre-oxidation using permanganate to mitigate water quality deterioration during ASR

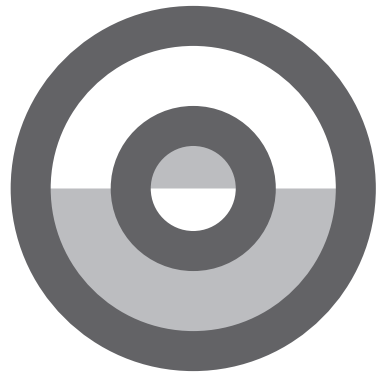

Published as:

Antoniou, E. A., Hartog, N., van Breukelen, B. M. and Stuyfzand, P. J. (2014). “Aquifer pre-oxidation using permanganate to mitigate water quality deterioration during aquifer storage and recovery.” Applied Geochemistry 50(0): 25-36.

ABSTRACT

Water quality deterioration is a common occurrence that may limit the recovery of injected water during aquifer storage and recovery (ASR) operations. This limitation is often induced by the oxidation of the reduced aquifer components by the oxygenated injection water. This study explores the potential of aquifer pre-oxidation using permanganate to improve the quality and volume of the recovered water during ASR. An experimental ASR column setup was developed to simulate the oxygenated water injection and recovery cycles. Undisturbed sediments from an anoxic brackish aquifer at a pilot ASR site were used. A series of 4 conventional ASR cycles injecting oxygenated tap (drinking) water was initially performed. These experimental trials showed a persistent Mn(II) production due to the dissolution of a Mn-containing carbonate that was triggered by pyrite oxidation reactions, as shown by the observed sulfate production. The rise in the Mn(II) concentrations above the drinking water standards would limit the recovery to 15-30% of the injected water without treatment of the recovered water. To a lesser extent, arsenic production resulting from the oxidative dissolution of pyrite posed a water quality threat to the ASR operation. Consequently, a second series of experiments was performed with an oxidation cycle using a dilute (0.02M) potassium permanganate ($KMnO_4$) solution, aimed at deactivating the reactive phases responsible for the acidity-triggered Mn(II) production. This pre-treatment cycle improved the net recovery ratio to 84% during a conventional ASR cycle using oxygenated tap water. The extent of pyrite oxidation was decreased by 63% after the permanganate treatment. The increased competition for oxygen by the adsorbed Fe(II) and Mn(II) on the newly precipitated Mn-oxides combined with the pyrite “deactivation” by removal of the most reactive iron-sulfide crystals during the permanganate flush were primarily responsible for the observed decrease in the pyrite oxidation. The stability of the Mn-oxide precipitates was tested by flushing the columns with native groundwater before performing a final ASR cycle, simulating an increase in the reducing conditions during static periods in the ASR system. The Mn-oxide reduction by ferrous iron in the native groundwater released substantial amounts of Mn(II), which adversely affected the ASR operation in the subsequent cycle. In these cases, repeating the permanganate treatment should be considered.

Keywords: ASR, aquifer storage recovery, aquifer recharge, permanganate treatment, pyrite, manganese, arsenic, column experiments

5.1 INTRODUCTION

Aquifer storage recovery (ASR) is a water resource management tool used to balance the water supply with the demand. During periods of excess water supply, water is injected and stored in an aquifer for subsequent recovery and use in times of water demand (Pyne 2005). ASR can result in water quality improvements, including denitrification, biodegradation of organic micropollutants, such as chlorination byproducts (Pavelic et al. 2005) and pharmaceuticals (Overacre et al. 2006), and removal of pathogens (Page et al. 2010). However, water quality deterioration may also occur during ASR, for example, when oxygenated (surface) water is injected into an anoxic environment containing reactive phases, such as pyrite, carbonates and sedimentary organic material (SOM). The water quality may further deteriorate during an extended storage or recovery phase due to the migration of the stored water or due to the reducing conditions triggered by anaerobic degradation of the organic material (Vanderzalm et al. 2002, Stuyfzand et al. 2005). This process may result, at least during the initial ASR cycles, in elevated concentrations of released Fe(II), Mn(II), arsenic and other trace elements, such as nickel and cobalt (Stuyfzand 1998, Pyne 2003). These elevated concentrations may limit the recovery efficiency of each ASR cycle, defined as the percent recovery by volume (Pyne 2005).

Arsenic release from pyritiferous aquifer material during ASR is problematic at well fields in different parts of the world (Stuyfzand 2001, Mirecki 2004, Price and Pichler 2006, Arthur et al. 2007, Jones and Pichler 2007, Vanderzalm et al. 2007, Stuyfzand and Pyne 2010). Persistent manganese release, typically derived from the dissolution of carbonates, has also been observed during ASR operations (Ibison et al. 1995, Pyne 2005, Stuyfzand et al. 2005b, Pyne et al. 2013). A common aspect of these studies has been that the manganese mobility was influenced by the pH, which controlled the solubility of a Mn-containing siderite. Chronic exposure to manganese in drinking water above the WHO guideline of 7.3 µmol/L may have neurological effects. Concentrations above the aesthetic guideline of 0.91 µmol/L are related to a water color that is black to brown, black staining, and a bitter metallic taste (US-EPA 2009). The removal of Fe(II) and Mn(II) requires further treatment of the recovered water, thus increasing the costs of the ASR system operation. Conventional treatment techniques for the removal of iron and manganese during drinking water production include aeration and rapid sand filtration, occasionally supported by chemical oxidation and sedimentation (Buamah 2009).

To minimize the negative effects of the aquifer reactivity on the water quality, oxygen removal prior to injection has been attempted. Physical removal using a membrane degassing system has been tested in Florida but suffered from high costs and operational issues (Kohn 2009). Catalytic removal of dissolved oxygen from the injected water using a palladium surface and hydrogen gas has not shown long-term reliability (ENTRIX 2009). Pearce and Waldron (2010) have successfully limited arsenic production during ASR by the addition of hydrosulfide ($NaHSO_3$ and NaHS) in the injected water and the chemical removal

of the dissolved oxygen. However, the addition of hydrosulfides resulted in significant iron production during ASR cycle testing, and the system is currently inactive. Moreover, oxygen removal from the injection water is a process that must be repeated prior to every ASR cycle.

Rather than removing oxygen and possibly other electron acceptors (notably NO_3) from the water prior to the ASR injection, extensive pre-oxidation of the aquifer to remove or inactivate the reactive phases might prevent or decrease the water quality deterioration during the ASR operation. This approach is based on evidence that water quality deterioration, especially regarding iron, diminishes with successive cycles (Pyne 2005, Stuyfzand et al. 2005b). In this approach, the injection water is enriched with oxygen or nitrate to accelerate the oxidation of the reactive phases in an aquifer (Chapter 2). A significant pH decline (from 7.6 to 6.7) in the subsequent storage phase due to the increased oxidation reactions caused an enhanced Mn(II) production. The source of Mn(II) is due to the increased carbonate dissolution buffering the induced acidity and due to inadequate sorptive removal. Additionally, even with oxygen-enriched water, a sufficient, therefore, beneficial decrease in the aquifer reactivity may require an impractical amount of treatment cycles.

Aquifer pre-treatment using “stronger” chemical electron acceptors could allow the removal of aquifer reactivity while minimizing the number of treatment cycles required. The use of these electron acceptors has previously been well established in the field of in-situ chemical oxidation (ISCO) to minimize groundwater organic contaminant concentrations (Cavé et al. 2007, Mahmoodlu et al. 2013). Because oxygen can achieve a maximum saturation of 5 times (100% oxygen) compared with air, the use of “strong” electron acceptors for aquifer pre-treatment during ASR allows a significantly greater oxidation capacity per injected water volume, particularly for highly soluble ionic electron acceptors, such as permanganate (MnO_4^-) (Cavé et al. 2007). An additional advantage of permanganate for aquifer pre-treatment is the increase in the sorption capacity through the generation of Mn-oxide precipitates. Mn-oxide precipitates are a by-product of the MnO_4^- reaction with the reduced aquifer phases, such as sedimentary organic matter and pyrite. These precipitates may coat the aquifer minerals and could effectively sequester a range of trace metals, including manganese (Buamah et al. 2009). Finally, the oxidation of the sedimentary electron donors with MnO_4^- consumes protons and increases the pH, thereby buffering the negative side effects related to the lower pH values that occur during aquifer treatment with other electron acceptors, such as oxygen.

The goal of this study is to test the feasibility of the permanganate pre-oxidation to minimize the water quality deterioration during ASR operations using bi-directional ASR column experiments to simulate the evolution of the water quality in an anoxic aquifer. The specific objectives include the following: 1) evaluation of the effect of the aquifer treatment with an aqueous permanganate solution on the water quality and comparing it with the injection of conventional oxygenated (air-saturated) water; 2) evaluation of whether the permanganate treatment of the aquifer sediments improves the recovery efficiency; and 3) evaluation of the water quality development after resaturation with native groundwater, reflecting the situation during static conditions in the ASR system.

5.2 MATERIALS AND METHODS

5.2.1 Aquifer sediments

Anoxic cores (1 m length and 0.1 m diameter) were obtained during the installation of an ASR well in a confined, brackish and anoxic aquifer at 14-41 m below sea level in Nootdorp, the Netherlands, using a reverse-circulation rotary method (Zuurbier et al. 2014). The sediments consist of fine to coarse Pleistocene fluvial sands that contain organic-rich clay lenses. The cores were sealed in PVC liners and stored at 4°C until the following analyses: (1) grain size; (2) organic matter (reactive and bulk); (3) total carbonate content by thermogravimetry (TGA in a CO_2 atmosphere at 330, 550, 1000 °C); (4) total carbon and sulfur using a combustion analyzer (LECO Induction Furnace Instruments); (5) total elemental composition using X-ray fluorescence (XRF). The pyrite content and the reactive iron (non-pyrite) were calculated using the following equations (Griffioen et al. 2012):

- $FeS_2 = 0.5 * S * {M_{FeS_2}}/{M_S}$ (5.1)
- $Fe_{reactive(non-pyrite)} = 2 * {M_{Fe}}/{M_{Fe_2O_3}} * [Fe_2O_3 - (0.225Al_2O_3 - 0.91\%)] - 0.5 * S * {M_{Fe}}/{M_S}$ (5.2)

where M_{FeS_2}, M_S and $M_{Fe_2O_3}$ are the molar masses of FeS_2, S, and Fe_2O_3, respectively. represents the total sulfur content by weight (% dry weight) as measured by the carbon/sulfur combustion analyzer, and Fe_2O_3 and Al_2O_3 represent their content by weight (% d.w.), as determined by XRF. This formula assumes that the silicate-bound Fe_2O_3 amounts to approximately 22.5% of the total Al_2O_3 content and that the total reactive Fe could be regarded as enrichment on top of the silicate-bound Fe (Huisman and Kiden 1997, Dellwig et al. 2001, Griffioen et al. 2012). The cation exchange capacity (CEC) was calculated using the following empirical equation (Stuyfzand et al. 2012)

$$CEC = 5.6 * L + 5.1 * (pH - 1.16) * C_{org} \quad (5.3)$$

where L is the clay fraction obtained from the grain size analyses, and C_{org} is the organic carbon content as measured by TGA. The exchangeable Fe and Mn fractions were further calculated using the PHREEQC model (Parkhurst and Appelo 1999) based on the calculated CEC and the groundwater composition.

The sediment used to pack the columns was obtained from the core at a depth of 28-29 m. The core was obtained from a relatively reactive part of the aquifer, which was expected to have a major influence on the water quality. The water quality deterioration

in these sediments has been previously observed during deep well injection experiments to determine the feasibility of artificial recharge for the drinking water supply (Stuyfzand 1998a). The sediment geochemistry, as averaged by the 5 samples obtained between a depth of 28 and 29 m, is described in Table 5.1.

Table 5.1. Geochemical characteristics of the sediment used in the column experiments.

	Median grain size	Al_2O_3	CaO	Fe_2O_3	MnO	Bulk OM	Carbonates	Clay	FeS_2	Fe_{reac} (non-pyrite)	CEC	Fe_{exch}	Mn_{exch}	As
	µm	(XRF) % d.w.				(LOI 550) % d.w.	(LOI 1000) % d.w.	% d.w.			meq/kg			ppm
Average	498	1.89	0.24	0.40	0.01	0.25	0.34	0.51	0.28	0.49	10.58	0.13	0.02	4
St dev	54	0.15	0.04	0.14	0.005	0.11	0.26	0.39	0.19	0.04	0.94	0.01	0.002	1.4

5.2.2 Water quality

Anoxic, brackish groundwater (Table 5.2) was collected from an observation well situated at a distance of 40 m from the ASR well and screened at a depth of 36 m. The groundwater contained appreciable concentrations of Fe(II) (0.42 mmol/L) and Mn(II) (0.03 mmol/L), whereas the sulfate and arsenic concentrations were negligible. Well purging and in-situ measurements of the dissolved oxygen, electrical conductivity and pH ensured that the water samples were representative of the native groundwater. The groundwater was pumped via a submersible pump into an airtight pressurized (with N_2) tank until it was completely full. Therefore, the anoxic groundwater was maintained for later use to saturate the sediment-packed columns. All of the samples were filtered (using 0.45 µm membrane filters) and acidified with 100 µl HNO_3 65% Suprapur (Merck International, Darmstadt, Germany) for analysis of the cations (Na, K, Ca, Mg, Mn, Fe, S, Si, P, and trace elements) using ICP-OES (Varian 730-ES ICP OES, Agilent Technologies, Santa Clara, CA USA). The anions (F, Cl, NO_2, Br, NO_3, PO_4, and SO_4) were analyzed using the Dionex DX-120 ion chromatograph (Thermo Fisher Scientific Inc., Waltham, MA USA), and the alkalinity was analyzed using the LabMedics Aquakem 250 discrete analyzer (Stockport, UK). All of the samples were cooled to 4 °C after sampling.

Table 5.2. Quality of the native and the injection water used during the experiments.

	pH	EC	T_{lab}	O_2	HCO_3	NH_4	Cl	Na	K	Ca	Mg	Fe	Mn	SO_4	As
		µS/cm	°C	mmol/l										µmol/l	
Native groundwater	6.8	3540	21	<0.01	18.35	0.68	29.30	27.19	0.67	6.79	2.78	0.42	0.03	6.87	0.01
Tap water (air/O_2-enriched)	8	392	21	0.28/0.78	3.85	<0.01	0.25	0.57	0.03	1.74	0.22	<0.01	<0.01	0.95	<0.01
$KMnO_4$ source solution 0.02M	8.4	2400	21	0.28	0.92	<0.01	0.03	0.07	20.00	0.04	<0.01	<0.01	20.02	0.52	0.03

5.2.3 Column setup and the experimental phases

The experimental setup (Figure 5.1) consisted of two serially connected airtight stainless steel columns that accommodated the aquifer sediments. Column 1, with a volume of 324 ml, has a length of 0.3 m and an internal diameter of 3.71 cm. Column 2, with a volume of 2.756 L, has a length of 0.6 m and an internal diameter of 7.65 cm. Both of the columns were preceded by a sampling port and a flow-through cell equipped with sensors for pH (Orbisint CPS11D), electrical conductivity (Condumax CLS21D), dissolved oxygen (Oxymax COS22), and oxidation-reduction potential (ORP) (Orbisint CPS12D, Endress+Hauser AG, Reinach, Switzerland). Two diaphragm-metering pumps (STEPDOS 08, KNF Flodos AG, Sursee, Switzerland) allowed the injection and recovery of the water at a low flow rate (0.39 ml/min). This rate corresponds to a linear velocity of 1.34 m/d, which resulted in a residence time of 5.4 hours in column 1. Stainless steel tubing (1/8”, Swagelok) connected all of the parts of the column-setup. The inner walls of all of the elements, including the columns, flow-through cells, tanks and tubing, were coated with a Teflon layer to avoid contact between the water and the stainless steel. Each column end was closed using 2 caps. The inner cap was comprised of a Teflon ring holding a replaceable sintered-glass filter disk. The filter prevented the transport of the sediment into the connected tubing. The outer cap was constructed of stainless steel and accommodated the outflow port where the tubing was connected.

The anoxic core section was unpacked in a glovebox under a N_2 atmosphere and was mixed carefully before repacking it in the two columns. The compaction was performed in increments using a PVC pestle to reduce the risk of creating preferential flow paths. Once sealed, the columns were weighed and attached to the remainder of the setup. Two experimental series were performed (Table 5.3); thus, the packing procedure was repeated twice. The total porosities (n_{tot}) were deduced from the calculated bulk density (ρ_b) and assuming $\rho_{solid} = \rho_{quartz}$. The total porosities calculated during both of the packing procedures showed a negligible difference (≤ 1.3% deviation). Therefore, the total average porosities were calculated as 0.39 and 0.43 for column 1 and column 2, respectively, and the respective pore volumes were calculated as 126 and 1185 ml. Prior to attaching the columns, the tubing was flushed with N_2 gas to purge the oxygen. After attaching the columns, the entire system was flushed overnight (at 0.5 ml/min) with native groundwater to ensure that both of the columns were fully saturated and the groundwater was in equilibrium with the sediment.

Table 5.3. Cycle characteristics during the 2 experiments. Pore volumes refer to column 1.

Cycle	Injectant	Pore flushes			% recovery	
		Injection	Recovery	Remaining	per cycle (gross)	cumulative (net)
	Experiment 1					
1	air-saturated tap water	9.1	8.7	0.4	96	96
2	air-saturated tap water	3.9	4.3	0	110	100
3	air-saturated tap water	11.9	8.5	3.4	71	63
	Resaturation with native groundwater					
4	O_2-enriched (56 %)	8.9	8.3	0.6	93	93
	Experiment 2					
1	air-saturated tap water	9.3	8.0	1.3 (tap water)	86	86
2	$KMnO_4$ 0.02M	7.1	6.1	1 ($KMnO_4$) + 1.3 (tap water)	86	75
3	air-saturated tap water	8.7	10.2	0.8 (tap water)	117	91
	Resaturation with native groundwater					
4	air-saturated tap water	7.9	9.2	-	114	114

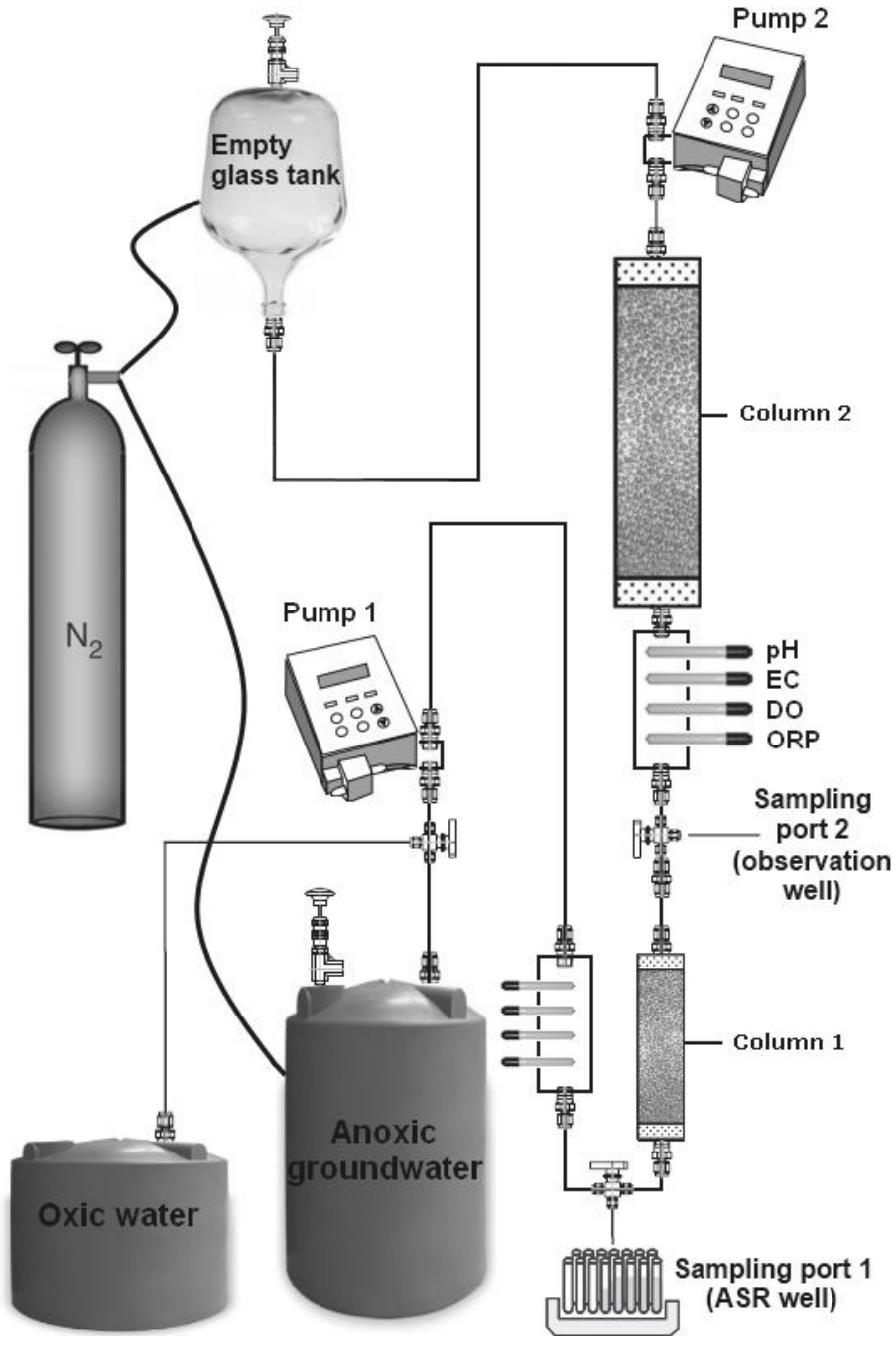

Figure 5.1. ASR column installation.

Injection was simulated by pumping (using pump 1) oxygenated (air-saturated) tap water out of a stainless steel container (Figure 5.1) and injecting it into column 1. The native groundwater was displaced out of column 2 and into an anoxic and slightly pressurized (with N_2) glass tank. A one-way valve allowed the nitrogen to escape to maintain a fixed overpressure while the glass tank filled up with the groundwater from column 2. As the only transparent element in the set-up, the glass tank was covered with aluminum foil to prevent photo-oxidation or other interferences from the light. Recovery was similarly simulated by pumping (using pump 2) all of the water out of the glass tank and injecting it back into column 2. Nitrogen gas was allowed to refill the glass tank to prevent an underpressure and air leakage inside the tank. During injection, port 2 was manually sampled by diverting the flow via a 3-way valve, whereas during recovery, the flow was permanently diverted towards port 1 in which an automatic fraction collector (FOXY 200, Teledyne ISCO, Lincoln, NE USA) obtained samples in predefined volumes and periods. Therefore, port 2 simulated an observation well, and port 1 simulated an ASR well. During recovery, port 2 was not sampled to avoid a discontinuous flow.

The two columns simulated the aquifer flow path as follows: (1) between the ASR well and an observation well and, (2) beyond the observation well, respectively. Column 1 served as the main study column, whereas column 2 functioned as a buffer volume that allowed for the expansion and contraction of the injected pore volumes during the injection and recovery phases. As determined by the electrical conductivity values, the mixing front between the injected water and the groundwater was contained within column 2 during the consecutive cycles, displacing only groundwater into the glass tank.

The first experiment consisted of 3 conventional ASR cycles injecting oxygenated tap water (0.28 mmol/L at 21 ± 2°C) followed by a resaturation of both of the columns with native groundwater and a final cycle in which oxygen-enriched tap water (~0.78 mmol/L) was injected to test the remaining sediment reactivity (Table 5.3). The term “conventional ASR operation” was used to differentiate the ASR cycles in which oxygenated tap water was used during the injection from those involving the injection of a treatment solution.

The second experiment involved the injection of a 0.02 M $KMnO_4$ solution during cycle 2 to treat the sediment (Table 5.2). The effects of this treatment were then evaluated using a third conventional cycle that immediately followed the treatment. A fourth cycle was performed after both of the columns were flushed with abundant native groundwater (9.4 column 1 pore volumes) to simulate the water quality changes after a long period of inactivity at an ASR system or during an extended recovery.

During the ASR operation, the injected water mixes with the groundwater, and the fraction of the recovered groundwater is affected by the recovery of the preceding cycles. Therefore, the gross and net recovery ratios (in percentages) were determined for the different injection-recovery cycles in the two experiments (Table 5.3). These ratios (V/Vi) defined the recovery (V) of the injected volume (Vi) within a cycle and the cumulative recovery of the injectant overall.

5.2.4 Calculation methods

The oxygen consumption in column 1 was determined from the difference in the oxygen concentrations measured by the two dissolved oxygen sensors placed at either end of the column (Figure 5.1). The permanganate consumption was determined by measuring the MnO_4^- concentrations in the samples from port 2 (during injection) and port 1 (during recovery) via UV spectrophotometric analysis of the absorption at 525 nm.

A mass balance approach was applied to quantify and compare the consumption of the electron acceptors that occurred during the two experimental series. The degree of pyrite oxidation was calculated stoichiometrically based on the observed sulfate production (Reactions 1 and 5, Table 5.4). To monitor whether the pyrite reactivity of the sediment in column 1 decreased with consecutive ASR cycles, the sulfate production was monitored at port 2 during the injection phase.

Forward reactive transport modeling was performed to interpret the data and the conclusions derived by the mass balance calculations during the conventional ASR cycles. A 1-D PHREEQC model was developed to simulate a conventional ASR cycle in column 1. The model featured pyrite, calcite, and rhodochrosite as individual phases and the calculated exchanger concentration. The initial theoretical contents of calcite and rhodochrosite were estimated from the CaO/MnO XRF-derived ratio and the total carbonate content, as derived by the TGA (Table 5.1). Ferrihydrite was initially absent, but its formation was allowed to occur following the pyrite oxidation. The native groundwater quality was used as the initial solution.

Table 5.4. Potentially relevant reactions.

Process	Reaction equation	No.
O_2 oxidizing pyrite (buffered)	$4FeS_2 + 15O_2 + 6H_2O + 8CaCO_3 \rightarrow 4Fe(OH)_3 + 8Ca^{2+} + 8SO_4^{2-} + 2CO_2$	1
O_2 oxidizing SOM	$CH_2O + O_2 \rightarrow CO_2 + H_2O$	2
O_2 oxidizing Fe(II) (buffered)	$4Fe^{2+} + O_2 + 4CaCO_3 + 6H_2O \rightarrow 4Fe(OH)_3 + 4Ca^{2+} + 4CO_2$	3
O_2 oxidizing Mn(II) (buffered)	$2Mn^{2+} + O_2 + 2CaCO_3 \rightarrow 2MnO_2 + 2Ca^{2+} + 2CO_2$	4
MnO_4^- oxidizing pyrite	$FeS_2 + 5MnO_4^- + H^+ \rightarrow 5MnO_2 + 2SO_4^{2-} + FeOOH$	5
MnO_4^- oxidizing SOM	$3CH_2O + 4MnO_4^- + 4H^+ \rightarrow 3CO_2 + 4MnO_2 + 5H_2O$	6
MnO_4^- oxidizing Fe(II)	$3Fe^{2+} + MnO_4^- + 7H_2O \rightarrow 3Fe(OH)_3 + MnO_2 + 5H^+$	7
MnO_4^- oxidizing Mn(II)	$3Mn^{2+} + 2MnO_4^- + 2H_2O \rightarrow 5MnO_2 + 4H^+$	8
Fe(II) reducing Mn-oxides	$2Fe^{2+} + MnO_2 + 4H_2O \rightarrow 2Fe(OH)_3 + Mn^{2+} + 2H^+$	9

5.3. RESULTS & DISCUSSION

5.3.1 Sediment geochemistry

Ca-carbonate, Mg-carbonate and Fe/Mn-carbonates were evident in the samples from depths between 27 and 29 m. The TGA of the specific sections revealed various distinct peaks in the close vertical proximity (Figure 5.2). At a depth of 29 m, the presence of Ca-carbonate was confirmed by a characteristic peak at 900 °C, whereas at a depth of 27.5 m, two peaks, at dissociation temperatures of ~690 and 490 °C, indicated the presence of Mg-carbonate and Fe/Mn-carbonates, respectively. The XRF results revealed a certain amount of supplementary reactive iron content, indicating an additional source, such as Fe-hydroxides or Fe-containing carbonates. The XRF results also revealed a low Mn content (0.01 – 0.02%), most likely also contained in the carbonates. Thus, pyrite, organic matter, and Mn/Fe-bearing carbonate are the potential sedimentary electron donors in the sediment used. Whether individual (calcite, siderite, or rhodochrosite) or a mixed carbonate phase (ankerite) existed in the sediment was unclear and would have required additional geochemical analyses, such as X-ray diffraction. However, the presence of mixed phases might complicate the success of this technique.

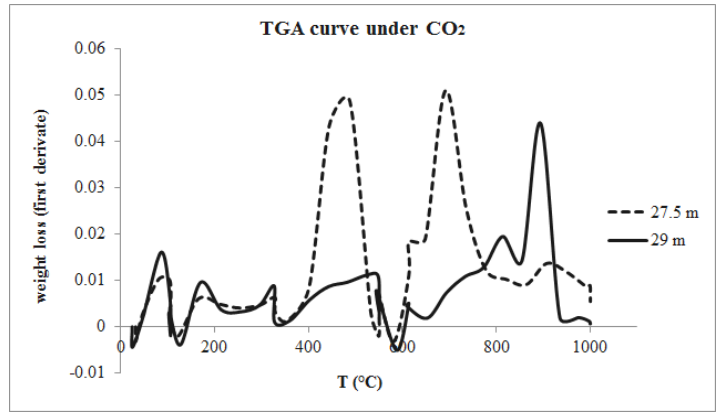

Figure 5.2. TGA results of the two sediment samples obtained at depths of 27.5 and 29 m.

5.3.2 Experimental series 1 - Conventional ASR simulation

Oxygen consumption

The injection of air-saturated water (Table 5.2) into the anoxic sediment column resulted in oxygen-consumption by the aquifer sediments. No dissolved oxygen was detected in the effluent from column 1 during the first 2 injection-recovery cycles. Low oxygen concentrations were detected during cycles 3 (7.4%) and 4 (10.2% of the injected oxygen concentration). The sulfate concentrations measured at port 2 (Figure 5.3) increased during all 4 cycles, suggesting pyrite oxidation by oxygen (Appelo et al. 1998, Prommer and Stuyfzand 2005). The pyrite oxidation accounted for 93% of the total oxygen consumption in cycle 1, whereas all of the oxygen consumption (100% ± 2) was due to pyrite oxidation in cycles 2 and 3. During cycle 4, the sulfate production increased to 0.3 mmol/L, agreeing with the three-fold increase in the oxygen content of the injection water and reflecting an oxygen limitation in the oxidation of pyrite. However, pyrite oxidation accounted for 93% of the oxygen consumption

from the oxygen-enriched injection water (Table 5.5), which was identical to the first cycle. Because the sediment was saturated with native groundwater before cycles 1 and 4, the competition for oxygen in each cycle was likely due to the oxidation of the adsorbed Fe(II) and perhaps, to a certain extent, the Mn(II) on the sedimentary exchange sites. To examine whether the adsorbed Fe(II)/Mn(II) would be sufficient to compete with pyrite for oxygen, the maximum amount of oxygen consumption by the exchangeable/sorbed Fe(II) and Mn(II) was calculated with the PHREEQC model using the native water composition and the calculated cation exchange capacity (CEC) of 10.6 meq/kg sediment (Table 5.1). The calculated reduction capacity of the exchangeable/sorbed Fe(II) and Mn(II) totaled 97 µmol oxygen/L, equivalent to 37% and 12% of the available oxygen in the oxygenated tap water (cycle 1) and in the oxygen-enriched tap water (cycle 4), respectively.

Table 5.5. Electron acceptor consumption and total oxidized pyrite during the two experiments.

Cycle	Oxidant consumption (%)	Relative contribution in oxidant consumption (%)		Total oxidized FeS_2
		FeS_2	Other reductants	% d.w.
Experiment 1				
1	100	93	7	1.3E-04
2	100	100	0	1.5E-04
3	92.6	100	0	1.4E-04
Resaturation with native groundwater				
4 (O_2)	89.8	93	7	3.8E-04
Experiment 2				
1	100	94	6	1.3E-04
2 (MnO_4^-)	51.8	45	55	2.4E-03
3	89.3	55	45	7.4E-05
Resaturation with native groundwater				
4	89.7	45	55	6.4E-05

Other electron donors present in the aquifer, such as sedimentary organic matter and Fe/Mn-carbonates, did not quantifiably contribute to the observed oxygen consumption. However, the oxidation of these phases might gain more importance if the pyrite oxidation rates decrease due to the accumulation of the Fe/Mn-(hydr)oxides on the pyrite surface (Evangelou 1995, Johnson and Hallberg 2005).

Carbonate dissolution

Pyrite oxidation is the primary process responsible for the observed oxygen consumption, whereas the associated proton production will be buffered by the dissolution of the sedimentary carbonates. Carbonate buffering by pure calcite (Reaction 1, Table 5.4) will release equal amounts of sulfate and Ca. However, the calcium concentrations are also affected by cation exchange due to freshening of the sediment during the replacement of the brackish groundwater by the fresh injection water (Appelo 1994) This process affected the initial cation concentrations as observed at port 2 (Figure 5.3) and caused an initial

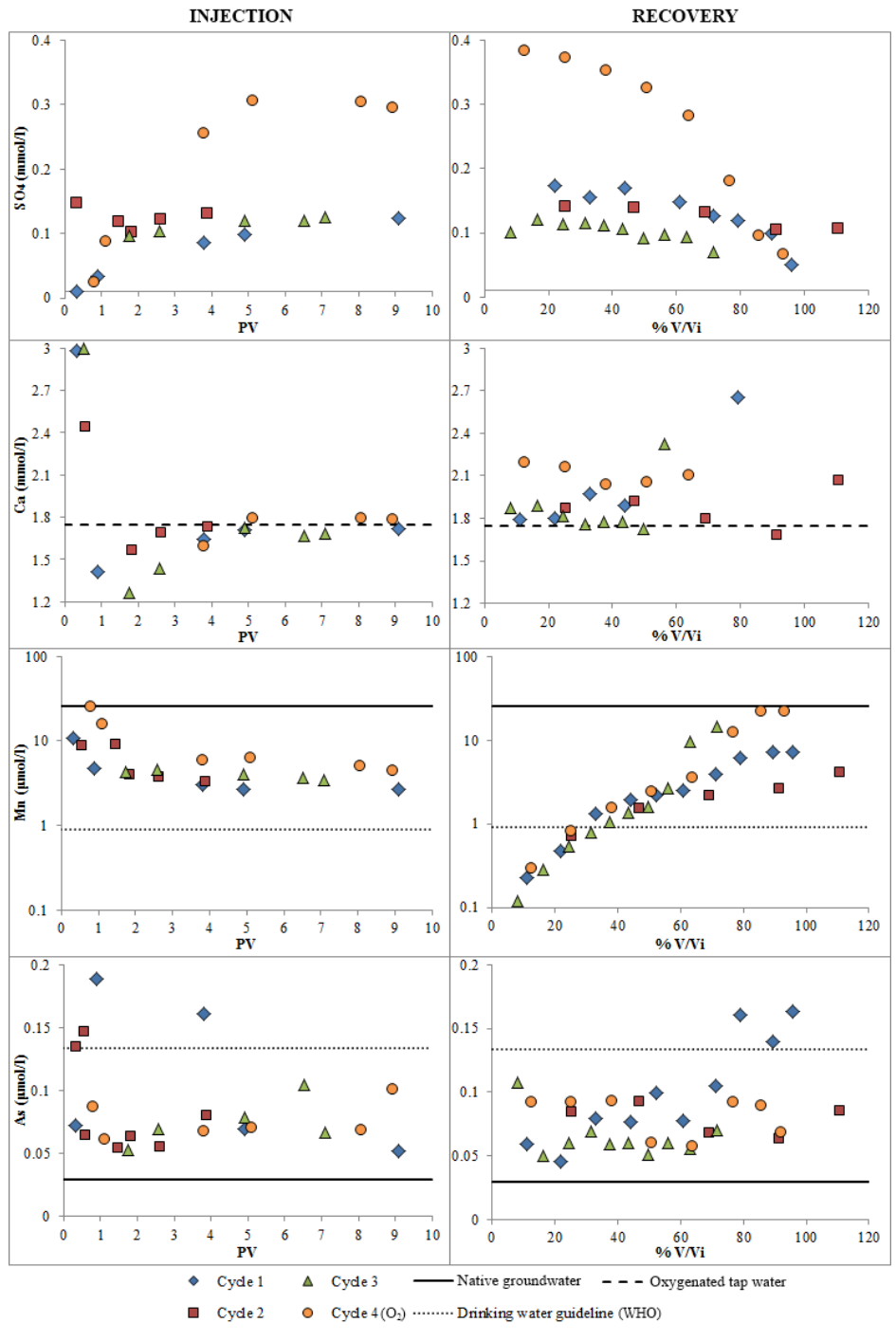

Figure 5.3. Water quality changes during the 4-cycle conventional ASR operation (experiment 1).

decrease in the calcium concentrations below that of the injection water during the flushing of the first four pore volumes. Therefore, the overall Ca and Mg production was measured during each cycle after the influence of the cation exchange (> 6 pore flushes) (Stuyfzand 1998a).

Beyond the influence of the cation exchange, the sulfate production is similar to the Ca production, as expected for proton buffering by a calcite phase. However, the average Ca production was relatively higher by 0.02 mmol/L (Table 5.6), reflecting the buffering of the extra acid production by additional carbonate dissolution, possibly by the partial oxidation of the exchangeable/sorbed Fe(II) and Mn(II) (Reactions 3 and 4, Table 5.4). The Ca production during cycle 2 is more similar to the sulfate production (Table 5.6), supporting that the additional carbonate dissolution during cycle 1, due to the oxidation of the exchangeable/sorbed Fe(II) and Mn(II) that was observed to contribute to the oxygen consumption, is absent in cycles 2 and 3.

Along with the Ca production, a slight increase in the Mg and Mn contents was observed. The ratio of the produced Ca and Mg concentrations during cycles 1 and 4 corresponds to the Ca/Mg ratio (3:1) for the bulk sediment analysis by the XRF, supporting the assumption of a mixed Ca/Mg carbonate. The three times higher Ca and Mg production for cycle 4 reflects the increased proton production by pyrite oxidation due to the three times higher oxygen concentration in that cycle (Table 5.6).

Table 5.6. Average production of sulfate, Ca and Mn during experiment 1.

	Average production		
Cycle	SO_4 (mmol/l)	Ca (mmol/l)	Mn (µmol/l)
1	0.10	0.12	3.3
2	0.12	0.12	3.7
3	0.12	0.11	3.8
4 (O_2)	0.30	0.36	5.4

Observed water quality deterioration: Mn and As production

Because the fresh water was injected to replace the brackish groundwater (Table 5.2), salinization of the recovered water was a clear risk to the recovered water quality. However, before the salinization during recovery yielded chloride concentrations above the drinking water guideline (7 mmol/L), the recovered manganese concentrations and, to a lesser extent, the arsenic concentrations had already compromised the quality of the recovered water. During the first 3 cycles, Mn(II) showed an average production of 3.6 µmol/L, persistent throughout the duration of the injection phase, although the injected water contained no manganese (Figure 5.3). The manganese production surpassed the aesthetic guideline after only 30% of water was recovered. The possible sources of the Mn(II) production are desorption from the exchange complex and dissolution of the existing

Mn-oxides or Mn-containing carbonates. Desorption from the cation exchange sites is inconsistent with the observed persistent manganese production during the consecutive pore flushes. The likely presence of Mn-bearing carbonates was indicated by the TGA of the native sediments (section 5.3.1). Dissolution of the Mn-containing carbonate was the likely origin of the observed Mn(II) production. During the injection of the oxygen-enriched water in cycle 4, a stronger Mn(II) production was observed (5.44 µmol/L, Table 5.6), suggesting that this was also related to the enhanced carbonate dissolution in response to the increased pyrite oxidation, as has been suggested in a previous study following the injection of oxygen-enriched water at an ASR field pilot in Herten, The Netherlands (Chapter 2). However, the increase in the Mn(II) production during the oxygen-enriched cycle in our experiment did not triple, as was observed for sulfate and calcium, suggesting that the produced manganese was further involved in precipitation or adsorption processes. The dissolved iron was not measured, although the TGA and XRF analyses suggested the presence of iron-containing carbonates in the sediment. This result suggests that when Fe(II) was produced (during Fe-carbonate dissolution), it precipitated within a secondary iron phase, such as Fe-hydroxide.

The arsenic concentrations, most likely of pyritic origin (Huisman 1998, Jones and Pichler 2007, Vanderzalm et al. 2007), showed a relatively high initial peak (0.19 µmol/L, Figure 5.3) during injection 1. Compared with the sulfate contents, the arsenic concentrations rapidly decreased to low levels, suggesting their sorption on or incorporation into the freshly precipitated iron hydroxides (Stuyfzand 2001, Buamah 2009, Van Halem 2011) that resulted from the pyrite oxidation. Similarly, arsenic posed a concern during recovery 1, surpassing the drinking water guideline of 0.13 µmol/L after having recovered 75% of the injected water and indicating the possible instability of the Fe-hydroxide precipitates (Vanderzalm et al. 2007). However, the arsenic production decreased in the subsequent cycles to below 0.1 µmol/L, indicating an increased sequestration efficiency. Production of other pyrite-associated trace elements, such as Co, Ni and Zn (Zhang et al. 2009), was not observed in this experiment.

5.3.3 Experimental series 2 – effect of the MnO_4^- pre-treatment on the recovered water quality

In the second experimental series, the effects of the aquifer treatment with permanganate are presented. To enable a comparison with the first experimental series, the first cycle was initiated with the injection of the same oxygenated tap water into the fresh aquifer sediment containing brackish native groundwater. The reactions that occurred and the associated water quality changes were similar (Figures 5.3 and 5.4, Table 5.5).

Cycle 2: Permanganate Treatment

During cycle 2, a 0.02 M $KMnO_4$ solution was injected instead of the normal oxygenated tap water (Table 5.2). The MnO_4^- solution represented an electron acceptor load 57 times greater than the oxygenated tap water based on the electron acceptance capacity/L. The strong oxidizing effects were reflected by significant increases in the sulfate concentration

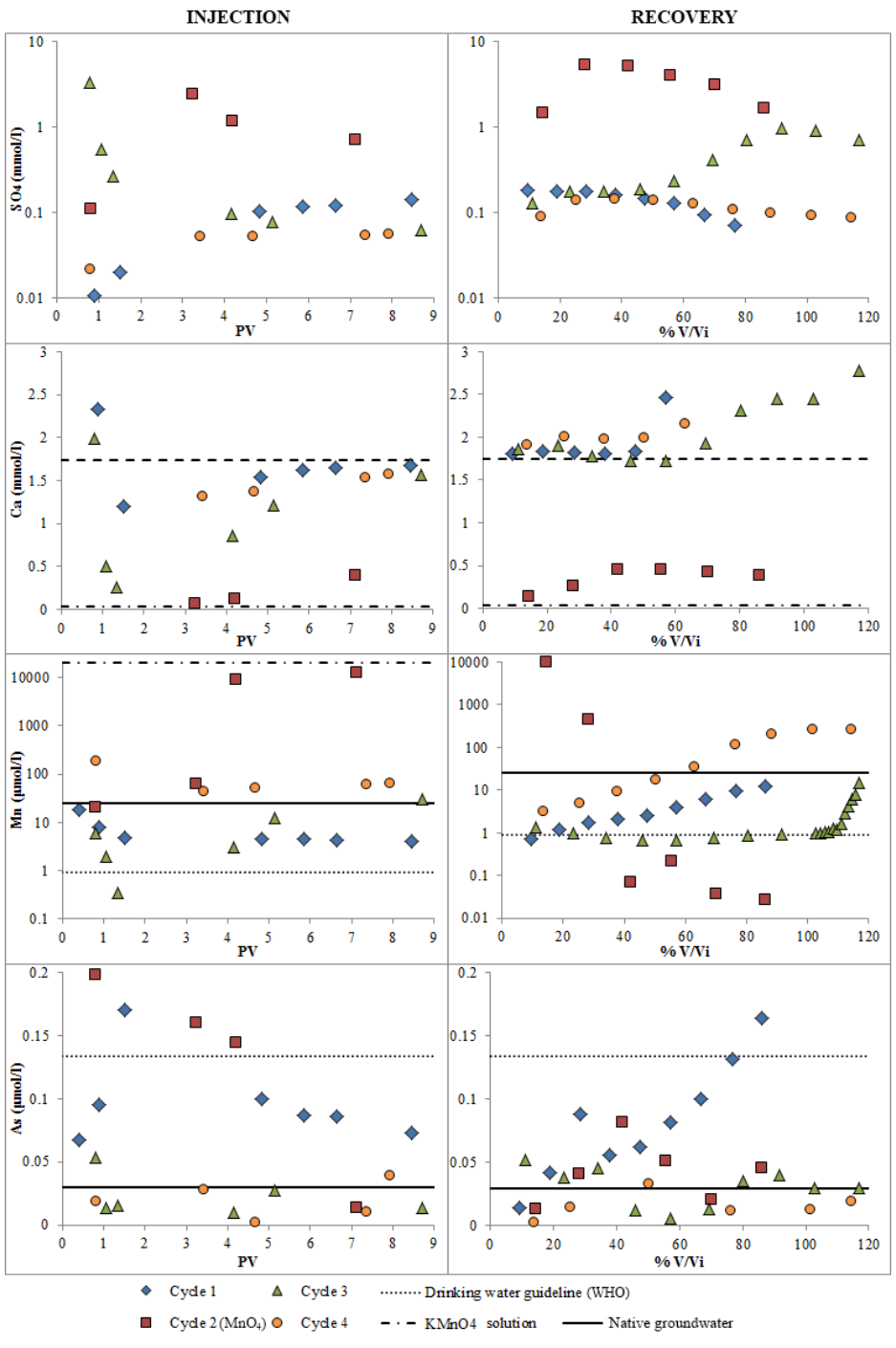

Figure 5.4. Water quality changes during the permanganate treatment experiment (experiment 2).

(2.43 mmol/L) and the alkalinity, as measured at port 2 (Figures 5.5 and 5.6). The initial sulfate production decreased over time, indicating a decrease in the extent of the pyrite oxidation. The total amount of sulfate produced accounted only for a small calculated fraction (0.85%) of the pyrite present in the sediment. Therefore, the decrease in the sulfate concentration was due to the progressive depletion of the most reactive pyrite surfaces or due to coating effects.

The permanganate concentration during the injection, as measured at port 2, increased from 5.2 to 13.6 mmol/L between the 3.2 and 4.2 pore volumes, respectively, approaching the concentration of the injected solution (Figure 5.5). This result indicated that during the first 3 pore flushes, most of the MnO_4^- precipitated as Mn oxide. Although the sulfate production increased 20 times compared with the first cycle, the pyrite oxidation could only account for 45% (or 4.7 mmol MnO_4^-/L) of the measured total MnO_4^- consumption. Consistent with the proton consuming stoichiometry of the oxidation of pyrite by permanganate, the pH values initially increased to 9.5, after which they started to decrease concurrently with the decrease in the sulfate concentrations (Figure 5.6). However, throughout the cycle, the observed pH values were at or above the pH of the injected permanganate solution (8.4) at both of the sampling ports. According to Reaction 6 (Table 5.4), during the oxidation of the organic matter, the pH increase due to proton consumption is mitigated by the production of weakly acidic CO_2. Therefore, the organic matter oxidation was likely the primary contributor to the remaining 55% of the observed permanganate consumption. The low adsorbed Fe(II) and Mn(II) concentrations were expected to contribute minimally (<1%) to the overall observed permanganate consumption.

During the injection of the permanganate solution, oxygen was measured in the effluent at port 2 after 3 pore volumes and reached a concentration of 0.07 mmol/L (25%) by the end of the injection. This result suggests that the permanganate treatment resulted in a pronounced reduction in reactivity towards oxygen compared with cycle 1 in which all of the oxygen introduced was still consumed in the column. Even during the oxygen-enriched fourth cycle in the first experimental series, a maximum of 10.2% of the injected oxygen concentration was detected in the effluent.

In addition to the reactive sulfides, SOM was also significantly consumed during the permanganate flush. The contribution of the SOM to the MnO_4^- consumption decreased during recovery, allowing the reactive sulfides to consume the remaining permanganate more exclusively, as indicated by the increased sulfate concentrations during the first stages of recovery (Figure 5.5). These maximum sulfate concentrations were 88% of the stoichiometric value expected based on Reaction 5 in Table 5.4. The sulfate concentrations decreased as the mixed dispersion front with the groundwater arrived. Apart from the first two samples during recovery (< 30% V/Vi), which showed high total manganese levels due to the remaining MnO_4^-, Mn was present in very low concentrations (< 0.2 µmol/L) throughout the remaining part of recovery (Figure 5.4).

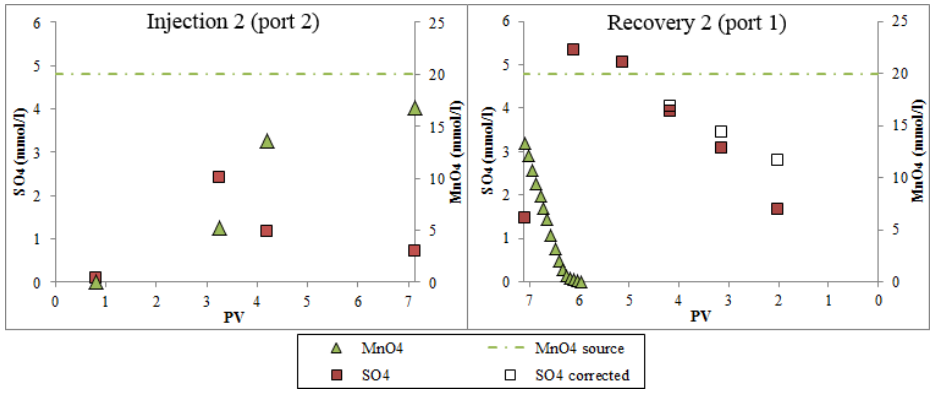

Figure 5.5. Sulfate and permanganate behavior as observed during the injection (at port 2) and during the recovery (at port 1) of the treatment cycle (cycle 2). X axes was reversed during the recovery (after correcting for the pore volume between the two observation ports) in order to match the injected pore volumes and make them comparable. The recovered sulfate concentrations were corrected for the dispersive mixing with the groundwater (sulfate corrected).

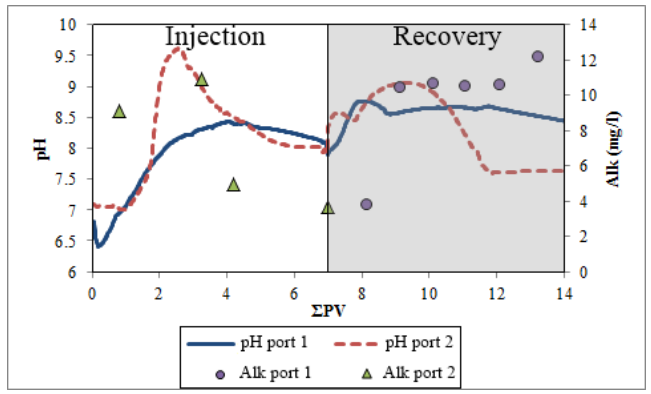

Figure 5.6. Alkalinity and pH behavior during the treatment cycle (cycle 2) of experiment 2.

Cycle 3: Conventional ASR cycle after the permanganate treatment

Cycle 3 started directly after the final recovery of cycle 2, with the injection of oxygenated tap water, as in cycle 1. Oxygen was detected in the effluent at port 2 after less than 3 pore flushes and reached a concentration of 0.09 mmol/L (32%) by the end of the injection phase. In addition to the initial pore flushes containing a portion of the sulfate from the previous cycle, the sulfate production stabilized at ~0.06 mmol/L by the end of the injection, a reduction of 57% compared with the first cycle.

An average Ca production of 0.23 mmol/L was measured, indicating a higher calcium/sulfate ratio compared with cycle 1. This result combined with the decreased pyrite contribution to the oxygen consumption (55%) compared with cycle 1 (94%, Table 5.5) indicated that

the adsorbed Fe(II) and Mn(II) acquired a major role as electron donors and caused an increased competition for oxygen consumption. After permanganate reacted with the SOM, it is unlikely that the organic matter oxidation by oxygen suddenly became as competitive as the pyrite oxidation. However, during recovery 2, the dissolved Fe(II) and Mn(II) from the native groundwater were expected to sorb on the Mn-oxides formed during the permanganate flush. Oxidation of these elements, now catalyzed by the Mn-oxides (Stumm and Morgan 1996, Scot 2005) is expected to cause an increased competition for oxygen consumption, impeding the oxidation of pyrite and producing the additionally observed Ca (Reactions 3 and 4, Table 5.4). Oxygen in the effluent at port 2 indicated complete oxidation of the adsorbed Fe(II) and Mn(II) fractions. The extent of pyrite oxidation was lower compared with that prior to the permanganate treatment. This result supports the conclusion that a significant portion of the oxidizing sulfides was removed or coated during the permanganate flush.

The Mn concentrations during recovery remained below the drinking water guideline (0.91 µmol/L) until achieving a recovery ratio of 110% (or a net recovery ratio of 84%, Table 3). Then, the Mn concentration increased to 14.5 µmol/L after recovering 17% more water compared with the injected volume (Table 5.3, Figure 5.4). This high recovery ratio with respect to Mn(II) suggested an effective removal of the dissolved Mn(II) by sorption to the Mn-oxides formed during the treatment cycle (Reactions 5-8, Table 5.4). The removal continued until the sorption capacity of the MnO_2 precipitates was saturated with the groundwater composition. Additionally, the Mn(II) adsorption capacity of the precipitates was expected to decrease as the pH values gradually decreased towards the native groundwater level, reflecting the pH sensitivity of the exchange sites at the MnO_2 surface (Buamah 2009).

Cycle 4: After resaturation with the native groundwater

Following cycle 3, the columns were abundantly flushed and resaturated with the native groundwater. The injection of oxygenated tap water during cycle 4 resulted in a steady sulfate production of ~0.05 mmol/L, 63% lower than in cycle 1, and slightly less than cycle 3 (Figure 5.4). Oxygen was detected in the effluent from column 1 after 6 pore flushes and reached a concentration of 0.06 mmol/L (21%) by the end of the injection. Therefore, more oxygen consumption was observed in cycle 4, whereas the relative contribution of pyrite decreased to 45% (Table 5.5). This result suggested an even greater contribution of heterogeneous Fe(II) and Mn(II) oxidation. The average net Ca production (0.33 mmol/L) and the calcium/sulfate production ratio increased significantly compared with cycle 3, confirming that the heterogeneous oxidation of the adsorbed Fe(II) and Mn(II) acquired a leading role in the oxygen consumption and further impeded the pyrite oxidation.

Increased and persistent manganese production (~0.06 mmol/L) occurred throughout the injection phase of cycle 4, suggesting the cation exchange between the injected/produced Ca and the exchangeable Mn(II). The exchanging Mn(II) concentrations derived from the native groundwater flush could not have exceeded 0.03 mmol/L (Table 5.2), indicating that the remaining exchangeable concentration was derived from another source. The partial

MnO_2 reduction triggered by Fe(II), as has been described in detail by Postma and Appelo (2000), might have occurred during the native groundwater flush. Considering this possibility, 0.42 mmol/L of Fe(II) in the native groundwater can reduce 0.21 mmol/L of the previously formed Mn(IV)-oxides, releasing an equal amount of Mn(II) (Reaction 9, Table 5.4). A Mn(II) concentration of 0.2 mmol/L was measured at port 2 after injecting 0.8 pore volumes of the oxygenated tap water (Figure 5.4), consistent with the production of Mn(II) during the Mn-oxide reduction by Fe(II) due to the preceding flush with the native groundwater. The released Mn(II) was expected to load the sorption sites on the MnO_2 to subsequently exchange (with Ca) or oxidize (heterogeneously) in the following injection during cycle 4.

During the recovery phase in cycle 4, the abstracted Mn(II) concentrations immediately exceeded the drinking water guide levels. The concentrations continued to rise towards a stable level, which reflected the Mn(II) concentration expected for the reductive Mn-oxide dissolution by Fe(II) derived from the native groundwater flush prior to cycle 4 (Figure 5.4).

5.3.4 Reactive transport modeling

The water quality observed at port 2 (during injection) and port 1 (during recovery) was satisfactorily reproduced during a conventional ASR cycle (Figure 5.7). The model simulated the exchange processes and the mineral behavior along column 1 (Figure 5.8). According to the model, Ca and, initially, Mg displaced Na and K from the exchanger, whereas Mg is later also displaced by Ca. The model provided additional insight into the carbonate behavior along the column during the injection. Calcite supersaturation due to the high Ca levels might have caused precipitation of the mineral along the first half of the column, whereas the expected dissolution, triggered by the pyrite oxidation, occurred in the second half (Figure 5.8). Rhodochrosite dissolved along the entire column causing the persistent Mn(II) production observed at port 2. We conclude that the PHREEQC model supported the conclusions derived by the observations and reinforced the mass balance calculations and the reactions chosen.

5.3.5 Efficiency of the treatment

The goal of permanganate treatment was to limit the As and Mn(II) production. Arsenic removal was observed even without treatment during the consecutive cycles of experimental series 1. Lower As concentrations were measured after the permanganate treatment, indicating that aquifers with persistent As regulatory exceedances might benefit from this treatment technique. Based on the recovered Mn(II) concentrations, the permanganate treatment resulted in an increase from 15% recovery before treatment to 85% (net) recovery after treatment in cycle 3. However, the increased recovery ratio regarding Mn(II) in our case, could be prohibitive with respect to other elements. For example, the chloride levels would prevent, for this particular brackish aquifer setting, a recovery ratio higher than 65% (results not shown) from a drinking water perspective. Buoyancy effects would further complicate the stability of the stored water, consequently affecting the recovery ratio regarding chloride, as has been observed by Zuurbier et al. (2014) for the same site.

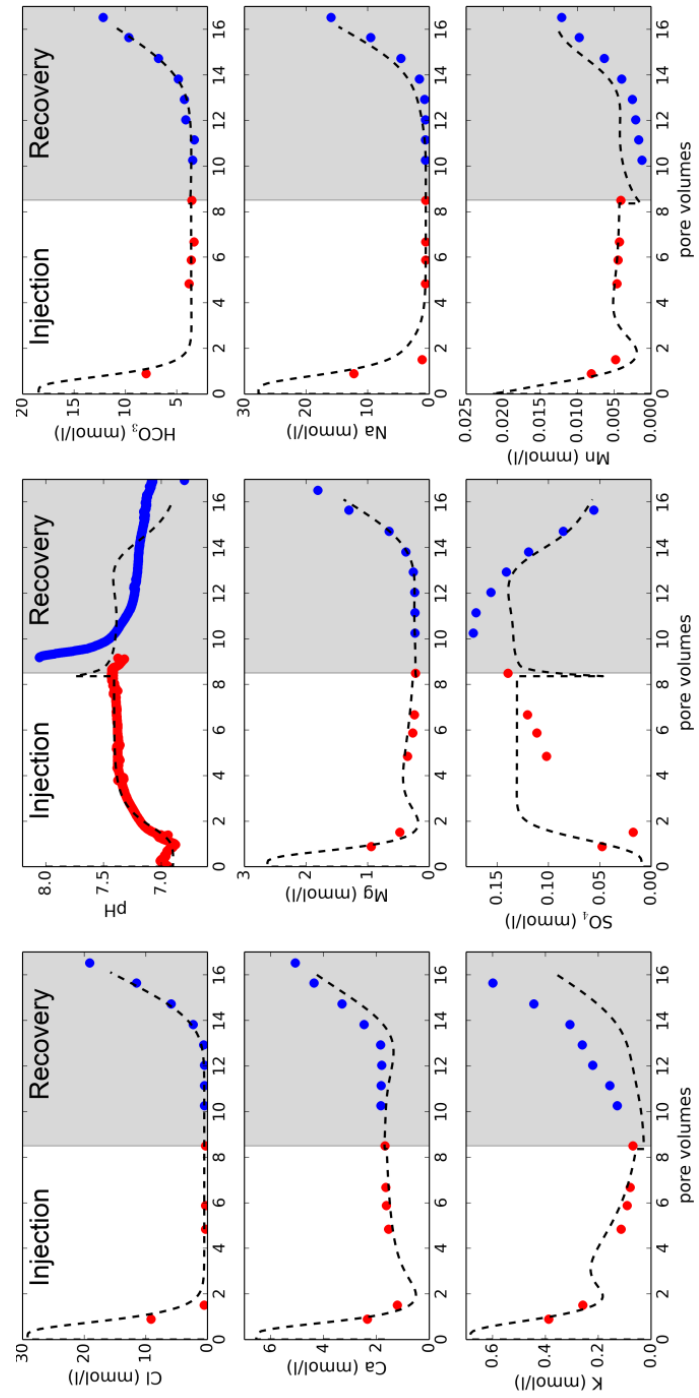

Figure 5.7. Model output and observations measured at port 2 during injection (red dots) and at port 1 during recovery (blue dots) during a conventional ASR cycle (cycle 1 – experiment 2).

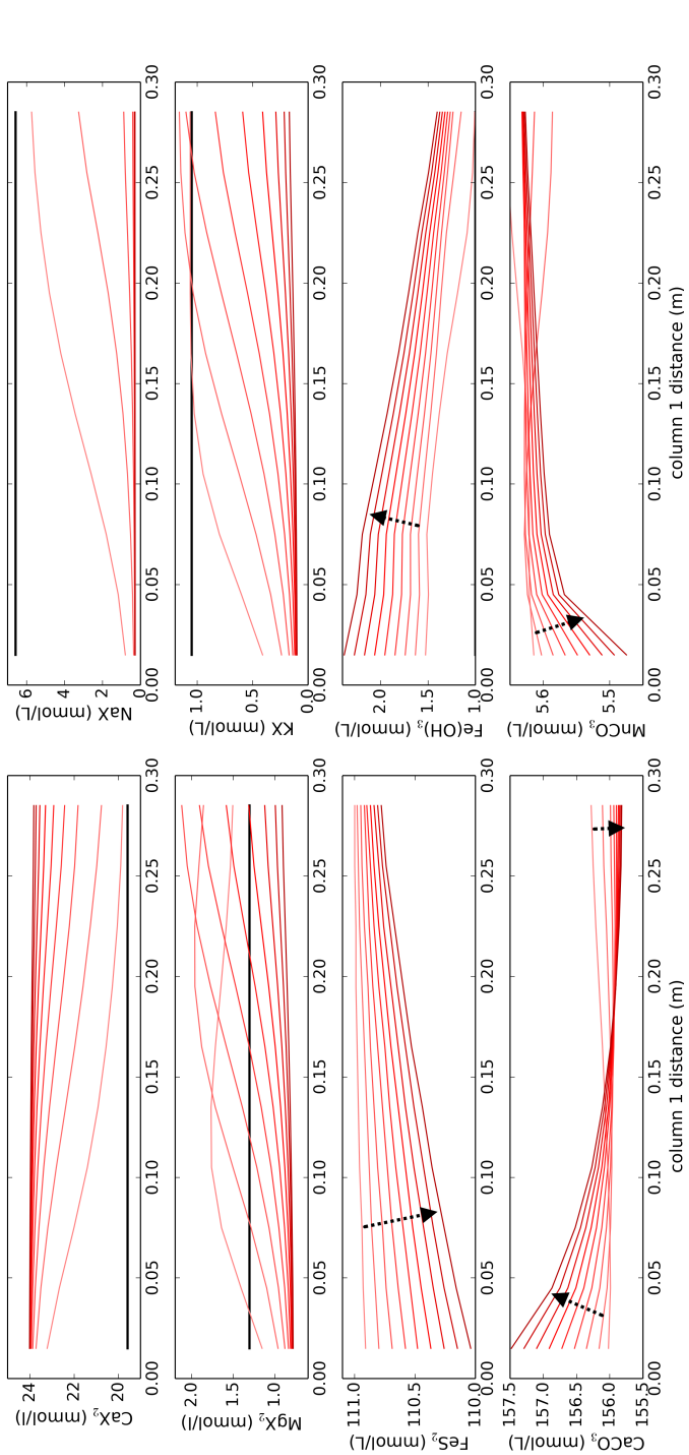

Figure 5.8. Modeled spatial distribution of exchanger and mineral concentrations along column 1 during a conventional ASR cycle (injection 1 - experiment 2). Black lines indicate the initial conditions while red lines (from light to dark) indicate the evolution during the 9.3 pore flushes. Arrows help visualizing the evolution.

The extended precipitation of Mn-oxides due to the permanganate treatment may result in clogging issues during the following ASR cycles. The pump operation and the pressure meters did not show any signs of clogging during the experiments. However, clogging could be an issue during the field-scale operation. Future studies aiming at upscaling this technique should address these potential issues.

The permanganate solution, depending on its purity, might introduce certain trace elements in the aquifer. The solution introduced in the columns, even at a 20 times dilution of a concentrated $KMnO_4$ solution, introduced trace concentrations of Al, Ag, Co, Cr, Ni, Pb, and Se that were above the native water concentration and, in certain cases (Cr, Ni, Pb, Se), above the drinking water guidelines (Table 5.7) as defined by the WHO (2011a). Although they were detected in the effluent at port 2 during the treatment cycle, these trace concentrations were not encountered in the recovered water from port 1 (Table 5.7), even during cycle 4, which followed the Fe(II)-induced reduction of the Mn-oxide precipitates. The recovered concentrations were even lower, confirming their efficient sorptive removal by the remaining Mn-oxides. In any case, during a field ASR application, a treatment solution can be diluted for regulatory compliance.

Table 5.7. Introduced trace elements with the permanganate solution that were above the native concentration or above the drinking water guideline (DWG). "Recovered" defines the maximum concentration measured in port 1 during the recovery phase of cycle 4.

Element	$KMnO_4$ solution	Native	DWG	Recovered
		µmol/l		
Al	1.44	0.07	7.41	0.96
Ag	0.60	<0.01	0.93	0.01
Co	0.52	0.04	-	0.06
Cr	2.86	0.08	0.96	0.03
Ni	0.65	0.05	0.34	0.19
Pb	0.50	0.03	0.05	0.04
Se	7.67	0.04	0.13	0.09

The elevated potassium and sulfate levels resulting from the $KMnO_4$ treatment solution and the pyrite oxidation were also recorded in the recovered water, which should be considered non-potable. However, once the injected treatment volume has been fully recovered, normal ASR cycling can be re-applied in a more stable aquifer setting, characterized by less reactive phases and highly sorptive surfaces able to efficiently scavenge the incoming Mn(II) and As. Whether this treatment would prove economical depends on the treatment costs, including the frequency with which it would have to be re-applied. Currently, the bulk price of potassium permanganate is 2-5 USD/kg, depending on the quantity ordered, resulting in a price of 6-16 cents/L for the 0.02 M solution used in our experiments.

Regarding the longevity of the beneficial effect of the permanganate treatment, it is expected that if the recovery ratio remains below 100%, then the Mn-oxides will continue

to scavenge the Mn(II) by adsorption aided by catalytic oxidation (Buamah et al. 2009). The entire process will possibly self-enhance, as occurs with consecutive cycles during the application of subsurface iron removal (Van Beek 1983, Rott and Friedle 1985, Appelo et al. 1999). If the ASR recovery ratios do not exceed 100%, then the dissolved native Fe(II) will not approach and reduce the Mn oxide precipitates.

In practice, ASR operations might undergo intentional or circumstantial downtime, which depending on the length of the downtime and the local groundwater flow conditions, might result in a substantial inflow of the native groundwater into the ASR storage zone. During a long static phase, the Mn (and Fe)-oxides may also be used as electron-acceptors for the mineralization of the biomass around the ASR well, also releasing high Mn(II) concentrations in the groundwater (Vanderzalm et al. 2006, Stuyfzand et al. 2005b). In these cases, the repetition of the permanganate treatment cycles might be periodically required. Generally, the permanganate treatment is recommended during the first or second (if an initial screening cycle is desired) ASR cycle so that the plant can immediately benefit from the treatment.

In conclusion, following the permanganate treatment, the Mn(II) production may increase, showing a persistent production during the injection phase of the subsequent cycles. This production is a result of the native Mn(II) that sorbed on the new exchange sites during the recovery of the permanganate solution and that, during the following injection, exchanges with the injected/produced Ca. This concentration cannot exceed the native levels (typically < 0.04 mmol/L; Buamah 2009) unless reduction of the newly formed Mn-oxides occurs. The high native Fe(II) concentrations, in our case, constitute a worst-case scenario regarding the Mn-oxide reduction and the resulting Mn(II) production. Despite the unavoidable Mn(II) production during injection, if care is taken as to avoid Mn-oxide reduction by an undesirable inflow of the native groundwater, no Mn(II) is expected to be detected in the recovered ASR water. Based on these conclusions, the permanganate treatment could be a viable option at the Nootdorp site for drinking water ASR applications.

5.3.6 Limitations of the laboratory assessment

This experimental setup simulated a one-dimensional flow along a flow path extending away from the ASR well. This simulation posed, as expected, certain limitations compared with a field ASR application. The most important limitation is that the aquifer heterogeneity effects were not considered in these experiments. Preferential flowpaths were not present in these carefully homogenized sediments. The inflow of the native groundwater, which is responsible for the observed reduction of the newly formed Mn-oxides, may even result during recovery if preferential flow paths are present. Homogenizing the sediment might have increased the overall reactivity inside the column as opposed to a field situation in which the reactive material is typically clustered into fine-grained lenses that may not transmit the majority of flow. These issues should be considered when this technique is to be applied in a field ASR application.

5.4. CONCLUSIONS

Column experiments simulating the ASR cycles in which oxygenated tap water was injected into a brackish and anoxic “aquifer” setting were performed. The primary observed processes were cation exchange due to freshening of the sediment, oxidation of pyrite, and carbonate dissolution, whereas oxidation of the adsorbed/exchangeable Fe(II) and Mn(II) was deduced by the pyrite oxidation and the oxygen consumption patterns. Carbonate dissolution was directly related to the magnitude of the oxidation reactions and resulted from proton production. The Mn(II) production, resulting from carbonate dissolution, did not show any decrease in time or with consecutive cycles. To neutralize the Mn production, which persistently compromised the recovered water quality after having recovered 15% of the injected water, the aquifer sediment was treated with a 0.02 M potassium permanganate ($KMnO_4$) solution. The extended oxidation reactions with organic matter and pyrite caused partial depletion and coating of their reactive surfaces (reactive organic matter and readily oxidizable iron-sulfides) along with an extensive precipitation of Mn-oxides. During the following ASR cycle, these precipitates allowed a recovery ratio of 110% (a net recovery ratio of 84%) before encountering prohibitive Mn(II) concentrations at port 1.

The amount of pyrite oxidized and its relative contribution to the electron acceptor consumption by other electron donors (SOM and adsorbed Fe(II)/Mn(II)) were quantified following a mass balance approach. No decrease in the pyrite reactivity was observed during the 4-cycle conventional ASR experiments, whereas the pyrite oxidation decreased by 63% after the permanganate treatment. The increased competition for oxygen consumption of the adsorbed Fe(II) and Mn(II) on the newly precipitated Mn-oxides was responsible for this decrease, possibly in combination with a pyrite “deactivation” by removal and coating of the most reactive iron-sulfide crystals during the permanganate flush. The decrease in the pyrite oxidation resulted in a suppressed As production, which initially compromised the recovered water quality after recovering 75% of the injected water. Although permanganate was not necessary for the As removal in our case, the MnO_4^- treatment further lowered the As concentrations, indicating that aquifers with persistent As problems might benefit from this treatment technique. Although Mn(II) is produced during the injection phase, even after treatment, the abundant accumulation of the Mn-oxides allowed for an efficient Mn(II) sorption during recovery. We conclude that the sediment in column 1 was more suitable for ASR after the permanganate treatment.

The abundant resaturation of the permanganate-treated columns with the native groundwater, simulating a potential scenario during operational ASR downtime or an extended recovery resulted in a substantial reduction in the previously formed Mn-oxides by the release of high Mn(II) concentrations from ferrous iron in the groundwater. During the subsequent recovery cycle, these Mn(II) concentrations were not successfully sequestered due to the absence of sufficient Mn-oxides, resulting in adverse effects on the recovered water quality. Therefore, care should be taken to avoid this situation; otherwise, a repetition of the permanganate treatment might be required.

CHAPTER 6
Synthesis

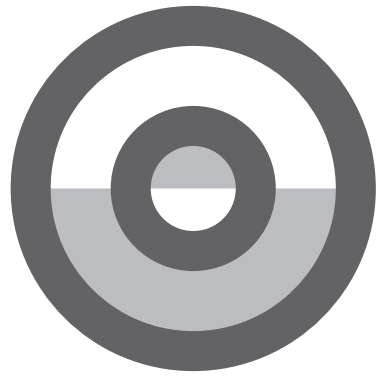

6.1 SUMMARY AND CONCLUSIONS

Based on the current knowledge gaps described in the introductory chapter, three key research objectives were defined:

1. Acquiring an improved insight in hydrogeochemical patterns and processes and water quality improvements through long term monitoring of a drinking water ASR pilot and through lab experiments with an innovative column setup (combined with modeling).
2. Improving ASR operation with optional treatments (O_2, NaOH, permanganate) as investigated in the field, with column experiments, and with reactive transport modeling.
3. Assessing and optimizing ASR performance through reactive transport modeling alone, by evaluation of variations in operational aspects (different source water compositions, implementation of a buffer zone, and bubble migration during a prolonged storage phase).

In order to realize these goals, we evaluated the extensive monitoring data of a 9-year ASR pilot at well field Herten of Water Utility WML, we constructed a novel column set-up for simulating flow reversals during ASR application, and we implemented a 1D reactive transport model capable of simulating and predicting the evolution of water quality along flowlines, representing different aquifer layers.

The focus in this study was exclusively on fresh water aquifers, ASR application for supply of water meeting drinking water standards, and on the inorganic chemistry. This excludes the complications due to upward bubble migration (buoyancy effects) driven by density differences, includes subtle problems with sometimes minor Fe, Mn and As exceedances of drinking water standards, and justifies not to deal with a large group of pollutants which are usually addressed when injecting surface water with a limited pretreatment.

Patterns and processes

With respect to the first research objective, both real-scale and lab-scale observations pointed to the fact that during ASR, the water quality is mainly altered by oxygen consumption by pyrite, sedimentary organic matter, and exchangeable Fe(II), NH_4^+, and Mn(II), and, if present, by the subsequent dissolution of carbonate minerals (calcite, siderite, ankerite), as testified by the increasing TIC during storage phases. If injection is performed in a brackish aquifer, cation exchange between Ca, Mg, Na, and K will cause major changes in the concentrations of these cations, possibly masking carbonate dissolution processes, as observed during the column experiments. Both field and lab results indicated that carbonate dissolution was directly related to the magnitude of oxidation reactions, as concluded after enriching the source water with O_2.

Carbonate dissolution reactions as well as desorption from Fe-hydroxides released Fe(II) and Mn(II) in the water during recovery phases. This behavior was observed during the column experiments and was verified by reactive transport simulations of the Herten aquifer. Fe(II) and partly Mn(II) removal during recovery was demonstrated by particle tracking between the 3 observation wells in Herten and pointed to sorption on neoformed ferrihydrite. The model suggested an increasing sorption capacity due to a gradual build-up of Fe-hydroxide precipitates resulting from prolonged injection phases. Modeled Fe(II) suggested a long term subsurface removal, while Mn(II) showed a tendency to easily desorb. Eventually, Mn(II) removal was insufficient during both the Herten pilot and the column experiments hindering the smooth operation of ASR. The frequent Mn drinking water standard exceedances (0.05 mg/L), in combination with expected treatment difficulties and high costs convinced water utility WML in 2009 to abandon the idea of ASR application in the Herten aquifer. An eventual drinking water ASR application in the Nootdorp aquifer, from which the column sediments derived, would have had a similar fate.

The leaching progress of reactive minerals in two aquifer layers (layers A and D), a natural process promoted by subsequent pore volumes and ASR cycles, was quantified using a mass balance approach. In layer A, where initial mineral contents were lower and flow velocities higher, we calculated a full depletion of pyrite and calcite in the proximal observation well (8 m) but not in the more distant one (25 m) implying that the leaching front is now situated somewhere in-between. In layer D, on the other hand, complete leaching was not identified. The pyrite leaching fronts and the Fe-hydroxide precipitation fronts were simulated in the two aquifer layers during the 14 ASR cycles. The results confirmed that a higher permeability, as in layer A, in combination with the low pyrite content caused more extended pyrite depletion. Shorter travel times translate into a higher oxygen flux implying higher oxidation rates.

The mobilization of Fe(II), SO_4, As, Co, Ni and partly of Mn(II), was observed to decline during consecutive cycles in the Herten ASR pilot. Leaching of pyrite's reactive crystals and their coating with reaction products were considered responsible for the gradually decreasing mobilization of these elements. Mn(II) mobilization deriving from acidity-driven carbonate dissolution (Mn-siderite) is also expected to decrease with the decline of oxidation reactions. Contrary to the field observations, no decrease in SO_4 and Mn(II) mobilization was observed during the column experiments. This was clearly due to the small number of cycles (4) in combination with a much higher pyrite content of the cored aquifer sand from Nootdorp. Since no decrease in oxidation reactions was observed, carbonate dissolution and therefore Mn(II) mobilization did not decrease either.

Treatment options

With respect to the second research objective, two treatment techniques were evaluated in order to suppress the mobilization of elements responsible for the quality deterioration in the recovered ASR drinking water. Each technique approached the problem from a different perspective.

1. Pretreating the source water prior to injection was tested both in the field and with model simulations. Oxygen enrichment of the source water was performed in Herten in order to accelerate the aquifer's leaching from its reactive species. The reactive transport model proved that such approach can actually accelerate pyrite leaching and cause a more extended Fe-hydroxide precipitation, enhancing thus the overall sorption capacity in the aquifer for Fe(II) and partly for Mn(II). Such measure, however, also caused an increased carbonate (Mn-siderite) dissolution, and as a net result, the dissolved Fe(II) and Mn(II) concentrations increased in the aquifer, as observed in Herten and during the column experiments. Pretreating the source water in order to lower its aggressivity towards siderite was modeled using the calibrated reactive transport model of the Herten aquifer. Scenario simulations showed that, if oxygen enrichment is combined with pH-buffering agents (e.g. NaOH), dissolution of Fe(II), Mn(II) and As can be controlled without impeding an accelerated aquifer leaching. This technique was further successfully tested, by scenario simulations, also to other source water types such as desalinated and urban storm water.
2. Aquifer pretreatment was tested next by means of column experiments. In order to neutralize the Mn mobilization which persistently compromised the recovered water quality after having recovered 15% of the injected water, the column sediment was treated with a 0.02M potassium permanganate ($KMnO_4$) solution. The enhanced oxidation reactions with the various reductants in the sediments, causing their partial depletion and an extensive precipitation of Mn-oxides, allowed during the following ASR cycle a recovery efficiency of 110% (net efficiency of 84% with respect to cycle 1) before encountering prohibitive Mn(II) concentrations in the ASR well. While no decrease in pyrite reactivity was observed during 4 cycles of conventional ASR operation, the SO_4 behavior revealed a decrease of 63% in pyrite reactivity after the permanganate treatment. The substantial pyrite "deactivation" was also primarily responsible for the suppressed As mobilization, which initially compromised the recovered water quality after having recovered 75% of the injected water. Arsenic remained well below the drinking water guideline (<10 µg/L) after the permanganate treatment. Despite Mn(II) mobilization during injection still taking place after the treatment, the abundant accumulation of Mn-oxides towards the "ASR well" allowed for an efficient Mn(II) sorption during recovery.

How to improve ASR performance

With respect to the third research objective, ASR performance was tested based on three different source water types, representative of potable ASR applications: pre-treated drinking water, desalinated and urban storm water. The injection of pre-treated drinking water verified the Mn(II) exceedances observed in the Herten aquifer, which derived from the dissolution of Mn-siderite. Inadequate sorption to ferrihydrite because of insufficiently high pH conditions was the main reason for the Mn(II) mobilization. The injection of desalinated water, having an even lower pH as compared to the pre-treated drinking water, caused Fe(II) mobilization even before Mn(II) would exceed the drinking water standard. Injecting urban storm water containing substantial amounts of dissolved organic carbon, lead to a considerable oxygen consumption by the DOC fraction resulting in a less extended precipitation of ferrihydrite. As a consequence, arsenic deriving from the oxidation of pyrite was inadequately sorbed and exceeded the drinking water standard.

Implementing a buffer zone around the ASR well, able to allow for a complete (100%) recovery of the injected water at a specific stage of aquifer development, was finally tested by means of numerical simulations. Independently of the source water used, if recovery is halted and injection restarted as soon as the drinking water standards are exceeded, an effective buffer zone will be gradually formed. The buffer zone build-up was substantially accelerated by enriching the source water with oxygen and NaOH during every cycle until having achieved a 100% efficient buffer zone. From that moment on, the ASR plant will be able to recover 100% efficiently provided that (i) the enrichment continues for a specified number of cycles, and (ii) the cycling scheme of equal amounts of infiltration and recovery can be maintained in practice.

Storage duration was finally evaluated with respect to bubble drift due to the native groundwater flow. Simulating the bubble migration after having created a 100% efficient buffer zone led to exceedances of drinking water standards long before the arrival of the native water. These exceedances were, however, retarded if continuous treatment of the source water took place during the implementation of the buffer zone. On a different note, the abundant resaturation of the permanganate-treated columns with native groundwater, simulating a potential scenario during operational ASR downtime, resulted in substantial reduction of the previously formed Mn-oxides by ferrous iron in the groundwater, releasing higher Mn(II) concentrations. Precipitation of Mn-containing carbonate might occur which can act as an enriched Mn(II) source during potential acid buffering processes, triggered by new ASR cycles when oxic water is injected.

6.2 CONCLUDING RECOMMENDATIONS

Tackling hydrogeochemical issues of ASR application

The following steps are recommended when considering a drinking water ASR application. Once the candidate aquifer and drilling location are found, groundwater and (undisturbed) sediment samples should be obtained at frequent depth intervals during the installation of the ASR well. This way, a good image of the hydrogeochemistry of the candidate aquifer is obtained. At least two fully-recovering (100%) ASR test cycles should then be performed and the recovered water sampled and analyzed at frequent time intervals. Even though one cycle could be enough, performing a second cycle will give additional insight on the natural processes responsible for the removal of various potential pollutants and

therefore for the increase in recovery efficiency with subsequent cycles. The next step is implementing a reactive transport model. The reactive phases and processes to be included should be carefully chosen based on the hydrogeochemical analyses performed. It is up to the modeler to empirically decide which processes should be included in the model and which ones should be treated kinetically. The model should first simulate the two ASR test cycles and should be automatically calibrated based on the water quality recovered from the ASR well. Once the model is calibrated, it is considered capable of predicting the water quality evolution during future ASR cycles. The recovered water quality and, therefore, the evolution of recovery efficiency with respect to threat posing elements during subsequent ASR cycles can be monitored. Depending on the issues to be dealt with, one of the treatment/operational techniques described in this study might be helpful, or even necessary, to render ASR sustainable or to achieve desired goals such as increased recovery efficiency or prolonged storage phase.

Monitoring

It is highly recommended to increase the sampling frequency during the first stages of each ASR phase. This allows fast processes such as cation exchange to be captured in detail and to allow for their accurate numerical simulation. The development of anoxic conditions close to the ASR well during storage is another process, the extent of which can only be assessed by frequent sampling of the ASR well during the initial stage of recovery. Even in field pilots where relatively stable drinking water is injected, a sufficient number of samples is needed to fully characterize input water quality, because small fluctuations may otherwise compromise the extent of the interpreted hydrogeochemical interactions with the aquifer.

Column experiments and pretreatment techniques

Column experiments should be performed as a preliminary step to test the reactivity of the aquifer material, identify the potential mobilization of threat-posing elements and asses how effective the various treatment techniques might be. However, the laboratory assessments performed cannot capture all the complexities of a field ASR application, as described in chapter 5. Treatment techniques should, thus, be tested in a realistic hydraulic situation to verify their positive effects and conclude whether they are applicable from a technical and financial point of view. Promising results were obtained with respect to recovered water quality after pretreating the column sediments with permanganate or the source water with O_2 and NaOH. It is therefore highly recommended to test these techniques in a field pilot.

Scenario modeling

Scenario modeling proved to be a useful tool to visualize and predict the development of the various hydrogeochemical processes of interest in the aquifer, including the evolution of reaction rates, mineral leaching and recovered water quality. It is recommended to take scenario modeling to the next level by implementing 1D ASR reactive transport models in which a number of flow lines in different aquifer layers can be mixed to simulate well mixing. It is finally recommended to upgrade such models by including the behavior of organic micro-pollutants and micro-organisms.

ACKNOWLEDGEMENTS

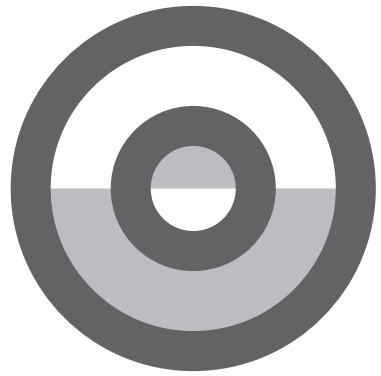

ACKNOWLEDGEMENTS

First and foremost, I would like to express my gratitude to my promotor prof. Pieter Stuyfzand for offering me this challenging opportunity. His support and constant willingness to discuss my issues were remarkable.

To dr. Boris van Breukelen, my co-promotor, I say thank you for the massive support and helping hands at crucial times.

I gratefully acknowledge the creative and immensely helpful presence of dr. Niels Hartog who played a decisive role in my research.

I thank the participants of the research theme ‘‘Underground Water Functions and Well Management’’ (Wetsus cooperation framework) as well as the members of the ‘‘Source Risk Management’’ theme of the joint water sector research program (BTO) for the fruitful discussions and their financial support.

My sincere thanks goes to ir. Jan Willem Kooiman for his excellent team leadership, positivity, and appreciation of my work throughout the entire research period. Thanks to Ir. Jos Boere and the entire Water Systems and Technology Research Group at KWR for being such friendly colleagues. I also owe special thanks to dr. Matthijs Bonte for the pieces of advice at various stages during my research. I heartily thank Sidney Meijering and Harry van Wegen for building the column installation. Many thanks to Koen Zuurbier for the constructive chats and for providing the anoxic core samples for my experiments.

Special thanks to Diego and Kees for being the nicest office mates. Thanks to my friends at KWR (Kerusha, Andrè, Roberto, Sara, Yuki, Helena, Christophe, Ana and Sabrina) and the VU (Stefanie, Heloise, Hylke, Artem and those I can’t recall). Big thanks to Diego, Bea, Manuel, Jeremy, Reinert, Thijs, Andres, Ine, Nikos, Panos and Harry.

My sincere thanks and appreciation go to my parents Anna and Takis for their love, support, patience and cooperation. And finally, to my beautiful Maria, thanks for everything <4

REFERENCES

REFERENCES

Appelo, C. A. J. (1994). “Cation and proton exchange, pH variations, and carbonate reactions in a freshening aquifer.” Water Resources Research 30(10): 2793-2805.

Appelo, C. A. J., Drijver, B., Hekkenberg, R. and de Jonge, M. (1999). “Modeling In Situ Iron Removal from Ground Water.” Ground Water 37(6): 811-817.

Appelo, C. A. J. and Postma, D. (2005). Geochemistry, groundwater and pollution, 2nd edn. Leiden, The Netherlands, AA Balkema.

Appelo, C. A. J., Van Der Weiden, M. J. J., Tournassat, C. and Charlet, L. (2002). “Surface Complexation of Ferrous Iron and Carbonate on Ferrihydrite and the Mobilization of Arsenic.” Environmental Science & Technology 36(14): 3096-3103.

Appelo, C. A. J., Verweij, E. and Schäfer, H. (1998). “A hydrogeochemical transport model for an oxidation experiment with pyrite/calcite/exchangers/organic matter containing sand.” Applied Geochemistry 13(2): 257-268.

Appelo, C. A. J. and Vet, W. W. J. M. (2003). Modeling in situ iron removal from groundwater with trace elements such as As. Arsenic in Ground Water. A. Welch and K. Stollenwerk, Springer US: 381-401.

Arthur, J. D., Dabous, A. A. and Fischler, C. (2007). Aquifer storage and recovery in Florida: geochemical assessment of potential storage zones. ISMAR 6, Phoenix, Arizona, Acacia Publishing Incorporated.

Barry, K., Dillon, P. J. and Pavelic, P. (2007). Mixing and clogging constraints on domestic-scale ASR at Kingswood, South Australia. ISMAR 6, Phoenix, Arizona, Acacia Publishing Incorporated.

Braester, C. and Martinell, R. (1988). “The Vyredox and Nitredox methods of in situ treatment of groundwater.” Water Science and Technology 20(3): 149-163.

Brown, C. J. and Misut, P. E. (2010). “Aquifer geochemistry at potential aquifer storage and recovery sites in coastal plain aquifers in the New York city area, USA.” Applied Geochemistry 25(9): 1431-1452.

Buamah, R. (2009). Adsorptive Removal of Manganese, Arsenic and Iron from Groundwater. Leiden, The Netherlands, CRC Press/Balkema.

Buamah, R., Petrusevski, B., de Ridder, D., van de Wetering, T. S. C. M. and Schippers, J. C. (2009). “Manganese removal in groundwater treatment: practice, problems and probable solutions.” Journal of Water Science and Technology 9(1): 89-98.

Buamah, R., Petrusevski, B. and Schippers, J. (2008). “Adsorptive removal of manganese(II) from the aqueous phase using iron oxide coated sand.” J Water SRT -- AQUA 57(1): 1-11.

Buijs, E. A. and Van der Grift, B. (2001). Underground reactivity during Aquifer Storage Recovery (ASR) in Limburg. Utrecht, TNO.

Cavé, L., Hartog, N., Al, T., Parker, B., Mayer, K. U. and Cogswell, S. (2007). “Electrical Monitoring of In Situ Chemical Oxidation by Permanganate.” Ground Water Monitoring & Remediation 27(2): 77-84.

Cremer, N., Obermann, P., Wisotzky, F., Schulz, H. and Hadeler, A. (2003). Mobilization of nickel, cobalt and arsenic in a multi-aquifer formation of the Lower Rhine valley: identification and modeling of the processes controlling metal mobility. Geochemical processes in soil and groundwater: measurement, modelling, upscaling. GeoProc2002 conference, Bremen, Germany, 4-7 March 2002., Wiley-VCH Verlag GmbH.

Dai, Z. and Samper, J. (2004). “Inverse problem of multicomponent reactive chemical transport in porous media: Formulation and applications.” Water Resour. Res. 40(7): W07407.

Davies, S. H. R. and Morgan, J. J. (1989). “Manganese(II) oxidation kinetics on metal oxide surfaces.” Journal of Colloid and Interface Science 129(1): 63-77.

Davison, W. and Seed, G. (1983). “The kinetics of the oxidation of ferrous iron in synthetic and natural waters.” Geochimica et Cosmochimica Acta 47(1): 67-79.

Dellwig, O., Watermann, F., Brumsack, H. J., Gerdes, G. and Krumbein, W. E. (2001). “Sulphur and iron geochemistry of Holocene coastal peats (NW Germany): a tool for palaeoenvironmental reconstruction.” Palaeogeography, Palaeoclimatology, Palaeoecology 167(3–4): 359-379.

Descourvieres, C., Prommer, H., Oldham, C., Greskowiak, J. and Hartog, N. (2010). “Kinetic reaction modeling framework for identifying and quantifying reductant reactivity in heterogeneous aquifer sediments.” Environ Sci Technol 44(17): 6698-6705.

Diem, D. and Stumm, W. (1984). “Is dissolved Mn(II) being oxidized by O2 in absence of Mn-bacteria or surface catalysts?” Geochimica et Cosmochimica Acta 48(7): 1571-1573.

Dillon, P. and Barry, K. (2005). Domestic Scale Rainwater ASR Demonstration Project. Project Status Report July 2003 – June 2005, CSIRO Land and Water.

Doherty, J. (2005). PEST: Software for Model-Independent Parameter Estimation (User Manual). Australia.

Dzombak, D. A. and Morel, F. M. M. (1990). Surface Complexation Modeling - Hydrous Ferric Oxide. New York, Wiley.

ENTRIX (2009). Technical memorandum: city of DeLand airport ASR program, mini-scale pilot test of deoxygenation using sulfides, St. Johns river water management district.

Evangelou, V. P. (1995). Pyrite Oxidation and Its Control, CRC Press.

Gao, X., Wang, Y., Hu, Q. and Su, C. (2011). “Effects of anion competitive adsorption on arsenic enrichment in groundwater.” Journal of Environmental Science and Health, Part A 46(5): 471-479.

Gaus, I., Shand, P., Gale, I. N., Williams, A. T. and Eastwood, J. C. (2002). “Geochemical modelling of fluoride concentration changes during Aquifer Storage and Recovery (ASR) in the Chalk aquifer in Wessex, England.” Quarterly Journal of Engineering Geology and Hydrogeology 35(2): 203-208.

Gerges, N. Z., Howles, S. R. and Dennis, K. J. (1998). ASR, Hydraulic and salinity response in unconfined / confined aquifers. 3rd International Symposium on Artificial Recharge of Groundwater, Balkema: 269-274.

Goldhaber, M. B. (1983). “Experimental study of metastable sulfur oxyanion formation during pyrite oxidation at pH 6-9 and 30°C.” American Journal of Science 283: 193-217.

Greskowiak, J., Prommer, H., Vanderzalm, J., Pavelic, P. and Dillon, P. (2005). “Modeling of carbon cycling and biogeochemical changes during injection and recovery of reclaimed water at Bolivar, South Australia.” Water Resour. Res. 41(10): W10418.

Griffioen, J., Klein, J. and van Gaans, P. F. M. (2012). “Reaction capacity characterization of shallow sedimentary deposits in geologically different regions of the Netherlands.” Journal of Contaminant Hydrology 127(1–4): 30-46.

Hartog, N., Griffioen, J. and Van der Weijden, C. H. (2002). “Distribution and Reactivity of O_2-Reducing Components in Sediments from a Layered Aquifer.” Environmental Science & Technology 36(11): 2338-2344.

Herczeg, A. L., Rattray, K. J., Dillon, P. J., Pavelic, P. and Barry, K. E. (2004). “Geochemical Processes During Five Years of Aquifer Storage Recovery.” Ground Water 42(3): 438-445.

Herrmann, R. (2005). ASR well field optimization in unconfined aquifers in the Middle East. ISMAR 5, Berlin, Germany, United Nations Educational, Scientific and Cultural Organization.

Huisman, D. J. (1998). Geochemical characterization of subsurface sediments in the Netherlands. PhD thesis. Wageningen University.

Huisman, D. J. and Kiden, P. (1997). “A geochemical record of Late Cenozoic sedimentation history in the southern Netherlands.” Geologie en Mijnbouw 76(4): 277-291.

Ibison, M. A., Sanders, F. A., Glanzman, R. K. and Dronfield, D. G. (1995). Manganese in recovered water from an ASR well. Second International Symposium on Artificial Recharge of Ground Water, Florida, American Society of Civil Engineers.

Izbicki, J. A., Petersen, C. E., Glotzbach, K. J., Metzger, L. F., Christensen, A. H., Smith, G. A., O’Leary, D., Fram, M. S., Joseph, T. and Shannon, H. (2010). “Aquifer Storage Recovery (ASR) of chlorinated municipal drinking water in a confined aquifer.” Applied Geochemistry 25(8): 1133-1152.

Johnson, D. B. and Hallberg, K. B. (2005). “Acid mine drainage remediation options: a review.” Science of The Total Environment 338(1–2): 3-14.

Jones, G. W. and Pichler, T. (2007). “Relationship between pyrite stability and arsenic mobility during aquifer storage and recovery in southwest central Florida.” Environmental Science & Technology 41: 723-730.

Karlsen, R., Smits, F., Stuyfzand, P., Olsthoorn, T. and Van Breukelen, B. (2012). “A post audit and inverse modeling in reactive transport: 50years of artificial recharge in the Amsterdam Water Supply Dunes.” Journal of Hydrology 454: 7-25.

Kohn, S. (2009). City of Bradenton Potable Water ASR Degas Pretreatment Pilot Study. ASR 9, Orlando FL.

Lord III, C. J. (1982). “A Selective and Precise Method for Pyrite Determination in Sedimentary Materials: RESEARCH-METHOD PAPER.” Journal of Sedimentary Research 52(2).

Lucas, M., McGill, K. and Glanzman, D. (1994). Controlling iron concentrations in the recovered water from aquifer storage and recovery (ASR) wells. 2nd International Symposium on Artificial Recharge of groundwater, American Society of Civil Engineers.

Mahmoodlu, M. G., Hassanizadeh, S. M. and Hartog, N. (2013). “Evaluation of the kinetic oxidation of aqueous volatile organic compounds by permanganate.” Science of The Total Environment(0).

Maliva, R. G. and Missimer, T. M. (2010). Aquifer storage and recovery and managed aquifer recharge using wells: planning, hydrogeology, design and operation., Schlumberger.

Maliva, R. G., Missimer, T. M. and Guo, W. (2007). Aquifer storage and recovery of reclaimed water in Florida: hydrogeological issues. ISMAR 6, Phoenix, Arizona, Acacia Publishing Incorporated.

McKibben, M. A. and Barnes, H. L. (1986). “Oxidation of pyrite in low temperature acidic solutions: rate laws and surface textures.” Geochimica et Cosmochimica Acta 50: 1509-1520.

Mettler, S. (2002). In situ removal of iron from ground water: Fe (II) oxygenation, and precipitation products in a calcareous aquifer. Swiss Federal Institute of Technology. Zurich. Doctor of Natural Sciences.

Mirecki, J. E. (2004). Water quality changes during cycle testing at aquifer storage recovery (ASR) systems of South Florida. ERDC Techn. Report US Army Engineer Research and Development Center. Vicksburg, MS: 39.

Mukhopadhyay, A., Al-Awadi, E., AlSenafy, M. N. and Smith, P. C. (1998). “Laboratory investigations of compatibility of the Dammam Formation Aquifer with desalinated freshwater at a pilot recharge site in Kuwait.” Journal of Arid Environments 40(1): 27-42.

Nicholson, R. V., Gillham, R. W. and Reardon, E. J. (1990). “Pyrite oxidation in carbonate buffered solution. 2. Rate control by oxide coatings.” Geochimica et Cosmochimica Acta 54: 395-402.

Overacre, R., Clinton, T., Pyne, D., Snyder, S. and Dillon, P. J. (2006). Reclaimed water aquifer storage and recovery: Potential changes in water quality. WEFTEC. Dallas, Water Environment Foundation: 1339-1360.

Page, D., Dillon, P., Toze, S., Bixio, D., Genthe, B., Jiménez Cisneros, B. E. and Wintgens, T. (2010). “Valuing the subsurface pathogen treatment barrier in water recycling via aquifers for drinking supplies.” Water Research 44(6): 1841-1852.

Parkhurst, D. L. and Appelo, C. (2013). “Description of input and examples for PHREEQC version 3 A computer program for speciation, batch-reaction, one-dimensional transport, and inverse geochemical calculations.” US Geological Survey Techniques and Methods, Book 6, Modeling Techniques.

Parkhurst, D. L. and Appelo, C. A. J. (1999). User’s guide to PHREEQC (version 2) - A computer program for speciation, batch-reaction, one dimensional transport, and inverse geochemical calculations. Water-Resources Investigations Report 99-4259. Denver, Colorado.

Parkhurst, D. L., Plummer, L. N. and Thorstenson, D. C. (1982). “Balance- A Computer Program for Calculating Mass Transfer for Geochemical Reactions in Ground Water.”

Pavelic, P., Nicholson, B. C., Dillon, P. J. and Barry, K. E. (2005). “Fate of disinfection by-products in groundwater during aquifer storage and recovery with reclaimed water.” Journal of Contaminant Hydrology 77(1–2): 119-141.

Pearce, M. S. and Waldron, M. (2010). ASR using sodium bisulfide for deoxygenation to prevent arsenic mobilization. AGWT-AIPG joint conference, Orlando FL.

Petkewich, M. D., Parkhurst, D. L., Conlon, K. J., Campbell, B. G. and Mirecki, J. E. (2004). Hydrologic and geochemical evaluation of aquifer storage recovery in the Santee Limestone/Black Mingo aquifer, Charleston, South Carolina, 1998–2002: U.S. Geological Survey Scientific Investigations Report 2004–5046.

Plummer, L. N., Prestemon, E. C. and Parkhurst, D. L. (1991). An interactive code (NETPATH) for modeling net geochemical reactions along a flow path, Department of the Interior, US Geological Survey.

Plummer, L. N., Wigley, T. M. L. and Parkhurst, D. L. (1978). “The kinetics of calcite dissolution in CO 2 -water systems at 5 degrees to 60 degrees C and 0.0 to 1.0 atm CO 2.” American Journal of Science 278(2): 179-216.

Postma, D. and Appelo, C. A. J. (2000). “Reduction of Mn-oxides by ferrous iron in a flow system: column experiment and reactive transport modeling.” Geochimica et Cosmochimica Acta 64(7): 1237-1247.

Price, R. E. and Pichler, T. (2006). “Abundance and mineralogical association of arsenic in the suwannee limestone (Florida) : Implications for arsenic release during water-rock interaction.” Chemical Geology 228: 44-56.

Prommer, H. and Stuyfzand, P. J. (2005). “Identification of Temperature-Dependent Water Quality Changes during a Deep Well Injection Experiment in a Pyritic Aquifer.” Environmental Science & Technology 39: 2200-2209.

Pyne, R. D. G. (2003). Water quality in aquifer storage recovery (ASR) wells. American Water Works Association Annual Meeting. Orlando.

Pyne, R. D. G. (2005). Aquifer Storage Recovery: A Guide to Groundwater Recharge through Wells. Second Edition. Gainesville, Florida, USA, ASR Systems LLC.

Pyne, R. D. G., Glanzman, R. K. and Odom, E. (2013). Aquifer Conditioning to Minimize Iron and Manganese In Recovered Water from ASR Projects ISMAR8, Beijing.

Pyne, R. D. G., McNeal, M. B. and Horvath, L. E. (2004). Analysis of Arsenic Occurrence and Attenuation in Thirteen Operational ASR Wellfields in the Floridan and Hawthorn Aquifers. Technical Memorandum prepared for Florida Department of Environmental Protection.

Rashid, N. and Almulla, A. (2005). Aquifer Storage Recovery (ASR): An economic analysis to support use as a strategic managerial tool to balance a city’s desalinated water production and demand. ISMAR 5, Berlin, Germany, United Nations Educational, Scientific and Cultural Organization.

Rott, U. and Friedle, M. (1985). “Physical, chemical and biological aspects of the removal of iron and manganese underground.” Water Supply 3(2): 143-150.

Saaltink, M. W., Ayora, C., Stuyfzand, P. J. and Timmer, H. (2003). “Analysis of a deep well recharge experiment by calibrating a reactive transport model with field data.” Journal of Contaminant Hydrology 65(1-2): 1-18.

Savage, K. S., Tingle, T. N., O’Day, P. A., Waychunas, G. A. and Bird, D. K. (2000). “Arsenic speciation in pyrite and secondary weathering phases, Mother Lode gold district, Tuolumne County, California.” Applied Geochemistry 15(8): 1219-1244.

Schäfer, W. (2001). “Predicting natural attenuation of xylene in groundwater using a numerical model.” Journal of Contaminant Hydrology 52(1–4): 57-83.

Scot, T. M. (2005). Precipitation and Dissolution of Iron and Manganese Oxides. Environmental Catalysis, CRC Press: 61-82.

Singer, P. C. and Stumm, W. (1970). “Acidic Mine Drainage: The Rate-Determining Step.” Science 167(3921): 1121-1123.

Stumm, W. and Lee, G. F. (1961). “Oxygenation of Ferrous Iron.” Industrial & Engineering Chemistry 53(2): 143-146.

Stumm, W. and Morgan, J. J. (1996). Aquatic Chemistry, chemical equilibria and rates in natural waters. Third edition. New York, Wiley.

Stuyfzand, P. J. (1998a). Quality changes upon injection into anoxic aquifers in the Netherlands: Evaluation of 11 experiments. Artificial Recharge of Groundwater. J. H. e. a. Peters. Rotterdam, Balkema: 283-291.

Stuyfzand, P. J. (1998b). Simple models for reactive transport of pollutants and main constituents during artificial recharge and bank filtration. Artificial recharge of groundwater, Proc. 3rd Intern. Symp. on Artificial Recharge, Amsterdam, the Netherlands, Balkema.

Stuyfzand, P. J. (2001). Pyrite oxidation and side-reactions upon deep well injection. WRI-10, Proc. 10th Internat. Symp. on Water Rock Interaction, Vol. 2, Villasimius, Italy.

Stuyfzand, P. J. (2010). Hydrogeochemical processes during river bank filtration and artificial recharge of polluted surface waters: zonation, identification and quantification. Riverbank Filtration for Water Security in Desert Countries, Shamrukh, Mohamed.

Stuyfzand, P. J., Arens, S. M., Oost, A. P. and Baggelaar, P. K. (2012). Geochemische effecten van zandsuppleties in Nederland (in Dutch). The Hague, The Netherlands, Bosschap.

Stuyfzand, P. J., Bunnik, J., Medema, A. J., Vogelaar, A. J., Wakker, J. C. and Verheijden, S. M. L. (2005a). Water quality changes, clogging and pathogen transport during deep well injection in the South-East Netherlands (DIZON). Water quality improvements during aquifer storage and recovery, Vol.2 Compilation of information from ten sites - AWWA report. P. J. Dillon and S. Toze: 77-103.

Stuyfzand, P. J. and Pyne, R. D. G. (2010). Arsenic behavior in SW Florida ASR systems and its expert modeling. ISMAR 7, Abu Dhabi.

Stuyfzand, P. J., Vogelaar, A. J. and Wakker, J. C. (2002). Hydrogeochemistry of prolonged deep well injection and subsequent aquifer storage in pyritiferous sands; DIZON pilot, Netherlands. 4th International Symposium on Artificial Recharge of Groundwater. P. J. Dillon, Balkema: 107-110.

Stuyfzand, P. J., Wakker, J. C. and Putters, B. (2005b). Water quality changes during Aquifer Storage and Recovery (ASR): results from pilot Herten (Netherlands), and their implications for modeling. ISMAR 5, Berlin, Germany, United Nations Educational, Scientific and Cultural Organization.

Swedlund, P. J. and Webster, J. G. (1999). “Adsorption and polymerisation of silicic acid on ferrihydrite, and its effect on arsenic adsorption.” Water Research 33(16): 3413-3422.

US-EPA (2009). Secondary drinking water regulations: guidance for nuisance chemicals. Washington, GPO.

Van Beek, C. G. E. M. (1983). In situ iron removal: An evaluation of investigations. Nieuwegein, The Netherlands, KIWA.

Van Breukelen, B. M., Griffioen, J., Röling, W. F. M. and van Verseveld, H. W. (2004). “Reactive transport modelling of biogeochemical processes and carbon isotope geochemistry inside a landfill leachate plume.” Journal of Contaminant Hydrology 70(3-4): 249-269.

Van Cappellen, P. and Gaillard, J.-F. (1996). “Biogeochemical dynamics in aquatic sediments.” Reviews in Mineralogy and Geochemistry 34(1): 335-376.

Van Halem, D. (2011). Subsurface iron and arsenic removal for drinking water treatment in Bangladesh. Delft, The Netherlands, Water Management Academic Press.

Vanderzalm, J. L., Dillon, P. J. and Le Gal La Salle, C. (2007). Arsenic mobility under variable redox conditions induced during ASR. ISMAR 6, Phoenix, Arizona, Acacia Publishing Incorporated.

Vanderzalm, J. L., Le Gal La Salle, C. and Dillon, P. J. (2006). “Fate of organic matter during aquifer storage and recovery (ASR) of reclaimed water in a carbonate aquifer.” Applied Geochemistry 21(7): 1204-1215.

Vanderzalm, J. L., Le Gal La Salle, C., L., H. J. and Dillon, P. J. (2002). Water quality changes during aquifer storage and recovery at Bolivar, South Australia. Management of Aquifer Recharge for Sustainability. P. J. Dillon, A. A. Balkema: 83-88.

Vanderzalm, J. L., Page, D. W., Barry, K. E. and Dillon, P. J. (2010). “A comparison of the geochemical response to different managed aquifer recharge operations for injection of urban stormwater in a carbonate aquifer.” Applied Geochemistry 25(9): 1350-1360.

Wallis, I., Prommer, H., Pichler, T., Post, V., B. Norton, S., Annable, M. D. and Simmons, C. T. (2011). “Process-Based Reactive Transport Model To Quantify Arsenic Mobility during Aquifer Storage and Recovery of Potable Water.” Environmental Science & Technology 45(16): 6924-6931.

Williamson, M. A. and Rimstidt, J. D. (1994). “The kinetics and electrochemical rate-determining step of aqueous pyrite oxidation.” Geochimica et Cosmochimica Acta 58(24): 5443-5454.

Zhang, Y.-C., Slomp, C. P., Broers, H. P., Passier, H. F. and Cappellen, P. V. (2009). “Denitrification coupled to pyrite oxidation and changes in groundwater quality in a shallow sandy aquifer.” Geochimica et Cosmochimica Acta 73(22): 6716-6726.

Zuurbier, K. G., Zaadnoordijk, W. J. and Stuyfzand, P. J. (2014). “How multiple partially penetrating wells improve the freshwater recovery of coastal ASR systems: a field and modeling study.” Journal of Hydrology.

BIOGRAPHY

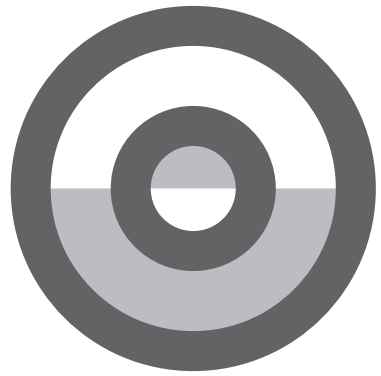

BIOGRAPHY

Andreas Antoniou, after completing his secondary education in 2001, proceeded to pursue a BSc in Earth Sciences at the Aristotle University of Thessaloniki, Greece. After graduating (2005) he moved to Savona (Italy) to work as an intern for a civil engineering firm dealing with flood risk zone mapping and river basin development. In 2006 he moved to Amsterdam to follow a 2-year master program in Hydrology at the Vrije University. For his MSc thesis he investigated the tidal effects on the freshwater lens at Majuro atoll (Republic of Marshall Islands) and quantified the freshwater supply available for distribution. In 2009 he started his PhD research at KWR Watercycle Research Institute under the guidance of prof. Pieter Stuyfzand (VU, KWR) and asst. prof. Boris van Breukelen (VU).